THE INTEGRATION OF GALLIUM-BASED LIQUID METAL ENERGY CIRCUITS INTO ADDITIVELY MANUFACTURED SHAPE MEMORY ALLOY ACTUATORS FOR INCREASED ACTUATION FREQUENCIES

A Thesis

by

JACOB LEE MINGEAR

Submitted to the Office of Graduate and Professional Studies of
Texas A&M University
in partial fulfillment of the requirements for the degree of

MASTER OF SCIENCE

Chair of Committee,	Darren Hartl
Committee Members,	Jim Boyd
	Ibrahim Karaman
Head of Department,	Rodney Bowersox

December 2018

Major Subject: Aerospace Engineering

ABSTRACT

Large monolithic shape memory alloy (SMA) actuators are currently limited to applications with low cyclic actuation frequency due to their high thermal masses coupled with low heat transfer rates. Liquid gallium-indium eutectic is a room-temperature liquid metal that can be used as a multifunctional heat transfer fluid. Integrated into an additively manufactured NiTi SMA actuator, liquid metal can cool an actuator via forced fluid convection through interior channels and then use those same channels to inductively heat the SMA, if electrically isolated and configured into induction-favorable geometries. Computational models suggest that such actuators can demonstrate an increased actuation frequency of 400%, compared to traditional cycling of large SMAs.

In this work, a cantilever SMA beam actuator is additively manufactured with an embedded planar induction geometry for a latterly applied liquid metal channel. This actuator is deformed, actuated, and found to have an increased cooling rate of 40% compared to free convection. A variety of topics related to the integration of liquid metal and SMAs are also investigated including: the surface roughness of additively manufactured internal structures and its mitigation via electropolishing techniques, liquid metal-induced corrosion, and polymer coatings for electrical isolation of the liquid metal adhered to a high-temperature, highly strained SMA. It is also concluded that lower laser energy density during additive manufacturing leads to reduced surface roughness, liquid metal does not induce corrosion on NiTi alloys until temperatures between 400°C and 600°C, and Xylan® acts as a sufficient coating for the electrical insulation of SMAs.

DEDICATION

To my mother Jill Mingear, my father Darren Mingear, my brother Samuel Mingear, my grandmothers Anna Mingear and Kate Schwartz, and my grandfathers Jack Mingear and Jerry Schwartz.

ACKNOWLEDGMENTS

I would like to first thank my parents for their obvious love and support in addition to giving me the confidence that I can do whatever I set my mind to. They supported and instilled a strong scientific foundation since childhood starting from physics museums to watching TV science shows to helping me with my many science fair projects. This prepared me for college-level research I started as a freshman and eventually led to the research I do today.

I would to thank Dr. Hartl for providing me countless opportunities to learn more and be truly curious about my research, as evidenced by the 'rabbit holes' I seemingly go down. Further, I would like to thank him for his critical guidance and research philosophy, in which I hope to effectively demonstrate.

I would like to thank Jessica Zamarripa for her hard work and many late nights in the lab preparing the liquid metal SMA beam and learning various metrologies.

I would like to thank Brent Bielefeldt for his dedication towards the great computational modeling work motivating this study.

I would like to thank the many undergraduates and graduate students of the Maestro Lab for their friendship, enthusiasm, and camaraderie.

I would like to thank Zahir Udovicic from the Aerospace Engineering machine shop at the Low Speed Wind Tunnel for producing parts promptly, enabling many of the described experiments without weariness.

I would like to acknowledge both James Jim Mabe and Frederick Tad Calkins of The Boeing Company for their support and guidance regarding SMA testing hardware.

I would like to thank the Bing Zhang and Alaa Elwany (Department of Industrial and Systems Engineering, Texas A&M University) for their collaboration of laser powder-bed fusion additive manufacturing of the various NiTi parts and test pieces found in several experiments in this work.

I would like to acknowledge Mohammad Naraghi (Department of Aerospace Engineering, Texas A&M University) for providing ovens for the liquid metal-induced corrosion experiments.

CONTRIBUTORS AND FUNDING SOURCES

Contributors

This work was supported by a thesis committee consisting of Professor Darren Hartl and James Boyd of the Department of Aerospace Engineering and Professor Ibrahim Karaman of the Department of Materials Science and Engineering.

Brent Bielefeldt produced the computational work, found in Section 1.2, which helped motivate this work.

Experimentally testing the liquid metal integrated shape memory alloy actuator in Sections 2.1 and 3.1 was assisted by Jessica Zamarripa, Emery Sheahan, Marcela Cabral Seanez, and John Rohmer.

The additively manufactured NiTi parts for the studies regarding the liquid metal SMA actuator and the surface roughness of interior channels were produced by Bing Zhang and Professor Alaa Elwany of the Department of Industrial and Systems Engineering. Further, Bing Zhang performed the ANOVA analysis found in Section 3.2.

All other work conducted for the thesis was completed by the student independently.

Funding Sources

This work and graduate study was supported in part by the US Air Force Office of Scientific Research under a grant number FA9550-16-1-0087, titled Avian-Inspired Multifunctional Morphing Vehicles monitored by Dr. B. L. Lee.

NOMENCLATURE

SMA	Shape Memory Alloy
SME	Shape Memory Effect
NiTi	Nickel-Titanium
A_s	Austinite Start
A_f	Austinite Finish
M_a	Martensite Start
M_f	Martensite Finish
UCT	Upper Cycle Temperature (of an SMA thermal cycle)
LCT	Lower Cycle Temperature (of an SMA thermal cycle)
AM	Additive Manufacturing
L-PBF	Laser Powder-Bed Fusion
E-GaIn	Eutectic Gallium-Indium Alloy
E-GaInSn	Eutectic Gallium-Indium-Tin Alloy
JH	Joule Heating
RF	Radio-Frequency (3 kHz - 300 GHz)
AC	Alternating Current
SEM	Scanning Electron Microscopy
EDS	Energy Dispersive X-Ray Spectroscopy
BSE	Back-Scatter Electrons
SE	Secondary Electrons
DOE	Design of Experiments
ANOVA	Analysis of Variance
S_a	Arithmetic Mean Areal Surface Roughness
S_q	Root-Mean-Square Areal Surface Roughness
S_{sk}	Areal Skewness
S_{ku}	Areal Kurtosis

TABLE OF CONTENTS

Page

LIST OF FIGURES

FIGURE Page

LIST OF TABLES

TABLE Page

1. INTRODUCTION

1.1 Motivation

Over the past decades, shape memory alloys (SMAs) have gained the attention of engineers for use as actuators by virtue of their high actuation energy density and have been implemented in a variety of fields including aerospace, marine, biomedical, and even consumer products. [1, 2, 3] Nickel-titanium and its related alloys dominate the SMA community as they can recover their original shapes after seemingly permanent deformations (e.g., bending, twisting, or axial deformations) provided sufficient applied thermal stimulus (i.e., heating). Equiatomic nickel-titanium, referred to as $Ni_{50}Ti_{50}$, exhibits fully recoverable strains of up to 7% [2]. Increasing the nickel content from 50 to 55 at.% Ni lowers the strain recovery capability to 3% but drastically increases the thermally induced fatigue resistance and thus has received special attention in aerospace [4, 5]. Further, additions of Hf, in replacement of Ti, increases the transformation temperature (e.g., 190°C in $Ni_{49}Ti_{36}Hf_{15}$) enabling shape recovery in higher temperature environments [6], greatly expanding their engineering capability.

Despite the actuation energy density of SMA materials poised as one of the highest of any active material, such actuators are limited to low cyclic actuation frequencies. SMA materials typically have limited heat transfer rates, which prevents a given actuator from performing repetitive and rapid actuation cycles. An increase in actuation frequency can be accomplished by increasing the heating and/or cooling rates of SMA actuators. Futher, this low cyclic actuation frequency leads to an overall low actuator power density (energy density per time), which is a common metric used to benchmark them against other types of actuators (e.g., hydraulic systems and electric motors). An increase in cyclic actuation frequency could position SMA actuators as the highest power density option among all actuators, as they are currently outperformed by multicomponent hydraulic systems [7].

A new option for increasing the cyclic frequency of SMA actuators involves the use structurally

embedded room-temperature liquid metal cooling circuits with geometric configurations designed for induction heating capabilities. In the past, high-temperature liquid metals such as lithium or sodium were considered as cooling fluids for nuclear reactors due to their high thermal stability and thermal conductivity [8, 9]. Eutectic gallium-indium (E-GaIn) is a non-toxic, room-temperature liquid metal alloy that melts at 15.3°C [10] and has been geometrically configured liquid metal circuits have been introduced into bulk materials ranging from soft elastomers to fiber reinforced composites to create flexible induction coil heaters [11] and tunable RF devices [12]. Embedded E-GaIn channels in a monolithic SMA actuator can increase cooling rates due to its high thermal conductivity, and if configured into helical coils and properly supplied electrical power, they can enable rapid and distributed induction heating for large SMA structures.

This thesis represents the efforts to demonstrate the production, experimental characterization of such an SMA-liquid metal composite actuator undergoing full cyclic operation. Specifically, a bending beam actuator with a planar spiral channel near the cantilevered end of the beam is considered, where the design of this channel is driven primarily by its performance as an inductive coil. The planar spiral channel has an open cross-section for ease of access, specifically enabling the application of the chosen electrically insulating coating to isolate the liquid metal from the SMA itself. Further, this thesis investigates two topics which allow for further modifications to the liquid metal integration of SMAs being: the surface roughness of interior channels from laser powder-bed fusion additive manufacturing and the liquid metal-induced corrosion of SMAs. Understanding the surface roughness of interior channels in additively manufactured sturctures enables liquid metal channels to be fully embedded into the SMA actuator enabling faster and more efficient heat transfer. Understanding liquid metal-induced corrosion allows the ability to access the durability of such a device, where a small crack in coating electrically isolating the liquid metal will not result in catastrophic corrosion; further this understand can enable different ways of liquid metal metal integration such as liquid metal flowing and in direct contact with hollow SMA wires. Fig. 1.1 relates the various multi-physical technical fields that enable such a liquid metal SMA actuator.

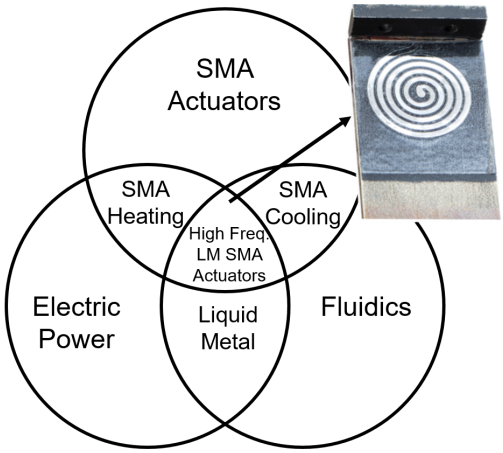

Figure 1.1: Diagram of the overlapping research fields that enable high-frequency liquid metal SMA actuators.

1.2 Literature Review

1.2.1 Review of Increased Actuation Frequency of SMA Actuators

SMA actuators are typically heated to the actuation temperature threshold via direct Joule heating in the case of wire-form SMAs, or via patch heaters and coil induction for bulk form SMAa [13, 14]. Cooling is usually achieved by free convection in air or forced fluid convection. Increasing the heat transfer rates of SMA components has been addressed in previous research efforts via increased heating and cooling rates [14, 15, 16, 17]. Methods outlined by Saunders et al. tabulated various additional ways to heat and cool SMA actuators in Table 1.1, adapted from [13].

Table 1.1: Methods for heating and cooling of shape memory alloys, adapted from [13]

Heating	Cooling
Direct resistive	Free convection (air)
Capacitance-assisted resistive	Liquid immersion
Conductive	Heat sinking
Convective	Peltier effect
Radiative (laser)	Forced fluid convection
Inductive	*Cool Chips* technology

Some highlighted methods include attaching Peltier coolers to an SMA component [15], immersing SMAs in a fluid bath after actuation, using exterior induction coils and forced air convection in torque tubes [18], and incorporating microvascular cooling channels for forced fluid convection [17, 19, 20]. Such methods are strongly application-specific; for example, an SMA device would be impractical to immerse into a heavy liquid reservoir in an application where low weight is required. Further, the use of a heavy cooling system would decrease the overall SMA actuator power density. Localized forced fluid convection remains the more viable option for lightweight applications; one version has been demonstrated with torque tube SMA actuators, where forced air flow through the hollow center was employed to rapidly cool the device [19]. Tubular geometry, in particular, facilitates straight-forward fabrication and interfacing with pressurized fluid systems. Forced fluid convection has also been implemented in non-tubular microchannel-based designs fabricated using sacrificial material vaporization from Coppola et al. [17]. Oil and water were flowed through microvascular channels in an SMA-polymer matrix composite and successfully removed heat from the SMA component; however, production of the device required multiple manufacturing steps including manual placement of Mg wires at desired channel locations, hot compaction spark plasma sintering, Mg vaporization, and electric discharge machining, while channel topologies were only limited to near-planar configurations.

Liquid metal, such as E-GaIn, can act as an effective heat transfer fluid [21] especially in applications of channel-based forced fluid convection. Further these channels could be multifunctional; the high electrical conductivity of E-GaIn could provide induction heating to the SMA if applied the appropriate RF current. Thus, channel-based designs have flowed liquid E-GaIn through embedded exterior channels in an L-PBF-fabricated NiTi SMA actuator [22, 23] which showed an increase in cyclic actuation frequency from both higher heating and cooling rates.

1.2.2 Review of the Laser Powder-Bed Fusion Additive Manufacturing of SMA Actuators with Internal Channel Considerations

The fabrication of NiTi shape memory alloy actuators with complex structures, such as channels, is challenging using traditional manufacturing technologies due to NiTi's difficulty to ma-

chining and sensitivity to temperature history and composition. Additive manufacturing (AM) is a set of emerging manufacturing technologies known for its ability to create objects with high degrees of geometric freedom, primarily due to its layer-by-layer fabrication based on digital 3D models. Laser powder-bed fusion (L-PBF) AM, commercially known as selective laser melting (SLM), is a method that uses a high-energy laser beam to selectively fuse metallic powder in a powder-bed and can process metallic powders including stainless steels, titanium alloys, nickel-based superalloys, and NiTi SMAs [24, 25, 26, 27, 28, 29]. Complex geometries with optimized topologies, such as internal microvascular channels, can thus be readily produced and are especially useful in the fabrication of complex NiTi parts; limitations in conventional manufacturing methods previously resulted in most SMA structures being limited to simple geometries such as wires, sheets, and tubes [30, 31, 32]. Furthermore, it has recently been shown that the functional properties of SLM-fabricated NiTi actuators can be tailored through local control of the thermal histories during fabrication via controlling SLM process parameters, without the need for training or post-fabrication heat treatments [33, 34]. L-PBF can thus enable the development of SMA actuators with complex geometric features such as producing hollow channels for liquid metal energy circuits to substantially improve SMA cyclic actuation frequency.

The surface integrity of interior channels in SMA actuators is critical to enable increased performance in actuators, such as increased cyclic actuation frequency via fluid flow. L-PBF involves many manufacturing process parameters such as laser power, scan speed, hatch space (distance between two adjacent passes of the laser beam within the same layer), scan pattern, and channel orientation, among others. These parameters drive the thermal histories within the processed material during fabrication, and in turn have a direct influence on various attributes of a material such as microstructure and surface roughness. The effects of L-PBF process parameters on porosity [35], the martensitic transformation temperature [36], and the evaporation of Ni [37] have been studied in literature for as-fabricated NiTi, however, no prior studies have reported the effects of these parameters on surface roughness.

Although L-PBF can be used to fabricate actuators with complex internal features such as

channels, the surface roughness of as-fabricated L-PBF parts, in general, does not have the same surface quality with traditional high-precision machining processes [38, 39]. It has been documented that process parameters which result in higher energy density lead to lower as-fabricated surface roughness for top surfaces [39, 40, 41], however this trend is not found for side surfaces [39, 41]. When specifically considering the interior features of L-PBF parts, surface roughness is typically even higher primarily due to features being supported by powder feedstock in contrast to solid bulk support [42], and this is especially noticeable on side or overhanging surfaces [43]. Since powder support has poorer heat dissipation than bulk support, larger and nonuniform melt pools created during laser scans result in higher surface roughness and, for overhanging surfaces, the formation of stalactite patterns from the melt penetrating into loose powder [43, 44]. The surface roughness of channels can impact heat transfer properties, flow speeds of thermal fluids, and interfacial applications, such as coatings. Moderate and Gaussian distributed roughness can be useful for improving coating adhesion [45], while high roughness can improve fluid mixing at flow-related boundary layers and increase the rate of heat transfer [46, 47]. On the other hand, depending on the size of a desired channel, surface roughness may be on the order of magnitude of the channel diameter and could obstruct a channel, preventing fluid flow altogether. Thus, supplementary post-process operations, such as electropolishing, are required to improve the surface quality of channels.

Therefore, it is of great importance to understand the effects of process parameters influencing surface roughness in as-fabricated L-PBF parts in NiTi. In this thesis, a systematic effort is presented to understand the relationships between these parameters and the surface roughness of as-fabricated NiTi parts, with emphasis on the roughness of interior channels. Second, this thesis presents efforts on post-processing L-PBF NiTi parts using electropolishing to improve surface quality and further establishes a relationship between process parameters and electropolished surface roughness.

1.2.3 Review of Liquid Metal-Induced Corrosion on the Constituents of SMAs

As discussed, room-temperature liquid metals can be utilized as more effective heat transfer fluid for forced fluid convection than air or water [21]. Gallium and its common alloys, eutectic gallium-indium (E-GaIn) and eutectic gallium-indium-tin (E-GaInSn), are non-toxic, room-temperature liquid metals with extremely low vapor pressure, especially in contrast to the common alternative, mercury [10, 48]. E-GaIn is an enabling fluid for many microfluidic devices that incorporate flexible electronics and tunable RF devices due to its high electrical conductivity and physical reconfigurability [11, 49, 12, 50, 51, 52, 53, 54, 55]. Implemented as a vascular channel, geometrically configured liquid metal circuits can be introduced into bulk materials ranging from soft elastomers to fiber-reinforced composites. Embedded E-GaIn channels configured into helical coils and properly supplied electrical power can enable rapid and distributed induction heating for large SMA structures [13, 14]. Further, E-GaIn acts as an effective coolant due to its high coefficient of thermal conductivity and thermal diffusivity compared to water or polymer-based coolants; its high boiling point ($>$1300°C) also allows it to withstand the $>$200°C local temperatures that can arise in SMA components [21]. E-GaIn will also not degrade over time from thermal cycling unlike that of polymer-based coolants; the only degradation mechanism for E-GaIn would be surface oxide formation but, given the appropriate system design, E-GaIn can flow without disturbances to its stable oxide layer on its surface. Thus, a multifunctional E-GaIn fluidic system included in the SMA actuator can leverage these properties, permitting liquid metal cooling channels that also have geometric patterns amenable to induction heating as a primary actuator heating route.

In the past, high-temperature liquid metals such as lithium or sodium were considered as cooling fluids for nuclear reactors due to their high thermal stability and thermal conductivity [8, 9, 56]; ultimately, the aggressive corrosive mechanism associated with solid metal-liquid metal interfaces rendered many practices unsustainable [57, 58, 59, 60]. Local temperatures in SMA components fabricated from some compositions (e.g., $Ni_{49}Ti_{36}Hf_{15}$ [61]) can readily reach temperatures of 200°C, giving E-GaIn, with its high boiling point, an additional advantage over water. However, there is a major concern of how liquid gallium alloys interact with the NiTi SMAs themselves and

even copper electrical interconnects during long-term exposures at elevated temperatures. Two destructive phenomena are associated with liquid metal exposure to solid metals and have been segregated as: liquid metal-induced corrosion and liquid metal-induced embrittlement. The occurrence of these phenomena can be independent of each other and are specific to certain liquid-metal/solid-metal couples [57]. Liquid metal corrosion reactions are governed by several mechanisms including: dissolution, interstitial reactions, alloying, and compound reductions [62], where dissolution and alloying is more relevant for the proposed work. Dissolution is the release of metal atoms from the solid metal into solution with liquid metal, while alloying is the formation of stable products (i.e., intermetallics) on the solid-metal/liquid-metal interface. Under ideal isothermal static-liquid metal conditions, dissolution occurs until the solid elemental concentration becomes equal to the solubility of the liquid metal; however, very low solubilities, $<1\%$, can effectively result in immediate alloying, if corrosion is to occur. Further, thin intermetallic layers still form on interfaces from systems undergoing dissolution due to the net elemental flux of solid species into the liquid metal [62]. Meanwhile, liquid metal-induced embrittlement is described as the drastic reduction of fracture resistance of typically ductile solid metal by liquid metal weakening the metallic bonding of dissimilar solid metals; when a tensile stress is applied to a solid metal in the presence of a liquid metal, the latter will quickly propagate through a crack tip or grain boundaries, resulting in brittle failure [58]. To successfully implement the proposed liquid metal-enabled SMA actuator, these phenomena must be considered and mitigated.

The extent of gallium-based liquid metal interactions with nickel-titanium alloys is not known. Further, copper at temperatures around the SMA maximum working temperature of 200°C, is also not well investigated. Currently, there is one preliminary investigation [63] on the liquid metal-induced corrosion of nickel-titanium alloys by gallium, which did not detect corrosion on $Ni_{50}Ti_{50}$ or elemental Ti but did observe significant corrosion with elemental Ni and elemental Cu at the tested temperature of 220°C exposed for 300 h. Further, there is only one source with quantifiable information on E-GaInSn-induced corrosion on various metals of interest; originating from Migaj et al. [64], a 1978 untranslated Soviet study found in the review paper, [21], there was negligible

mass change for both Ni/E-GaInSn and Ti/E-GaInSn, while the Cu/E-GaInSn couple resulted in dissolution with a mass loss of 0.002 g/m^{2}h at room-temperature. More recently in 1998, Barbier et al. [60] tested the Ni/Ga couple which showed alloying as the dominate corrosion type with a growth of 0.21 mm/day at 400°C, providing insight into the effects of liquid gallium interactions on 316 L austenitic stainless steel (12 wt.% Ni).

Longer exposures and higher temperatures are required to further assess the viability of liquid metal with SMAs and determine the mechanisms as to the observed corrosion found on the pure Ni, while there was no interaction found in nickel-titanium systems. This work aims to further elucidate the interactions of gallium, E-GaIn, and E-GaInSn on equiatomic nickel-titanium ($Ni_{50}Ti_{50}$), nickel-rich nickel-titanium ($Ni_{55}Ti_{45}$), and a nickel-titanium-hafnium alloy ($Ni_{49}Ti_{36}Hf_{15}$) and determine at what conditions and how a nickel-titanium alloy will corrode from liquid metal exposure. Multiple liquid metals are investigated, as minor additions can result in varying of the liquid metal-induced corrosion [57] and to better elucidate the influence of each component (Ga, In, or Sn).

To simulate long term exposures at high actuator working temperatures, solid metal specimens would be exposed for up to 1200 h at 220°C. $Ni_{55}Ti_{45}$ and Ti would be exposed to temperatures as high as 950°C to further elucidate their lack of liquid metal-induced interaction at 220°C. Further, a separate test would include $Ni_{50}Ti_{50}$ thermally cycled from 35°C to 220°C, undergoing the shape memory effect, while immersed in E-GaIn to observe if martensitic transformations that occur at the surface augment possible corrosion. This work would compare the SMA interactions to those of its elemental components in the form of both commercially pure 200 nickel alloy (Ni) and grade 2 titanium alloy (Ti). Last, due to concern of liquid metal-induced attack when liquid metal is in contact with copper electrical leads, common in liquid metal RF applications, this work would investigate corrosion on electrical grade 110 copper (Cu). Observations would include the cross-sectional morphology, reaction layer chemistry, and assessment of diffusion into the solid metal primarily using electron-based characterization techniques. Mechanisms that could prevent nickel-titanium from low-temperature corrosion would also be identified.

1.3 Computational Modeling of a Liquid Metal SMA Actuator Showing Viability as a High Frequency Actuator[1]

To further motivate this thesis, computational efforts have been previously performed showing the significant improvements of a liquid metal integrated SMA actuator over one traditionally heated and cooled.

The heating and cooling rates of an SMA-liquid metal composite actuator were first assessed and compared to those associated with traditional induction heating and cooling methods for SMA actuators using preliminary COMSOL Multiphysics thermoelectric modeling. For this initial proof-of-concept study, only the critical region within an SMA actuator to be heated and cooled is considered. Specifically, the coil region near the root of the beam actuator is considered (Fig. 1.2) and assumed to be an axisymmetric disk. To model actuator heating (i.e., reverse transformation), a 2D axisymmetric SMA domain with a radius r_{SMA}=15 mm and thickness t_{SMA}=4.5 mm is considered, as shown in Fig. 1.3. The baseline prediction associated with traditional induction techniques [19, 13, 14] is modeled by considering five copper wires of radius r_{wire}=1 mm spaced 0.65 mm apart, corresponding to concentric rings that approximate a spiral induction coil with N=5 turns placed on the positive z-surface of the SMA component. Alternatively, a structurally embedded, spiral-configured, liquid metal-filled channel with the same N=5 turns is represented using five channels having a semicircular cross-section with the same radius of $r_{channel}$=1 mm also spaced 0.65 mm apart. These two models (traditional and structurally embedded) are illustrated in Fig. 1.3. It should be noted that the transformation behavior and in particular the latent heat properties of the SMA are not considered in these computational analyses, as they serve only as a proof-of-concept demonstration of potential heating and cooling capabilities of the proposed method. In [65] it is shown that a 10%-20% error might be introduced by the omission of these considerations. The SMA is currently modeled assuming a thermal conductivity k=18 W/m°C and a heat capacity C_p=400 J/kg°C, as taken from [13], but future work considering direct experimental and

[1]Part of the data reported in this section is reprinted with permission from "Towards High-Frequency Shape Memory Alloy Actuators Incorporating Liquid Metal Energy Circuits" by Hartl et al., 2017. *Shape Memory and Superelasticity*, 3, 457-466, Copyright 2018 by Springer Nature.

computational comparisons must consider the thermal consequences of latent heat transformation.

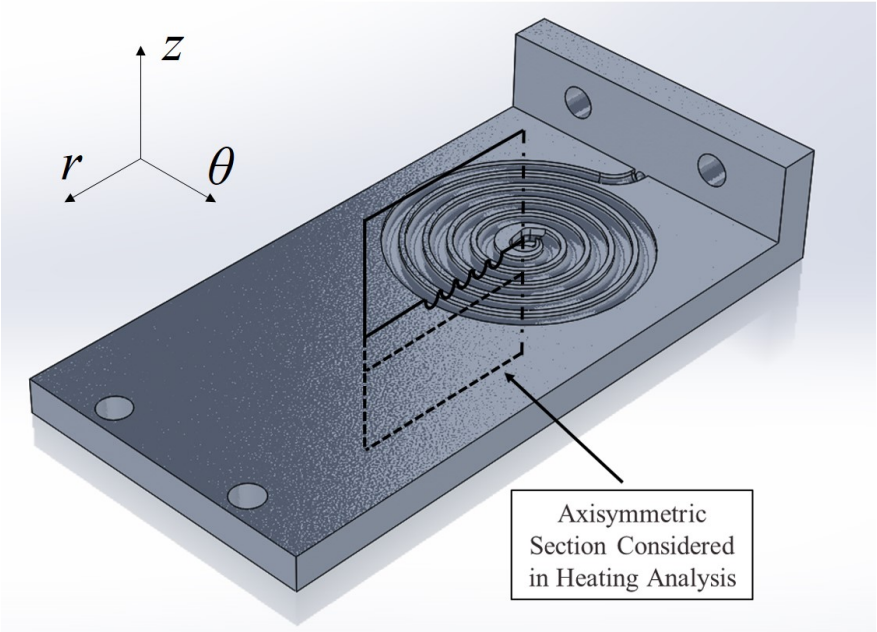

Figure 1.2: Example of an SMA-liquid metal composite beam actuator. The root of this cantilever beam lies on the -r side with 2 holes for mounting. The planar induction channel is embedded onto the top surface of the cantilever on the root side. There are two ports to the induction channel out the -r face and the -z face. The tip of the cantilever, located on the +r side, has two holes for applying a load.

Based on prior induction heating studies [19, 13, 14], our analyses assume an inductive signal frequency of f=150 kHz and a current I=20 A applied to each coil for 60 seconds. Fig. 1.4a compares the temperature on the positive z-surface of the actuator along the axis of symmetry in each model (see Fig. 1.3). The solid lines account for the induction heating of the SMA as well as the Joule heating (JH) of the induction coils themselves and the conduction of this heat into the surrounding matrix. The dashed line represents a study in which the liquid metal domain is considered only electromagnetically (i.e., heat is only generated in the SMA domain via induction) and Joule heating of the coil itself is neglected, while the dotted line represents a study that considers only the Joule heating of the coil. Notice that the structurally embedded SMA-liquid

metal actuator schemes considering only induction or only Joule heating are predicted to provide a nearly identical moderate increase in heating rate. This similarity is believed to be due to the following: 1) the application of the same amount of power to the system in both cases and 2) the relatively small size of the SMA domain considered leading to a homogenized temperature field. Both the qualitative differences in the two heating approaches and the relative thermal homogeneity generated by each in the time considered are shown in Fig. 1.5. However, the change in heating rate is doubled when both induction heating and the direct resistive heating of the liquid metal coil itself are considered (i.e. the additional Joule heating generated in the coil is allowed to pass into the SMA), as the heat associated with the high electrical resistivity coil combined with the large contact area between the embedded coil and SMA material almost doubles the rate of total heat generation in the actuator. Ultimately, using a traditional induction coil corresponds to a predicted temperature increase of approximately 40°C in 60 seconds, while a structurally embedded SMA-liquid metal energy circuit increases the temperature by over 100°C in the same amount of time given the exact same frequency and current inputs (Fig. 1.4a).

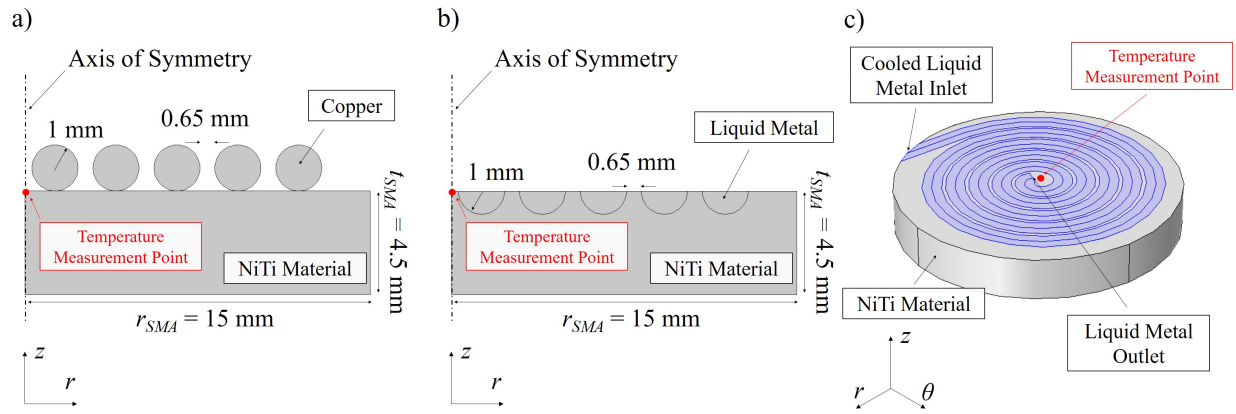

Figure 1.3: SMA beam actuator region considered during heating and cooling analyses (cf., Fig.1). a) 2D axisymmetric model approximating traditional external induction coil. b) 2D axisymmetric model approximating structurally embedded liquid metal induction coil. c) 3D model illustrating the cooling effect of flowing liquid metal through the coil.

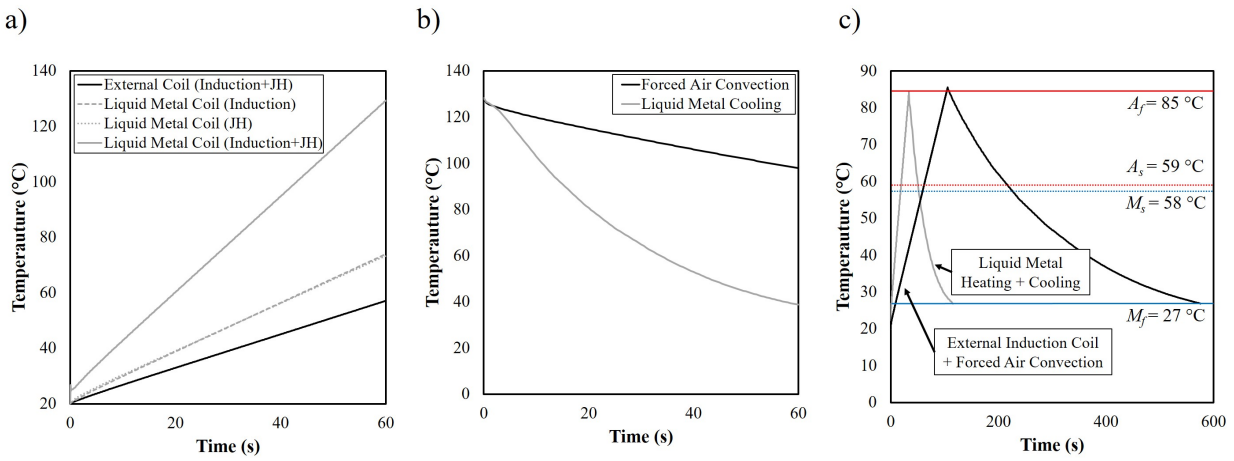

Figure 1.4: Results of computational heating and cooling analyses. a) Comparison of traditional induction heating approach and embedded liquid metal induction heating for an SMA component. b) Comparison of traditional external air flow approach and liquid metal cooling for an SMA component. c) Prediction of full cyclic actuation frequency using SMA transformation temperatures taken from SLM-fabricated NiTi.

For actuator cooling (i.e., forward transformation), a 3D model (Fig. 1.3c) is generated based on the 2D representation comprising the heating model. An SMA domain having a radius r_{SMA}=15 mm and a thickness t_{SMA}=4.5 mm is modeled as containing a spiraled planar channel with N=5 turns, an inner radius $r_{channel, i}$=1 mm, and an outer radius $r_{channel, o}$= 13 mm. The cross-section of the liquid metal channel remains semicircular with a radius $r_{channel}$=1 mm. The initial (hot) temperatures for this cooling analysis are determined by mapping the distributed final temperature fields from the previous 2D induction heating models onto the 3D model. To form a baseline prediction based on traditional cooling techniques, the SMA actuator is assessed with the Heat Transfer in Solids module in COMSOL and assumed to have forced air flowing over all exterior surfaces with a velocity of 1 m/s, corresponding to an effective convective coefficient of 21.6 W/m^{2}K [66]. To consider the case of the SMA-liquid metal actuator, the model considers liquid metal flowed through the spiral coil, dissipating heat from the SMA domain internally; this is performed using the Heat Transfer in Pipes module in COMSOL. The surface roughness of the coil is assumed to be R_q = 0.05 mm, derived from the characterization of L-PBF NiTi samples. The

initial liquid metal temperature inside the coil is set equal to the temperature of the surrounding SMA, the distribution of which is taken from the end of the inductive heating model as discussed above. The liquid metal is assumed to flow into the inlet at a rate of 9.42 mL/min (0.1 m/s) and at a temperature of 27°C. Fig.3b shows the temperature change at the center of the coil on the positive z-face during cooling for these two methods. Within 60 seconds, a traditional external airflow cools the component by approximately 30°C within 60 seconds, while liquid metal flowing through the component is able to reduce its temperature by nearly 90°C in the same amount of time.

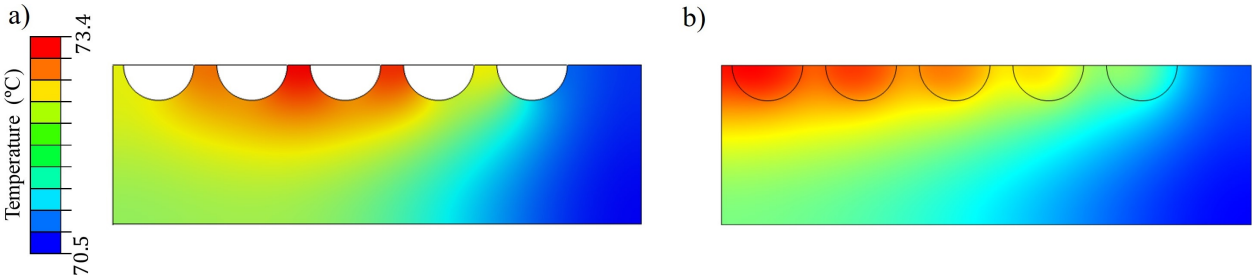

Figure 1.5: Predicted temperature contours when considering a) only induction heating and b) only Joule heating of the liquid metal-SMA composite actuator. Note that the relatively small size of the SMA domain and large time taken to heat (i.e., low power) lead to a relatively homogenous temperature distribution within the component.

Combining heating and cooling modeling and given estimates for the transformation temperatures of the SMA material to be produced from preliminary testing, the overall increase in the full cyclic actuation frequency of the liquid metal-augmented actuator (structurally embedded induction coil and liquid metal vascular flow) is predicted to be nearly five times greater than the traditional approach (surface-mounted induction coil and external air flow) (see Fig. 1.4c). Specifically, utilizing liquid metal energy circuits results in a full cycle actuation period of 116 seconds, while the traditional methods require an actuation period of 576 seconds. Given these results, efforts toward experimental demonstrations of the concept are well motivated.

1.4 Thesis Summary

The major goal of this work is to incorporate liquid E-GaIn channels into NiTi SMA actuators to increase the shape memory effect actuation frequency. This goal will be accomplished by utilizing a synergistic approach that integrates research on SMA materials and actuators, micro-vascular cooling, room-temperature liquid metals, reconfigurable liquid metal electronics, and production of complex SMA components using L-PBF; thus, the previous limitations regarding SMA actuator power density can be addressed. This work will be supported with studies laying the groundwork for future modifications of such a device as it will investigate on the surface quality of fully interior channels created by L-PBF techniques and investigate the interactions of direct liquid metal contact on NiTi SMAs.

1. Successfully demonstrate a NiTi shape memory alloy produced via laser powder-bed fusion heated and cooled with liquid gallium-based energy circuits

2. Investigate the effects of laser powder-bed fusion printing parameters on interior channel formation and mitigate their high roughness using electro-polishing techniques

3. Investigate liquid metal-induced corrosion of gallium alloys on NiTi and its related alloys

2. EXPERIMENTAL

2.1 Designing and Testing of a Liquid Metal SMA Actuator[2]

This work represents a major effort to demonstrate the production and experimental characterization of an liquid metal SMA actuator undergoing full cyclic operation. A fully functional SMA actuator component entails structurally embedded spiral channels produced by L-PBF AM, with an electrically insulating coating later applied to the channel surface, as represented in Fig. 2.1. We consider a bending beam actuator with a planar spiral channel near the cantilevered end of the beam. The planar spiral channel has an open cross-section for ease of access, specifically enabling the application of the chosen electrically insulating coating. A cyclic operation entails:

1. The spiral channels are filled with static liquid metal, allowing for distributed induction heating when provided with the appropriate input signals

2. The current required for sufficient induction heating also contributes towards direct Joule heating of the liquid metal itself, further leading to increased heating rates, thus driving reverse martensitic transformation

3. After device actuation, cooled liquid metal is then flowed through these channels to remove heat from the domain, substantially increasing cooling rate and driving forward martensitic transformation.

A diagram of the proposed liquid metal driven SMA actuator is shown in Fig. 2.2. The actuator channel will be interfaced with heat-resistant polymer tubing via ceramic inserts installed on both openings of the actuator channel. A syringe pump would drive liquid metal to the tubing which will pass in series through an ice bath, the actuator coil, and a liquid metal reservoir. The AC source for induction heating will be a self-tuning Roy 1500 induction power supply. Various

[2]Part of the data reported in this section is reprinted with permission from "Towards High-Frequency Shape Memory Alloy Actuators Incorporating Liquid Metal Energy Circuits" by Hartl et al., 2017. *Shape Memory and Superelasticity*, 3, 457-466, Copyright 2018 by Springer Nature.

Figure 2.1: A liquid metal filled external surface channel embedded the configuration of a planar induction coil in an SMA produced via L-PBF. The black surface is a Xylan®polymer coating isolating the shiny liquid metal.

sensors will be positioned to measure the inputs: electrical current, voltage, and frequency applied by the induction power supply. The outputs will be: tip displacement and temperature distribution throughout the SMA beam. The tip displacement will be measured using a Keyence laser displacement sensor IL-600 with 0.01 mm resolution. The electrical voltage, current, and frequency will be measured using a Tektronix TCP303 current probe with a TCPA300 amplier and a Tektronix TDS1012 oscilloscope. The surface temperature distribution of the Kapton-covered SMA actuator will be acquired using a FLIR A600 thermal camera.

2.1.1 Setup of the Liquid Metal SMA Actuator

Preliminary computational modeling (see Section 1.3) has successfully demonstrated the potential benefits of using a structurally embedded liquid metal channel as both an induction coil and as a vascular system for internally circulated heat transfer fluid. A prototype of the SMA beam actuator with a planar coil near its root was then produced, as shown in Fig. 2.3 on a commercial ProX 100 L-PBF system. Precursor powder supplied by NANOVAL was composed of gas-atomized NiTi (50.9 wt. % Ni) particles with d_{50} = 19.6 μm. Manufacturing parameters for the part included a laser power of 50 W, laser speed of 80 mm/s, and hatch spacing of 120 m, with the laser rastering in the 45°/45°directions relative to the beam length. The hatch spacing refers to the distance between two adjacent passes of the laser beam within the same layer. The fabricated SMA beam had a nominal length of 70 mm, a width of 40 mm, and a thickness of 4 mm. The spiral

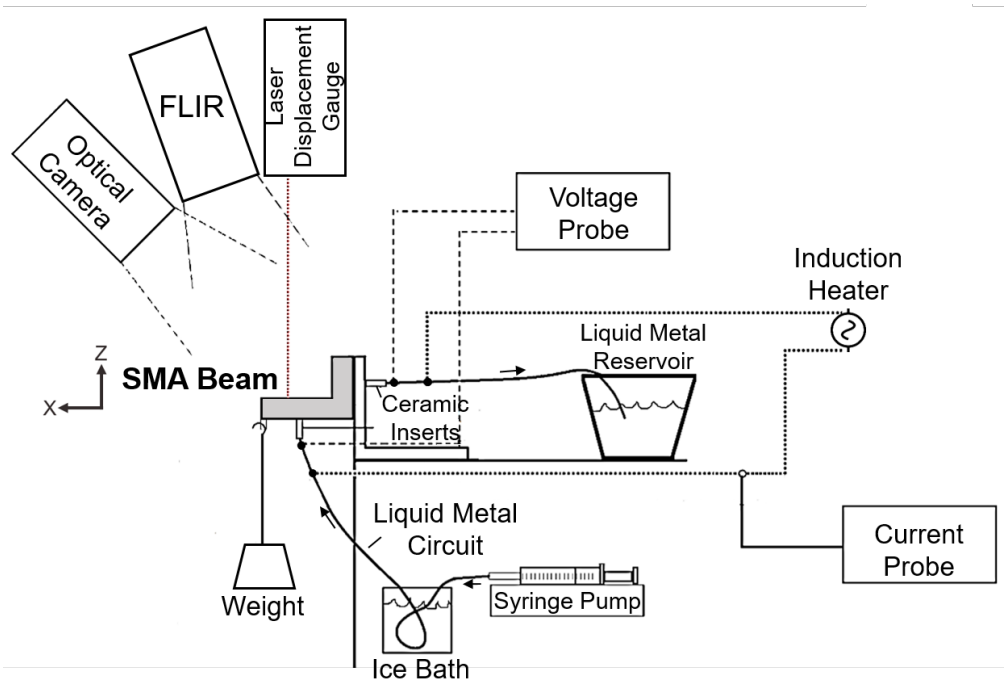

Figure 2.2: A digram of the proposed experimental setup of the liquid metal driven SMA actuator. An inductive heater power unit supplies RF signal to the embedded liquid metal induction coil to heat the SMA. Liquid metal is flowed via a syringe pump, through the embedded induction coil to cool the SMA. Multiple probes and cameras are used to record thermal data, RF signal, and displacement.

induction coil configuration was matched to that considered in the computational model, having a semi-circular open cross-section and being comprised of 5 turns with a channel radius of 1 mm and a spacing between turns of 1.4 mm. The open channel design was necessary for the development of a procedure for applying an electrically insulating coating.

Preventing an electrical short circuit between the liquid metal and bulk SMA is critical to actuator operation since even a moderate current leakage can undermine inductive heat generation by the coil. The inner surface of the spiral coil was coated with the black Xlyan® fluoropolymer supplied by Whitford. The coating procedure consisted of first applying Xylan® 8251 via air-brush, which was then cured at 250°C for 12 minutes, followed by a second identical coat and heat treatment. This polymer was used as it was a high temperature polymer that can adhere well to metal surfaces and can be applied via a single wet solution, rather than chemical vapor deposition

or some type of two-part mixture. The coated channel region (i.e., the black region in Fig. 2.3) was then covered with a self-adhesive Kapton® film to contain the liquid metal during flow for cooling. This Kapton® film was subsequently found to limit the liquid metal flow rate by the tendency of this film to debond from the SMA given sufficient channel pressure.

The coated actuator channel interfaced with the liquid metal flow circuit (i.e., polymer tubing) via ceramic inserts installed on both ends of the actuator channel. A model New Era 501 syringe pump supplied liquid metal to the tubing at a precise rate. The liquid metal then passed through an ice bath, the actuator coil, and finally into a liquid metal reservoir. This is schematically shown in Fig. 2.2. The electrical connections passed current into the liquid metal-filled tubing near the ceramic inserts, which limited electrical current to within the SMA domain and prevented overheating of the polymer tubing. The AC source for induction heating was a self-tuning Roy 1500 induction power supply. As shown in Fig. 2.2, various sensors were positioned to measure actuator inputs and outputs. These included the following inputs: electrical current, voltage and frequency applied by the induction power supply, and the following outputs: tip displacement and temperature distribution throughout the SMA beam. The tip displacement was measured using a Keyence laser displacement sensor IL-600 with 0.01 mm resolution. The electrical voltage, current, and frequency were measured using a Tektronix TCP303 current probe with a TCPA300 amplifier and a Tektronix TDS1012 oscilloscope. The surface temperature distribution of the Kapton-covered SMA actuator was measured using a FLIR A600 thermal camera, where the Kapton® was measured to have an effective thermal emissivity of 0.95. For the purpose of the results that follow, temperature is taken as an average over the entire coil area, while for the purpose of experimental control temperature was measured at a point at the center of the planar coil.

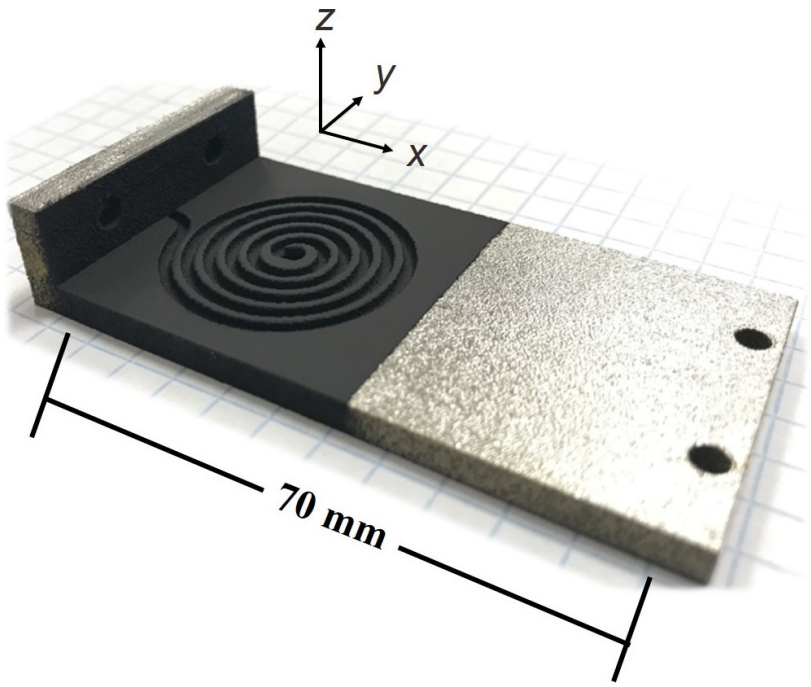

Figure 2.3: The fabricated SMA actuator beam with surface-accessible spiral channels and electrically insulating coating (black region) before liquid metal integration.

2.1.2 Experimental Procedures of the Liquid Metal SMA Actuator

The SMA actuator was mounted to a fixed structure and liquid metal was introduced via the tubing and ceramic inserts, as previously described in Fig. 2.2 and shown in Fig. 2.4a. The time history of the various experimental inputs is shown in Fig. 2.4b and corresponds to two heat/cool cycles. Starting at time (0), the SMA beam was inductively heated in an unloaded condition to the upper cycle temperature (UCT) at the center of the coil of 90°C to ensure that the specimen was initialized to an austenitic state. At time (1) the specimen was subjected to a nearly instantaneous tip load of 133 N (30 lbs) and then permitted to cool via natural convection (i.e., no liquid metal flow). At time (2), the beam was again inductively heated until the UCT was reached. At time (3), liquid metal was driven by the syringe pump through the ice bath and into the channel at a rate of 1 mL/min, cooling the actuator from within. Flow rates were limited to 1ml/min due to the aforementioned Kapton film debonding at sufficient channel pressures. At time (4), the available liquid metal in the syringe was exhausted and the beam continued to cool via natural convection

until the experiment was completed at 3000 seconds. During the experiment, the temperature distributions and beam tip displacement were continuously recorded, while the induction current and frequency were sampled once during the heating.

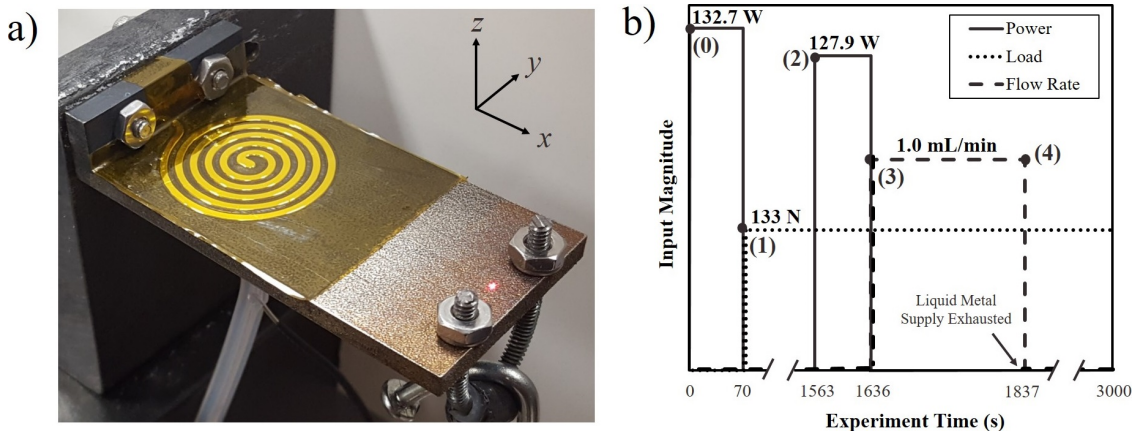

Figure 2.4: Experimental SMA-liquid metal actuator and associated experimental inputs. a) The SMA actuator beam with liquid metal filling the open-faced channel as covered with Kapton film. b) Schematic of the input levels during the experiment (applied power, actuator loading, and liquid metal flow rate) and actions performed from time (1) to time(4).

2.2 Investigating the Surface Quality Interior Channels of Laser Powder-Bed Fusion Nickel-Titanium

2.2.1 Experimental Design of the Interior Channel Surface Roughness Study

Table 2.1: Process parameters for the two-level fractional factorial design of experiments.

Process Parameter	Low level -		High level +
Laser Power [W]	45		50
Scan Speed [mm/s]	80		120
Hatch Space [μm]	35		120
Scan pattern [°]	-45°/+45°		0°/90°
Channel Orientation	Horizontal		Vertical
Independent Parameter			
Channel Diameter [mm]	1	1.5	2

The L-PBF system used to produce NiTi channel specimens was a commercial ProX 100 with a Gaussian profile fiber continuous wave laser with a wavelength of 1070 nm, a beam diameter of approximately 70 μm, and maximum laser power of 50 W. The builds took place under a high purity argon protective inert atmosphere to minimize oxidation [67] on a NiTi substrate with an average areal surface roughness of 2.5 μm. The powder layer thickness was fixed at 30 μm for all builds. The precursor powder was supplied by Nanoval was produced from NiTi ingots (50.9 at. % Ni) through gas atomization under argon. The powder particles diameters ranged between 15-45 μm with the median diameter, D50, $<$ 19.6 μm. Fig. 2.5e depicts a representative secondary electron micrograph using scanning electron microscopy (SEM) of the powder, demonstrating a dominantly spherical morphology.

A two-level fractional factorial design of experiments [68] was employed to study the relationship between five L-PBF process parameters and the surface roughness of interior channels in as-fabricated NiTi. The process parameters are listed in Table 2.1 and include: laser power [W], scan speed [mm/s], hatch space [μm], scan pattern [-45°/+45°, 0°/90°], and channel orientation [horizontal (H), vertical (V)]. The L16 design matrix, shown in Table 2.2, presents combinations of high and low factor levels (+ and -, respectively) for each channel. Channels with horizontal and vertical build orientation are denoted by H1-H8 and V1-V8, respectively. Further, the design matrix was repeated independently to consider a total of three channel diameters [mm].

Table 2.2: Design of experiments matrix representing combinations of the five process parameters.

Channel	Laser Power [W]	Scan Speed [mm/s]	Hatch Space [μm]	Scan Pattern [-45°/+45°, 0°/90°]	Channel Orient. [H, V]
H1	-	-	-	-	-
H2	+	+	-	-	-
H3	+	-	+	-	-
H4	-	+	+	-	-
H5	+	-	-	+	-
H6	-	+	-	+	-
H7	-	-	+	+	-
H8	+	+	+	+	-
V1	+	-	-	-	+
V2	-	+	-	-	+
V3	-	-	+	-	+
V4	+	+	+	-	+
V5	-	-	-	+	+
V6	+	+	-	+	+
V7	+	-	+	+	+
V8	-	+	+	+	+

The difference in laser power was constrained by the ProX 100 system's maximum laser power and the high power required to melt NiTi, thus 50 W and 45 W were selected. Scan speed and hatch space values were selected based on successful preliminary builds of channels; success was determined by part density and the absence of part cracking. Scan pattern and channel orientation were two out of the five factors representing process parameters that are not directly correlated to L-PBF system laser energy density. Scan pattern values were chosen to observe any geometrically effects upon the build-up of channels.

Channel orientation was included as a factor because it has been reported to have a strong effect on the properties of additively manufactured parts, including surface roughness [39, 44]. Fig. 2.5a depicts the fabrication of vertically and horizontally oriented channels. For horizontal channels, the first few layers comprise of the bottom floor of the channel and are supported by solidified bulk material underneath. Thus, it is expected that the floor will have a surface quality similar to that of

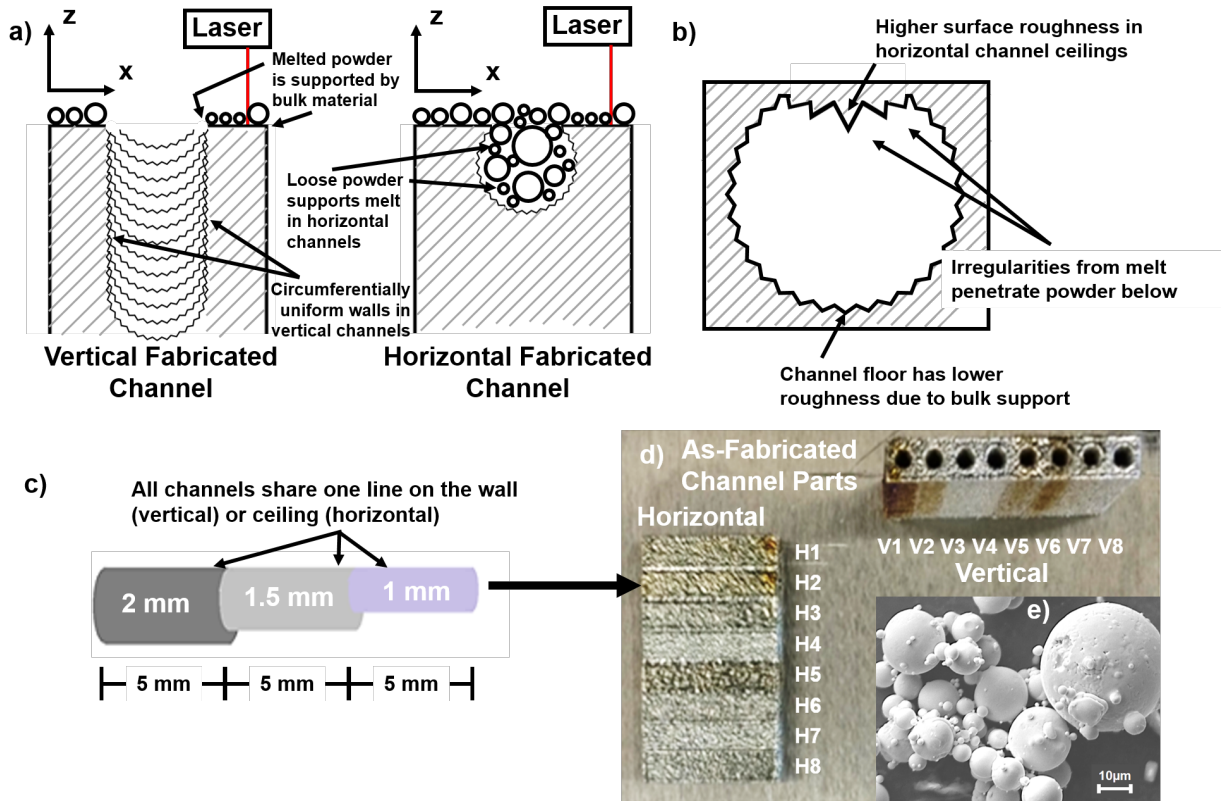

Figure 2.5: (a) Diagram depicting the origin of surface roughness differences between vertically and horizontally oriented interior channels. (b) Diagram showing the higher surface roughness associated with the overhangs in horizontally oriented interior channels after powder has been removed. (c) All three diameters in a given channel lie on a single line for facile measurement; channel diameters step every 5 mm. (d) Finished channel parts with their respective parameter sets (e) SEM micrograph of NiTi powder.

an ordinary top flat surface produced by L-PBF. The last few layers of building a horizontal channel comprise of the ceiling of the channel and is supported by loose powder. As the ceiling is being completed layer-by-layer, molten metal can penetrate into the powder support underneath, leading to undesired solidified material that manifests itself as large peaks and high surface roughness as depicted in Fig. 2.5b. Vertical channels are expected to have a more circumferentially uniform surface roughness as there are no floors and ceilings but only walls. Vertical channel build-up takes place over the circumferential channel outline, which is composed of solid bulk material from previous layers but can runoff into the neighboring powder of the unmelted channel. Alternatively, channel orientation can be viewed as a up-skin/down-skin/in-skin parameter, like that specified in Calignano et al [40]. The vertical channels surfaces can be viewed as the in-skin; the horizontal channel floor can be viewed as the up-skin, while the horizontal channel ceiling is the down-skin. However, the horizontal channel floor is not investigated in this study as it would be somewhat similar to ordinary flat surfaces.

Since the channel diameter translates to the width of powder supported ceiling, multiple channel diameters (1 mm, 1.5 mm, and 2 mm; Fig. 2.5c) were also investigated as a parameter independent of the other process parameters specified in the design matrix. The smallest of the three sizes was chosen based on preliminary experiments showing that the lowest patent channel size obtained with the tested parameters was 0.7-1.0 mm in diameter; the largest of the three sizes was chosen as it was the channel size of the liquid metal/SMA actuator [22, 23].

Powder layer thickness was kept constant due to the amount of separate builds it would require. A value of 30μm was chosen based on previous literature reporting lower mechanical properties of L-PBF NiTi parts with higher layer thicknesses due to the reduced amount of energy reaching the underlying surface to achieve full melting and adequate bonding between layers [67].

2.2.2 Preparation and Measurement of the Interior Channel Surface Roughness Specimens

Without any observed part distortion during fabrication, two separate parts were produced with one part containing horizontal channels and the other containing vertical channels, shown in Fig. 2.5d. Each part has eight through-channels 15 mm in length, with each channel comprised of

three 5 mm length segments with different diameters (Fig. 2.5c). Two parts were chosen in order to easily align the three diameters to share one a single line on the vertical channel wall and horizontal channel ceiling. This would assist in maintaining a consistent distance from the surface during sectioning and subsequent measurements. Thus, forty-eight channels, each with a unique set of L-PBF process parameters and channel diameter, were created within the two parts.

The as-fabricated parts were subsequently cut from the build substrate using wire electrical discharge machining (EDM). Both parts were sectioned along their channel axes using a slow speed diamond precision cutting wheel, exposing their internal surfaces for surface roughness measurements and imaging. Sectioning was needed for two reasons: (1) to enable measurement of surface roughness, and (2) to facilitate electropolishing. After sectioning, channels were sonicated in a 1:1 ethanol/acetone mixture to remove cutting fluid and remove any loose powder from the surface.

The surface roughness was measured over an area of the exposed channels using a Zygo Zegage optical profilometer. The width of that area was decreased with respect to a decreasing channel diameter to minimize possible bias from radial effects, (i.e., measuring a profile perpendicularly unaligned to the instrument).To minimize this effect, the width was determined by drawing a chord through the channel cross-section perpendicularly from 98% of the channel radius. Thus, the dimensions of the measured area were 800μm long by 400μm wide for 2 mm channels. The width was linearly reduced to 300μm and 200 μm for 1.5 mm and 1 mm channels, respectively.

Surface roughness can be represented using different metrics, with one of the most common metric being the average areal surface roughness, S_a. However, it has been argued that the root-mean-square areal surface roughness, S_q, has a more physical foundation than S_a; for instance, S_q is directly related to surface energy and light scattering [69, 70]. In our study, we elect to report S_q values along with the profile skewness, which can be around 10%-20% higher than S_a values. We also elect to report S_{sk}, which represents the degree of bias of peaks or valleys, and the profile kurtosis, S_{ku}, which provides a measure of the spikiness of the area. One physical interpretation of skewness relates to lubrication retention, where negative values would have deep

valleys to retain lubrication. High kurtosis values (>3) imply the presence of sharp peaks and troughs which can affect coating application and wear, whereas low kurtosis values (<3) imply the presence of rolling hills and valleys. A surface with a Gaussian height distribution has a kurtosis value of 3 [70]. These three metrics provide a useful quantification of the surface roughness based on the engineering application proposed. Furthermore, secondary-electron SEM was conducted on a Tescan Vega 3 instrument to provide high-resolution micrographs, which represent useful qualitative data to corroborate the quantitative surface roughness data.

After measuring the surface roughness of as-fabricated channels, electropolishing was performed as a post-processing step based on a procedure by Pohl et al. [71] for NiTi alloys using a acetic/perchlorate acid electrolyte, as depicted in Fig. 2.6a. A nickel foil anode encompassed the interior of a beaker to ensure equal distance from the channels. The post-processing step took 25 min at 10 V. The channel parts were adhesively bonded to a copper wire-embedded rubber stopper and acted as the cathode. It is acknowledged that electropolishing would normally be non-uniform for high aspect ratio channels since the channel openings would be more affected than the channel center. A preliminary electropolish was conducted to quantify the mass loss associated from on as-fabricated features comparable to the size of the channels. Eight small 1.5 mm diameter pillars were fabricated in the build z-direction on a separate NiTi substrate (Fig. 2.6b), with the same eight process parameter combinations used to fabricate vertical channels V1-V8. After electropolishing the channel parts, the channels were subsequently reevaluated for surface roughness measurement and imaging.

Analysis of the data, based on the experimental design outlined in Section 2.1, was conducted to elucidate the effects of the process parameters on the channel surface roughness. This included: (1) analysis of variance (ANOVA) to identify the significance of each process parameter; (2) main effects plots to further support the results from ANOVA, and (3) response surface modeling to quantitatively express as-fabricated surface roughness as a function of process parameters.

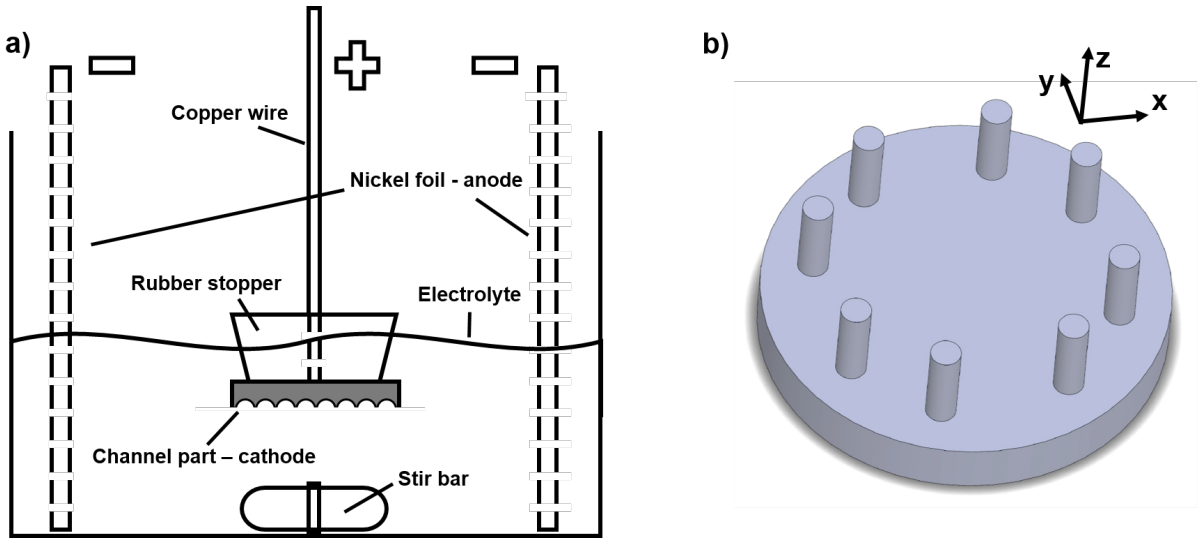

Figure 2.6: (a) Section view depicting the electropolishing experimental setup. (b) 3D model of the mass loss test piece built using processing parameters V1-V8 for its eight vertical pillars.

2.3 Investigating Liquid Metal-Induced Corrosion of Gallium Alloys on Nickel-Titanium

2.3.1 Materials

The six solid metals and three liquid metals under investigation are compiled with relevant material properties in Table 2.3.

The three nickel-titanium alloys were procured from excess material from previous SMA structural studies [4, 5]. Ni, Ti, and Cu were obtained from `Online Metals.com` in sheet form. Specimens were nominally 3.175 mm (1/8") thick except for 2 mm thick $Ni_{50}Ti_{50}$ and $Ni_{49}Ti_{36}Hf_{15}$. Material specimens were cut into rectangular prisms using a diamond-embedded, high-speed rotary blade. Widths ranged from 4-5.5 mm, while lengths ranged from 12-13 mm. Specimens were ground on all sides using SiC metallurgical paper with grits of 180 and then 320 to remove potential surface defects and preexisting surface oxides.

Gallium of 99.99% purity was supplied in ingot form by Alfa. The E-GaIn was produced by mixing gallium with 99.999% pure indium ingots supplied by the Materials Directorate of the Wright-Patterson Air Force Research Laboratory. E-GaInSn was supplied by Solution Materials, LLC, with a nominal composition of 68.5 wt.% Ga, 21.5 wt.% In, and 10 wt.% Sn.

Table 2.3: Relevant properties of the solid and liquid metals.

Material	Density	T_m	Nom. wt.%		
	[g cm^{-3}]	[°C]	Ni	Ti	Hf
Ni	8.91	1455	100	-	-
Ti	4.54	1668	-	100	-
$Ni_{50}Ti_{50}$	6.45	1310	55.0	45.0	-
$Ni_{55}Ti_{45}$	6.52	1120	60.0	40.0	-
$Ni_{49}Ti_{36}Hf_{15}$[72]	8.81	1300	38.5	23.0	36.0
Cu	8.96	1085	-	-	-
-	-	-	Ga	In	Sn
Ga [21]	5.91	30	100	-	-
E-GaIn [10]	6.25	15	75.0	25.0	-
E-GaInSn [48]	6.36	11	68.5	21.5	10.0

2.3.2 Testing and Measurement of the Liquid Metal-Induced Corrosion Specimens

Porcelain crucibles contained 5-7 g of static liquid metal with solid specimens placed such that one face was in contact with the bottom of the crucible; the low density of Ti resulted in the Ti floating on the liquid metal surface instead. Crucibles were complemented with porcelain lids and placed in an air-convection oven. Generally, solid metal specimens were exposed to each of the three liquid metals for at least 300 h at 220°C, while couples of particular interest were explored at longer exposures, as seen in Table 2.4. Additional Ti and $Ni_{55}Ti_{45}$ couples were exposed for 3 h up to 950°C temperatures. Crucibles were air-quenched upon oven removal.

Liquid metal was static during exposure, which could result in the liquid metal becoming saturated with dissolved solid metal. In a fluidics application, though there would be flow to replenish this saturated liquid metal, it would most likely still be contained in a limited reservoir which would eventually equilibrate.

For the experiment regarding the thermal cycling of $Ni_{50}Ti_{50}$, specimens were prepared similarly but in an E-GaIn-filled crucible on a computer-controlled hotplate. Temperatures were cycled from 35°C to 220°C for 300 and 600 h exposures using a custom python script, which resulted in approximately 135 and 270 cycles, respectively.

Table 2.4: Tested couples at 220°C denoted by an 'x'.

	Gallium			E-GaIn			E-GaInSn		
Exposure [h]	300	600	1200	300	600	1200	300	600	1200
Ni	x	x	x	x			x		
Ti	x			x			x		
$Ni_{50}Ti_{50}$	x	x	x	x	x	x	x	x	x
$Ni_{55}Ti_{45}$	x			x			x		
$Ni_{49}Ti_{36}Hf_{15}$	x	x	x	x			x		
Cu	x	x	x	x	x	x	x	x	x

After exposure, specimens were removed from their crucibles and sonicated across multiple steps using heated alcohols. The heat ensured that loosely adhered gallium did not solidify while the sonication removed the liquid metal, leaving behind only solid products on specimen surfaces. Specimens were weighed to measure either mass loss from dissolution or mass gain from alloying. Specimens were sectioned using a diamond-embedded, high-speed rotary blade to expose the cross-section and subsequently mounted in epoxy resin. Polishing steps included: SiC metallurgical paper of 180, 320, 400, 600, and 1200 grits followed by a polish of 1 μm and 0.3 μm alumina powder slurry from Metallurgical Supply Co., Inc. on a soft cloth pad. Polished samples were rinsed with ethanol and dried with compressed air.

The effects of the liquid metal on the specimens were assessed using a Tescan Vega 3 Scanning Electron Microscope (SEM), with both Secondary Electron (SE) imaging and Back-Scatter Electron (BSE) imaging, including Oxford Instruments Energy-Dispersive X-ray Spectroscopy (EDS). Stated EDS values contained a σ-value of 0.1 - 0.3. X-ray diffraction was used to corroborate the intermetallics found in the Ni specimens. The open-source Fiji plug-in *Analyze Stripes* [73] was used for image processing to measure edge surface roughness and thickness of reaction layers.

3. RESULTS

3.1 Results of the Liquid Metal SMA Actuator[3]

After undergoing the procedures with various metrologies outlined in Section 2.1, the liquid metal SMA actuator was heated, actuated, and cooled using the multifunctional liquid metal energy circuit.

Fig. 3.1a shows the mean temperature history of the SMA actuator coil region during the experiment, while Fig. 3.1b depicts the displacement of the beam tip as a function of the same temperature. Taking the deformed actuator after initial loading in the high-temperature state to be the reference configuration, the SMA beam tip deflected 14 mm during the initial cooling. Induction heating via the liquid metal circuit raised the temperature over the surface of the coil to 85°C in approximately 75 seconds (applied RMS current of 18.4 A, frequency of 63.2 kHz). As the surrounding SMA material reached the austenitic finish temperature, the actuator tip moved toward its reference position for a total upward displacement of 10 mm (a recovery of 71.4%), as illustrated in Fig. 3.1 and imaged in Fig. 3.2.

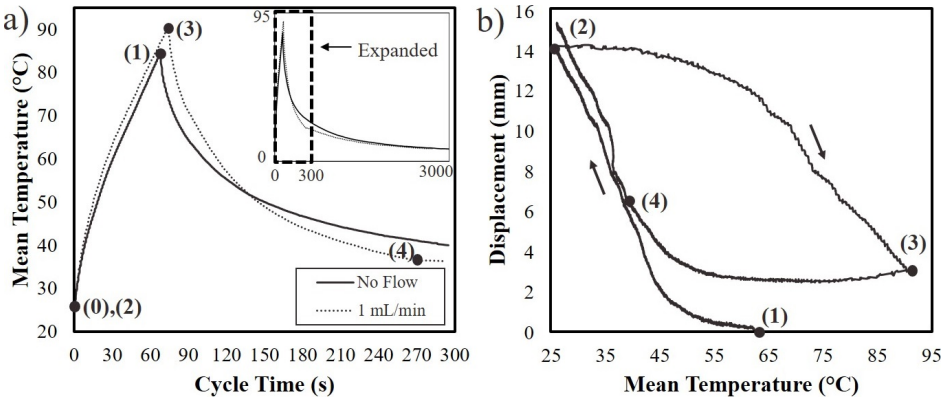

Figure 3.1: Prototype response subject to the inputs of Fig.6b. a) A comparison of actuator cooling rates with and without liquid metal flow. b) Displacement of the beam tip as a function of average temperature throughout the experiment.

[3]Part of the data reported in this section is reprinted with permission from "Towards High-Frequency Shape Memory Alloy Actuators Incorporating Liquid Metal Energy Circuits" by Hartl et al., 2017. *Shape Memory and Superelasticity*, 3, 457-466, Copyright 2018 by Springer Nature.

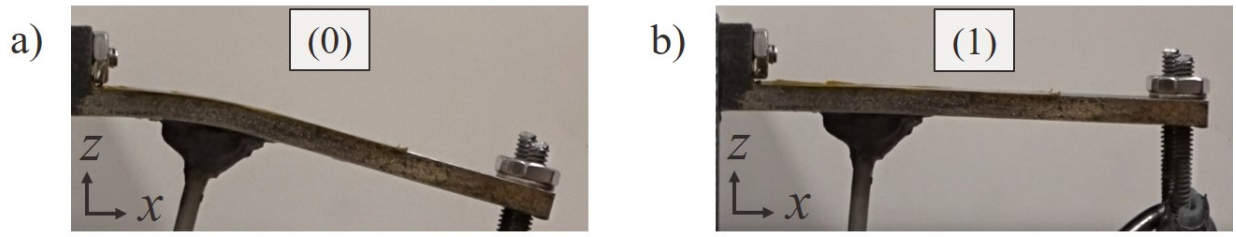

Figure 3.2: SMA actuator tip deflection a) before and b) after induction heating via the liquid metal coil. Note that induction heating resulted in a total upward motion of 10 mm, or a recovery of 71.4% of the initial deformation generated upon heating.

Subsequently, fresh liquid metal was flowed through the channel at a rate of 1.0 mL/min (time (3) to time (4)) until an average temperature of approximately 25°C was again reached. In cooling from 85°C to 37°C (i.e., the temperature at which the liquid metal supply was exhausted), it was found that in the no-flow case (time (1) to time immediately before time (2)) cooling required 311.0 seconds to complete, while for the liquid metal flow case (time (3) to time (4)) cooling required 183.9 seconds. This corresponds to a 40.9% reduction in the cooling time for a low liquid metal flow rate (compare to 9.42 mL/min in the computational study, which is a goal for future experimental studies). Ultimately, the actuation frequency of the SMA-liquid metal actuator without flow was 0.0026 Hz, while the actuation frequency with the slow flow rate of 1 ml/min was 0.0037 Hz. Fig. 3.3 depicts example temperature profiles of the SMA beam actuator during both induction heating and liquid metal cooling. In Fig. 3.3b, note the centrally located temperature reduction due to the low-temperature liquid metal entering the middle of the coil and drawing heat from the SMA domain as it flows spirally outward.

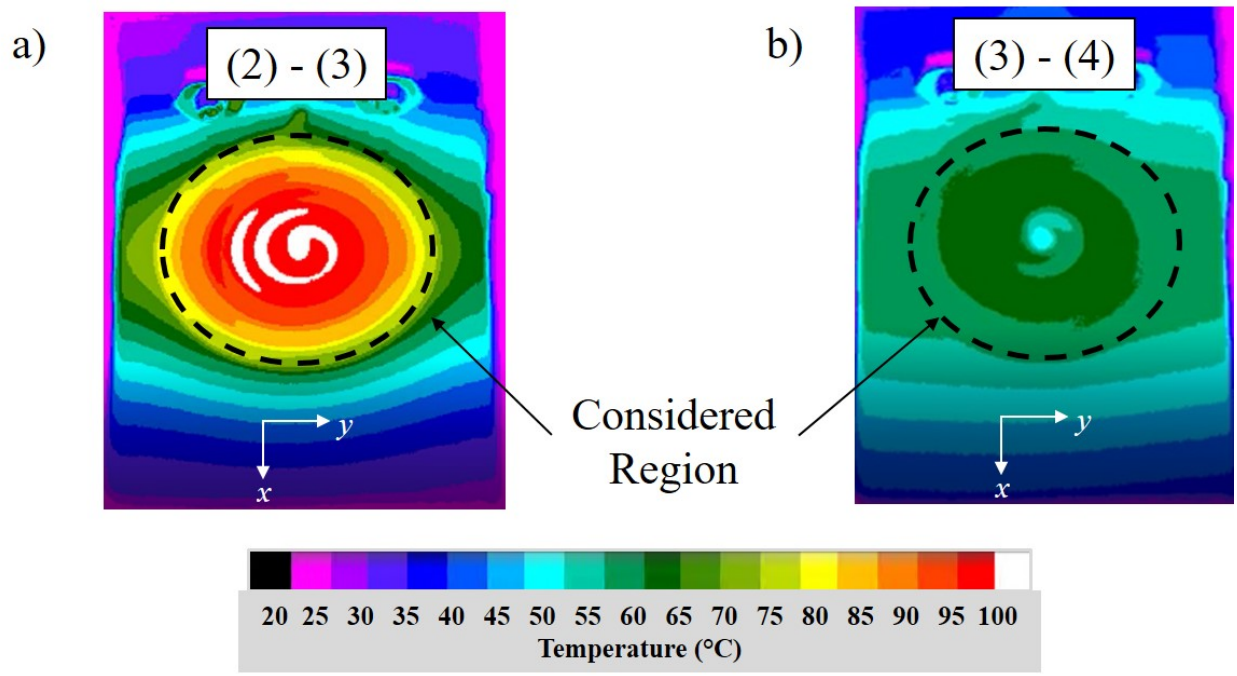

Figure 3.3: Temperature profiles of the SMA beam actuator during a) induction heating via the liquid metal coil and b) forced convective cooling associated with liquid metal flow through the coil. The considered region has been highlighted for reference.

After the conclusion of the experiment, additional computational studies were conducted to assess SMA beam actuator cooling rates at these less aggressive liquid metal flow rates by using the same 3D model discussed in Section 1.3 but considering a liquid metal flowing at a rate of 1.0 mL/min as in the experiment described above. As seen in Fig. 3.4, the results of these analyses predict that cooling from 85°C to 37°C require 175.0 seconds, which is in good agreement with the experimental results (183.9 seconds). Table 3.1 places these results in the context of other large monolithic SMA actuators (beams and tubes) of similar size. Further research at higher liquid metal flow rates will further improve the actuation frequency of the current concept.

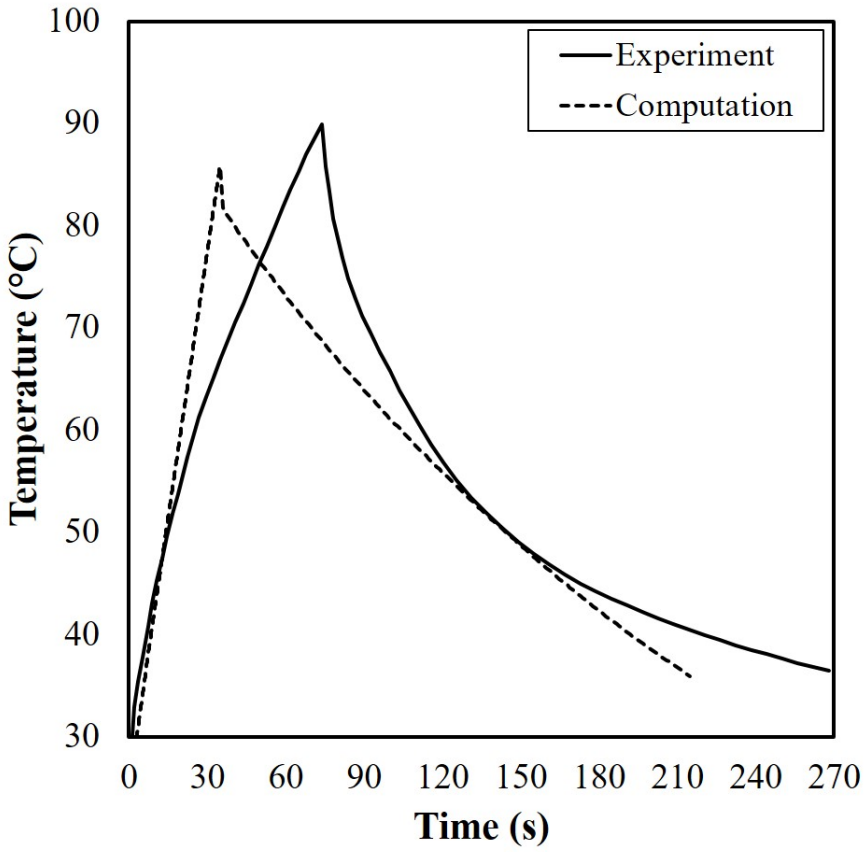

Figure 3.4: Comparison of actuation cycles for experimental SMA-liquid metal composite actuator and computational model with less aggressive liquid metal flow rates (1ml/min).

Table 3.1: Comparison of actuation frequencies observed in other large monolithic SMA actuators.

Study	Heating	Cooling	Actuator	Act. Wt. [g]	Freq. [Hz]
Hartl et al. [23]	Induct.	Forced Liq. Metal Conv.	NiTi Beam	72.3	0.0037
Mabe et al. [18]	Induct.	Forced Air Conv.	NiTi Torque Tube	105	0.0017
Mabe et al. [74]	Conduct.	Forced Air Conv.	60-NiTinol Beam	180	0.0014
Saunders et al. [19]	Induct.	Forced Air Conv.	NiTiHf Torque tube	149	0.0200

3.2 The Surface Roughness and Its Mitigation of Laser Powder-Bed Fusion Additive Manufacturing of Internal Channels

Now that a liquid metal SMA actuator has been demonstrated, one can further increase the cooling rates by embedding the liquid metal channels fully into the interior of the SMA, which

require L-PBF to manufacture. The results of the roughness of these channels are investigated in relation to printing parameters and its mitigation via electropolishing are presented herein.

3.2.1 General Trends

A representation of the root-mean-square surface roughness, S_q, profile skewness, S_{sk}, and profile kurtosis, S_{ku}, from optical profilometry are depicted in Fig. 3.5. As-fabricated S_q values range between 30-$100\,\mu\mathrm{m}$ which are orders of magnitude higher than the typical S_q values associated with machined metallic parts (0.5-$5\,\mu\mathrm{m}$ [75]), and also several times higher than the S_q values of the top flat exposed surfaces of additively manufactured parts ($10\,\mu\mathrm{m}$ [42]). Though these S_q values are relatively high, it can even be argued that the values should be even higher as these channels were sectioned open and sonicated in an alcohol bath which can remove loose powder more easily than a removing powder from long unopened high aspect ratio channel. Between channel diameters, no significant trend is observed in regards to the overall S_q values. These S_q values are analyzed in more detail later in the manuscript.

The mean of as-fabricated S_{sk} values across all channels is slightly negative, indicating a slight bias towards troughs on the surface. When the mean is taken across horizontal and vertical channels separately, there is a clear distinction between horizontal channels tending to be dominated by troughs and vertical channels tending to be dominated by peaks. The as-fabricated kurtosis values, S_{ku}, have nominal values of approximately 3, implying that Gaussian distributed surfaces are present.

After electropolishing, we observe a reduction in S_q values that diminish in intensity to a varying degree. This degree follows a trend following laser energy density which is later discussed. However, it is generally evident that electropolishing is an effective post-process procedure for the reduction in S_q. Furthermore, after electropolishing, S_{sk} indicates a bias for peaks for 2 mm and 1.5 mm channels and a bias for troughs for 1 mm channels, generally regardless of channel orientation; S_{ku} seems not to be affected and remains at a nominal value of 3. Since the S_{ku} value implies a Gaussian distributed surface for both the as-fabricated and electropolished channels, no further analysis of S_{ku} is performed.

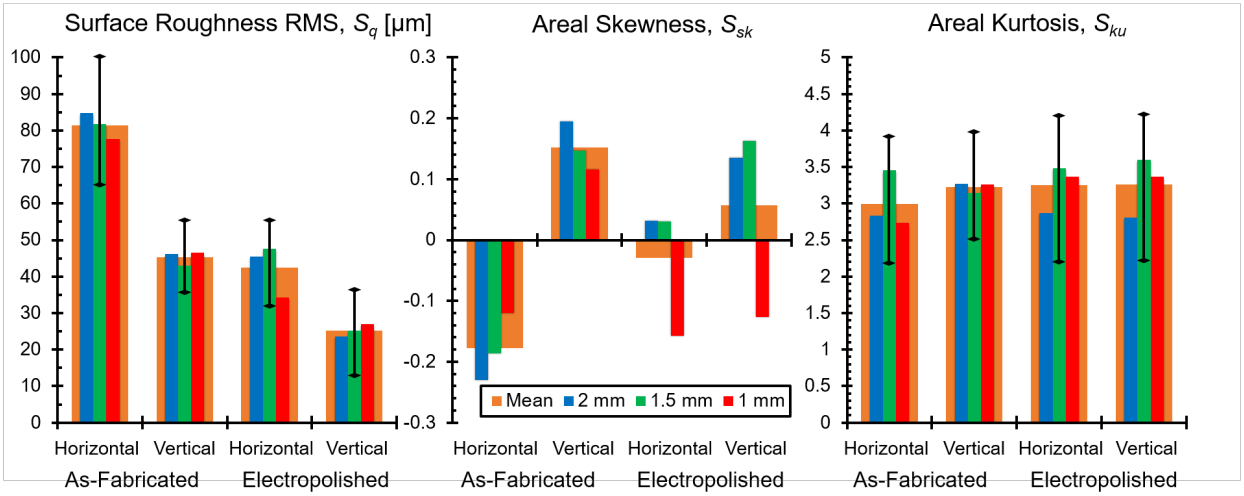

Figure 3.5: Experimental results displaying the group S_q, S_{sk}, and S_{ku} of as-fabricated and electropolished channels. The mean includes all channels regardless of channel diameter. Error bars depict the standard deviation for the mean.

Fig. 3.6 displays a representative SEM micrograph of the four major scenarios of the forty-eight channels before and after electropolishing: horizontal as-fabricated (top left), vertical as-fabricated (bottom left), horizontal electropolished (top right), and vertical electropolished (bottom right). Significant improvement in surface roughness after electropolishing can be observed. The horizontal channel surfaces originally contained stalactites covered in powder feedstock; after electropolishing, these features were almost completely removed, leaving behind thin bridge-like features and some circular topology. The vertical as-fabricated surfaces were originally speckled with partially fused precursor powder, which subsequently yielded a visibly smooth surface with sporadically positioned particles-like features remaining after the electropolish. It is believed that the circular and particle-like features in the electropolished channels are not powder feedstock on the surface but the remnant edges of interfaces of separate penetrating melt pools and partially fused particle interfaces, respectively.

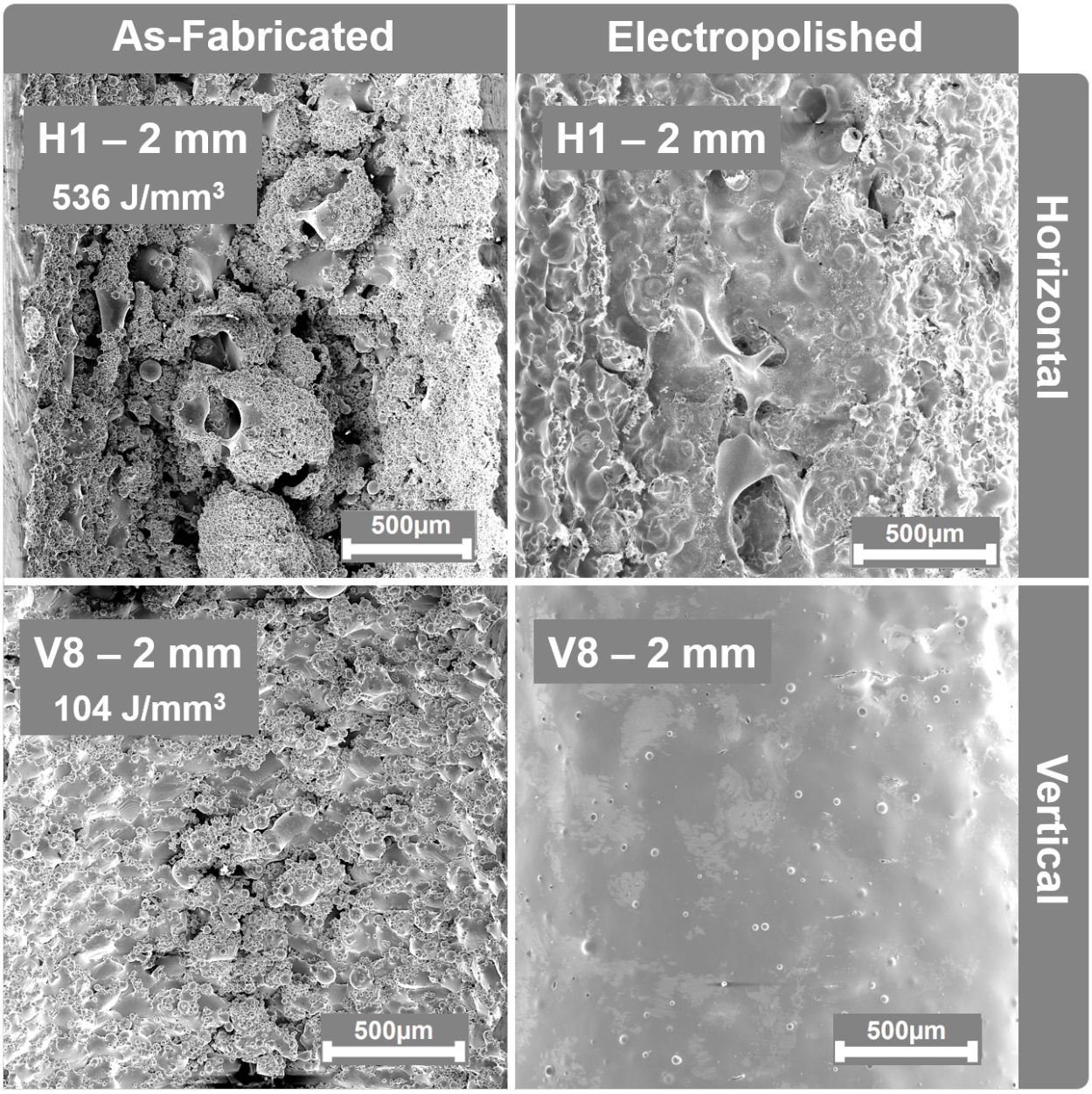

Figure 3.6: SEM micrographs displaying representative interior channel morphology before and after electropolishing of horizontal and vertical channels. The fused feedstock powder on the as-fabricated surfaces found in both horizontal and vertical channels was effectively removed, thereby decreasing surface roughness significantly. However, horizontal channels contained some larger features from the remains of their stalactites.

3.2.2 As-Fabricated Channel Analysis

A more detailed representative group of SEM micrographs of the as-fabricated channels decreasing in channel diameter is presented in Fig. 3.7, with the top and bottom rows representing horizontal and vertical channels, respectively. Micrographs further detail that the surfaces of vertical channels are speckled with partially fused precursor powder while the horizontal channels contain a similar appearance but with additional large stalactites.

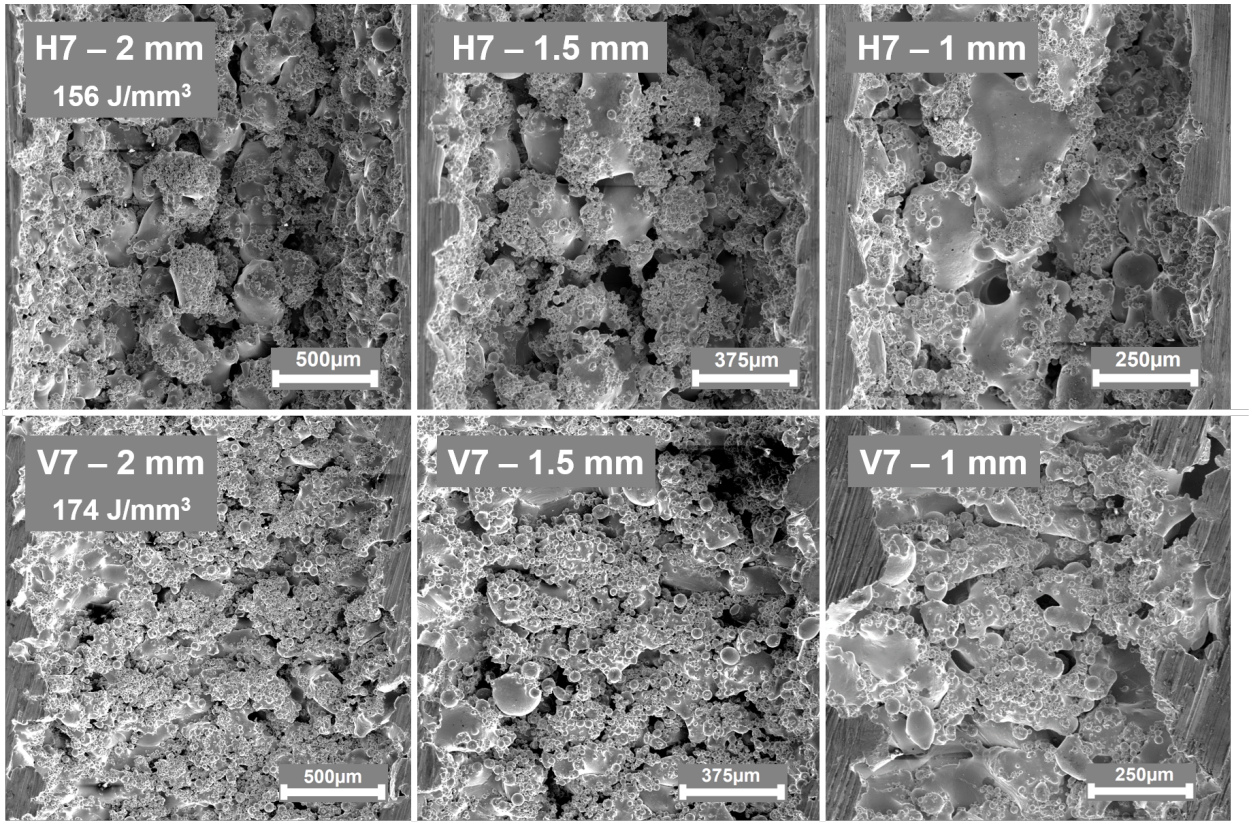

Figure 3.7: Representative SEM micrographs of the as-fabricated channel ceiling for the horizontal channels (top three images) and the as-fabricated channel walls of the vertical channels (bottom three images) over the three channel diameters. The stalactite structures on the ceilings of the horizontal channels are a prominent feature and increase surface roughness. The vertical channels are more uniform with NiTi powder partially fused to the surface.

When comparing laser energy density to surface roughness, qualitatively, the SEM micrographs

indicate an obvious pattern versus surface topology, as highlighted in Fig. 3.8. The higher energy density channels seem to be covered more uniformly and denser in powder than lower energy density channels. Specifically in the horizontal channels, the size of the stalactites are much larger at higher energy densities. In vertical channels, the underlying surface where the melt solidified for each layer is more easily observed as energy density decreases; notice the increase of the underlying melt surface from V5 to V8 (including V7 from Fig. 3.7) as energy density decreases. The underlying surface is less noticeable in the horizontal channels as the stalactites are the main feature. These trends stem from increased energy density leading to larger melt pools; larger melt pools result in more melt runoff into the powder feedstock in horizontal channels creating larger stalactites and/or more melt fusing to more powder feedstock. This observation is also seen in 1.5 mm and 1 mm channels not shown in Fig. 3.8. However, quantitatively, there is no trend with regards to energy density against surface roughness of either the vertical or horizontal top surfaces. It is possible that there is still enough powder on the lower energy density channels to increase the roughness to an equivalent degree like that of the higher energy density channels, which is further supported by the surface roughness values that are on the order of magnitude of the powder feedstock.

S_q and S_{sk} surface roughness data from optical profilometry was processed to produce p-values from ANOVA shown in Table 3.2. The p-values help clarify which process parameters are significant for determining as-fabricated S_q and S_{sk}. A p-value of less than 0.05 is considered significant with 95% confidence, therefore it is clear that channel orientation has the most significant effect on S_q. Scan pattern and channel orientation play an important role in determining S_{sk} compared to other factors, even though they are not as statistically significant.

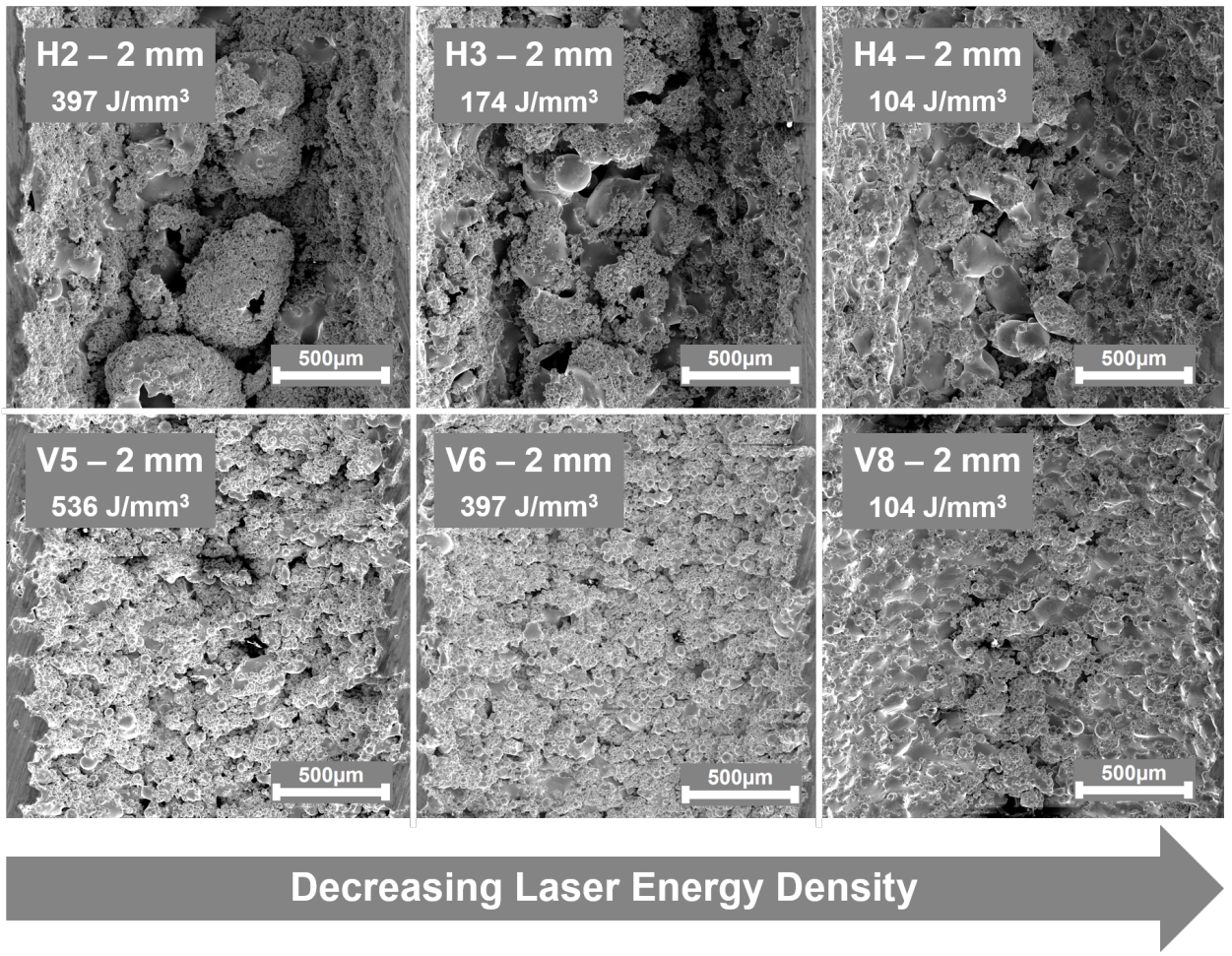

Figure 3.8: SEM micrographs displaying representative as-fabricated interior channel morphology in with respect to energy density. The top images consist of the horizontal channels, while the bottom images consist of the vertical channels. As energy density decreases there is an increase in areas of smooth surfaces rather than powder adhered to the surface.

Table 3.2: p-values from ANOVA of as-fabricated channels; bold-face denotes significance

		Process Parameter				
	Channel Diameter	Laser Power	Scan Speed	Hatch Space	Scan Pattern	Channel Orient.
S_q	2 mm	0.0909	0.0859	0.3313	0.5566	**0.0002**
	1.5 mm	0.5083	0.2792	0.4280	0.4309	**0.0002**
	1 mm	0.8381	0.7806	0.6255	0.3766	**0.0062**
S_{sk}	2 mm	0.3910	0.3826	0.5348	0.3175	0.0816
	1.5 mm	0.7180	0.8280	0.5070	0.1170	0.2330
	1 mm	0.9189	0.3678	0.7056	**0.0313**	0.3072

The main effects plots of Fig. 3.9 support the ANOVA results as demonstrated by the high slopes associated with channel orientation for S_q, in addition to scan pattern and channel orientation for S_{sk}. Comparing horizontal channels against vertical channels, S_q values of the horizontal channels are nearly twice that of the S_q values of the vertical channels. The remaining parameters clearly are overshadowed by the influence of channel orientation for S_q, thus, it can confidently be stated that channel orientation plays the single most contributing parameter to the resultant S_q.

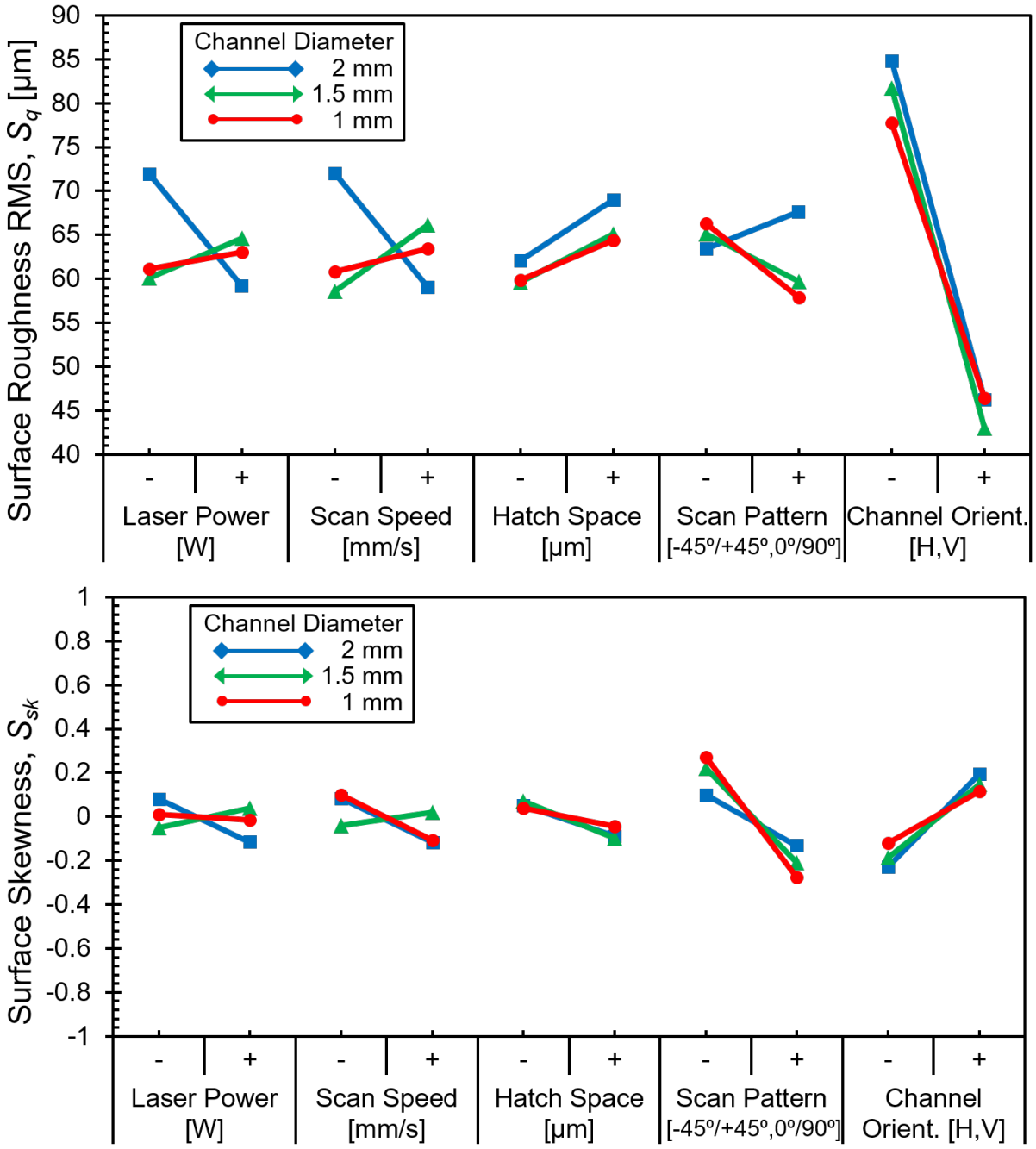

Figure 3.9: Main effects plots for as-fabricated channels display the variation of S_q and S_{sk} with each factor. Channel orientation dominates the resultant S_q while S_{sk} is most affected by scan pattern.

The significant effect of channel orientation on surface roughness is consistent with expectations, as discussed previously. Channel orientation is an important design consideration in AM. It

is not uncommon to encounter a situation where flexibility in setting a specific channel orientation is not feasible. For example, a part that has a complex vascular design of channels will inevitably include some channels fabricated in the horizontal orientation, or the layout of support structures in the part may necessitate building in a specific orientation. Therefore, when producing horizontally oriented channels it is important to take into account that the channel ceiling surface will inevitably have high roughness, seemingly regardless of other process parameters.

3.2.3 Electropolished Channel Analysis

Electropolishing was performed as a post-processing step to improve surface roughness. An initial experiment was first conducted, however, to quantify the mass loss of small features on as-fabricated surfaces. After 25 min of electropolishing, all pillars lost approximately 0.25 mm of material circumferentially. Thus, a consistent mass loss rate of approximately 0.01 mm/min occurred, regardless of process parameters used. It is important to point out that this does not necessarily suggest each channel has the same decrease in surface roughness due to electropolishing. Ultimately, this procedure would result in a 1.5 mm diameter channel losing enough material to become a 2 mm diameter channel, an important consideration when designing channels or similarly sized features (assuming uniform electropolishing for high aspect ratio channels).

As discussed before in Section 3.2, it was observed qualitatively that there was some trend in the as-fabricated surface topology with respect to energy density. It was suggested that this trend came from higher energy densities producing more melt runoff which could create larger stalactites and/or partially fuse more raw powder that was located in the channel. Electropolishing seems to also exhibit this trend both qualitatively and quantitatively regarding laser energy density against S_q values. Quantitatively, laser energy density in L-PBF is a metric that combines laser power (p), scan speed (v), and hatch space (h), and thickness (t) through the following relationship:

$$\text{Energy Density} = \frac{p}{vht} \tag{3.1}$$

For both horizontal and vertical channels, an inverse correlation is observed between the effi-

cacy of electropolishing on reducing surface roughness and laser energy density [J/mm^3], represented by the reduction in surface roughness between as-fabricated and electropolished channels, as presented in Fig. 3.10.

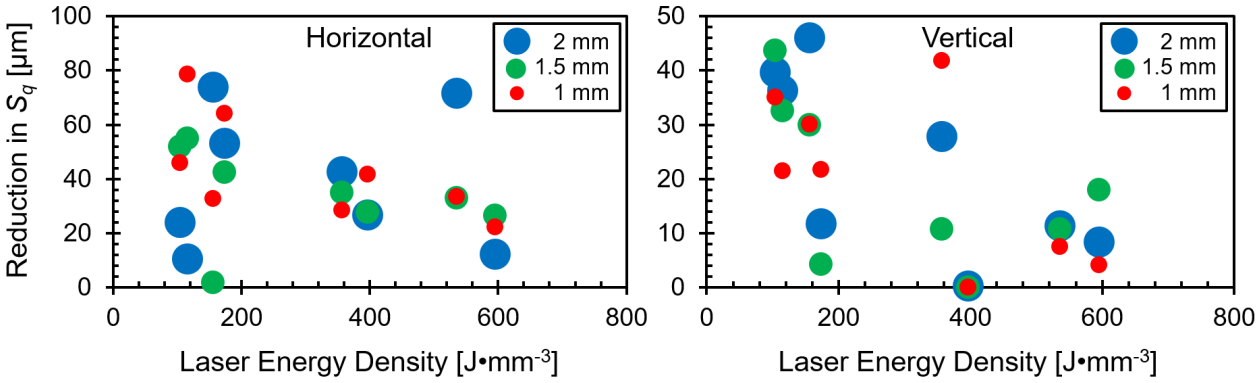

Figure 3.10: As energy density during fabrication decreases the efficacy of electropolishing increases as quantitatively displayed for horizontal and vertical channels.

Through SEM micrographs in Fig. 3.11 for both horizontal channels and vertical channel, H2 clearly has more features on its surface including the edge remnants of fused powder boundaries. H2 was produced with an energy density of 397 J/mm^3; H3 was produced with 174 J/mm^3 and visibly displays a lower density of surface features; this trend of decreasing surface features is further iterated in H4 with an energy density of 104 J/mm^3. For the vertical channels, V6 presents noticeable surface features while decreasing the energy density leads to a surface with only a few remaining particle boundaries in V8. From optical profilometry, V6 has over three times the S_q value than V8. This effect also observed for the other channel diameters not shown in Fig. 3.11.

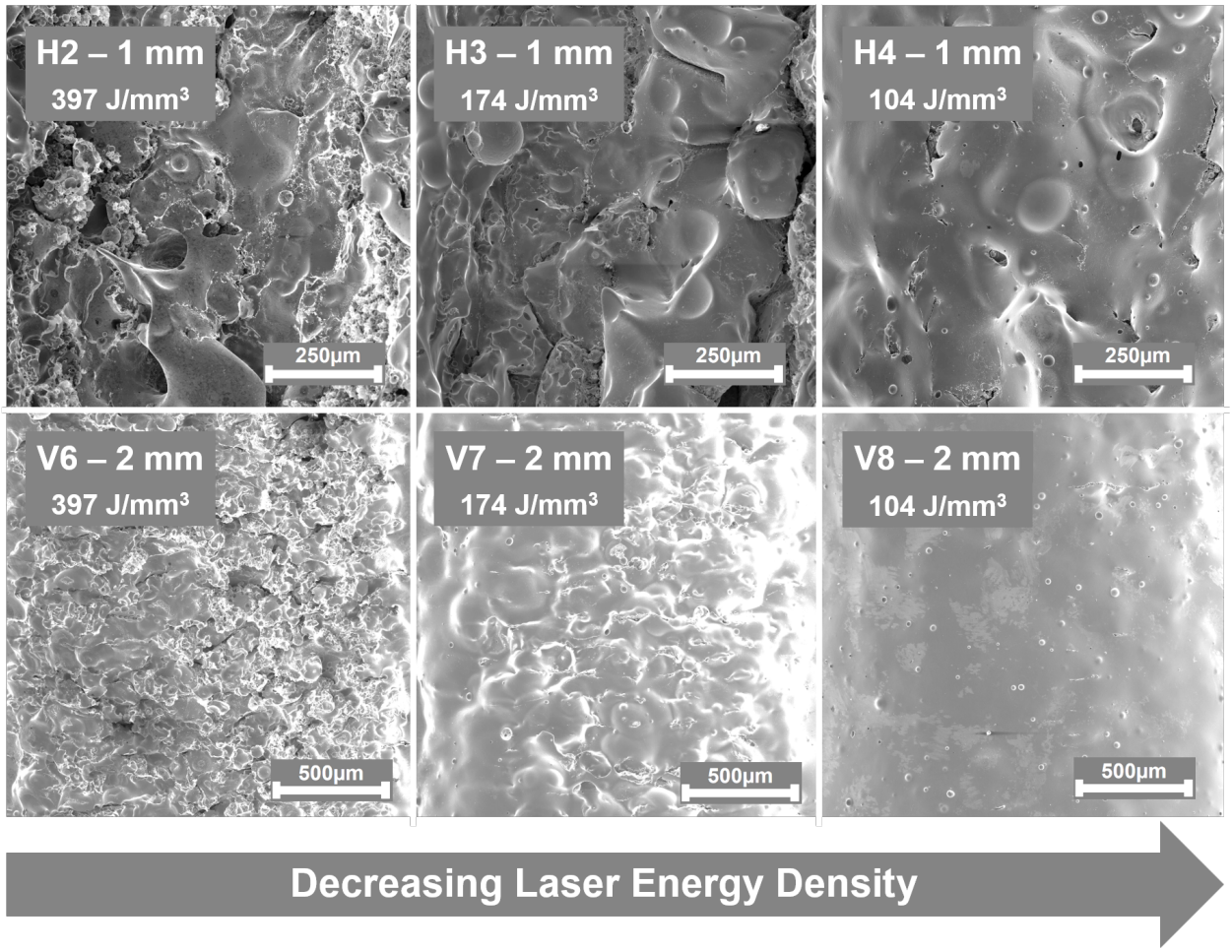

Figure 3.11: SEM micrographs of electropolished horizontal (upper) and vertical (lower channels) indicate that as laser energy density decreases the effectiveness of electropolishing increases, ultimately resulting in lower surface roughness for electropolished lower energy density surfaces.

With the additional step of electropolishing, the more penetrating melt pools and partially fused particle interfaces powder effectively results in a less effective electropolish as there is a higher density of some edge remnants in the higher energy density channels. A lower energy density would lead to less melt pool runoff into supporting powder and less partial fusion with powder. When ordered by energy density there is a evident trend that is even agnostic to channel orientation which can be seen in Fig. 3.11 and even seen on 3.6. The energy density of H1 is 536 J/mm^3 while V8 is 104 J/mm^3. Thus, it is emphasized that using the lower energy density parameter sets that still provide appropriate melting can provide a more facile route to reduce

channel surface roughness via electropolishing.

Captured by the ANOVA p-value results and main effects plots in Table 3.3 and Fig. 3.12, there appears to be multiple significant parameters in determining electropolished S_q, unlike the as-fabricated channels. For S_q, channel orientation remains the most significant parameter for 2 mm and 1.5 mm channels; however, laser power and scan pattern are also significant for 2 mm channels and hatch space is significant for 1 mm channels. It is observed that as channel diameter decreases from 2 mm to 1 mm, laser power, scan pattern, and channel orientation become less important in determining S_q and hatch space becomes more significant as the low level hatch space of $35\,\mu\mathrm{m}$ leads to higher roughness. This effect could be due to lower hatch space resulting in an increased amount of melt overlap interactions between laser scans rather than high hatch space which, contrarily, contains an increased amount of wide solidified melt surfaces. This effect could have been obscured in the as-fabricated channels due to the fused surface powder.

Table 3.3: p-values from ANOVA of electropolished channels; bold-face denotes significance

		Process Parameter				
	Channel Diameter	Laser Power	Scan Speed	Hatch Space	Scan Pattern	Channel Orient.
S_q	2 mm	**0.0400**	0.5030	0.2521	**0.0031**	**0.0003**
	1.5 mm	0.2921	0.5714	0.3694	0.4659	**0.0134**
	1 mm	0.5530	0.1954	**0.0076**	0.9020	0.1348
S_{sk}	2 mm	0.2230	0.1760	0.7670	0.7020	0.3020
	1.5 mm	0.1039	0.0644	0.1915	**0.0251**	0.5989
	1 mm	0.8245	0.2211	0.3794	**0.0032**	0.5393

For S_{sk}, the tendency of channels to be dominated by troughs or peaks is dependent on scan pattern; the -45°/+45° pattern leads to peaks while the 0°/90° leads to troughs. The main effects plots indicate that for other factors excluding scan pattern, 2 mm and 1.5 mm channels remain generally dominated by peaks or neutral while 1 mm channels remain strictly dominated by troughs

after electropolishing.

Ultimately, the act of electropolishing results in the ability to mitigate S_q by decisively altering L-PBF process parameters for electropolished channels rather than being confined by a design constraint (i.e., channel orientation), as was the case in the as-fabricated channels.

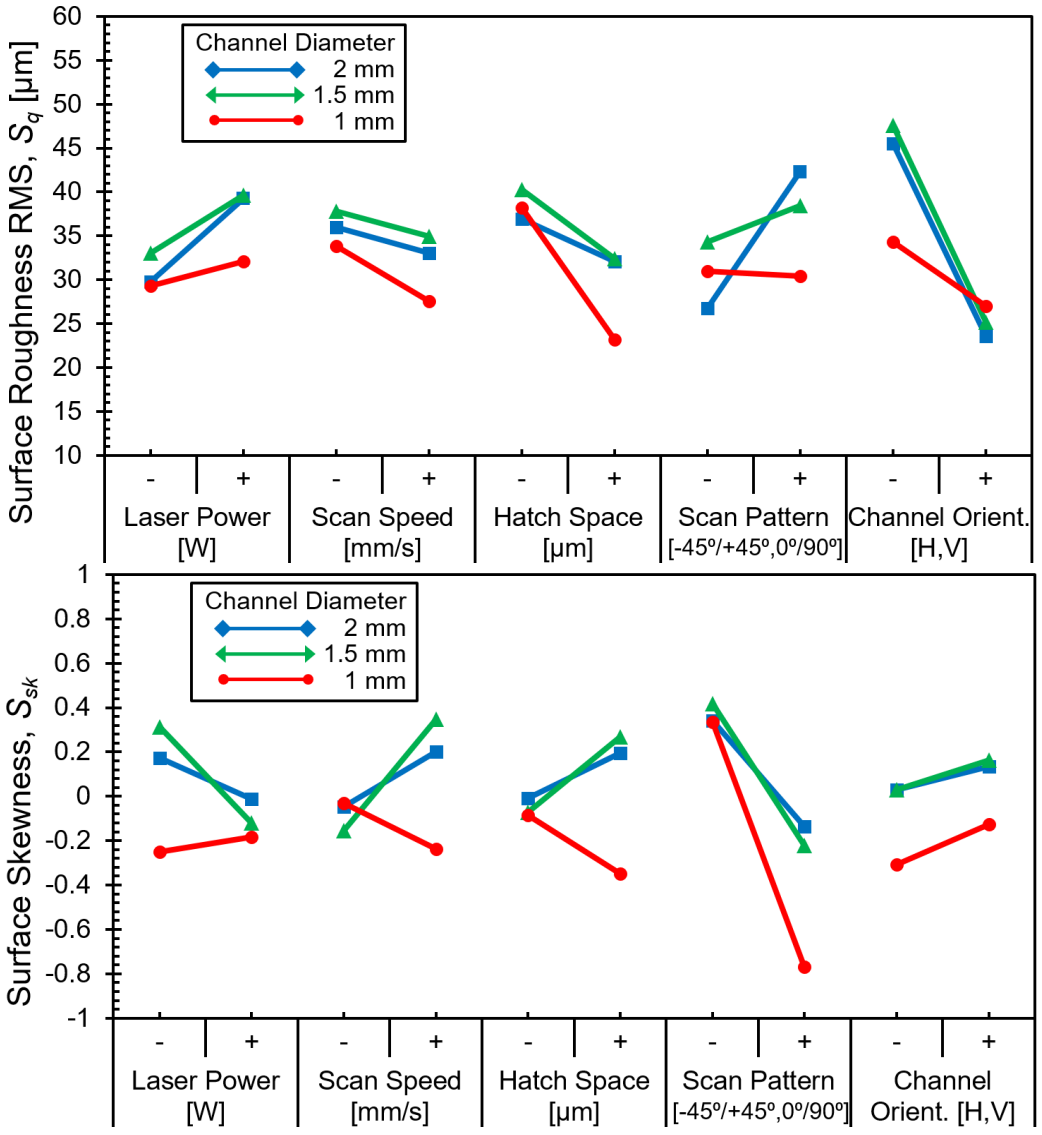

Figure 3.12: The main effects plots for electropolished channels display the variation of S_q and S_{sk} with each factor. Channel orientation again dominates the resulting S_q for 2 mm and 1.5 mm channels; as channel diameter decreases, channel orientation becomes less dominant and hatch space becomes the most dominant. S_{sk} is most affected by scan pattern for 1.5 mm and 1 mm channels.

3.3 Gallium-Based Liquid Metal-Induced Corrosion of Nickel-Titanium Alloys, Its Constituents, and Copper

This section presents the result of gallium-based liquid metal interactions on SMA and related metals. This enables modifications of a liquid metal SMA where in some application liquid metal would be in direct contact with the SMA rather than isolated electrically by a polymer coating, as in the liquid metal SMA presented in Section 3.1. Further, copper is in direct contact with previously mentioned setup which is why it was included in this study.

3.3.1 Liquid Metal-Induced Interactions on Elemental Ni and Ti

3.3.1.1 200 Nickel

Ni reacted significantly with each liquid metal composition at the tested temperature of 220°C. After the cleaning treatment, dark gray solid reaction products remained protruding from the Ni surface. A comparison of the liquid metal interactions of the Ni/Ga couples over the time exposed to liquid metal is plotted against their mass gain and reaction layer thickness in Fig. 3.13. As exposure to the liquid gallium increased, both the weight and reaction layer thickness increased, indicating that alloying is the dominant corrosion mechanism for these couples. Further, the total cross-sectional dimensions increase over time compared to their initial values.

SEM imaging shows the reaction layer as not a single monolithic formation, but rather a dense collection of tetragonal crystals oriented normal to the Ni surface. In many diffusion experiments, thin needle-like crystals are formed in the case where only grain-boundary diffusion takes place due to low temperatures, rather than volume diffusion which occurs at higher temperatures [76]. Highlighted in Fig. 3.14, each Ni couple had similar cross-sectional morphologies having: significantly rounded corners on the bulk remaining Ni, curled reaction layers on the corners, and concave reaction layers on each side. This morphology is similar to but distinctly different from that of the Ni/Ga couple at 400°C discussed in [60]; that morphology had sharp corners in the bulk Ni, and thick flat reaction layers on each of the sides.

EDS data suggests that the reaction layer is comprised of concentrations ranging from 70 80

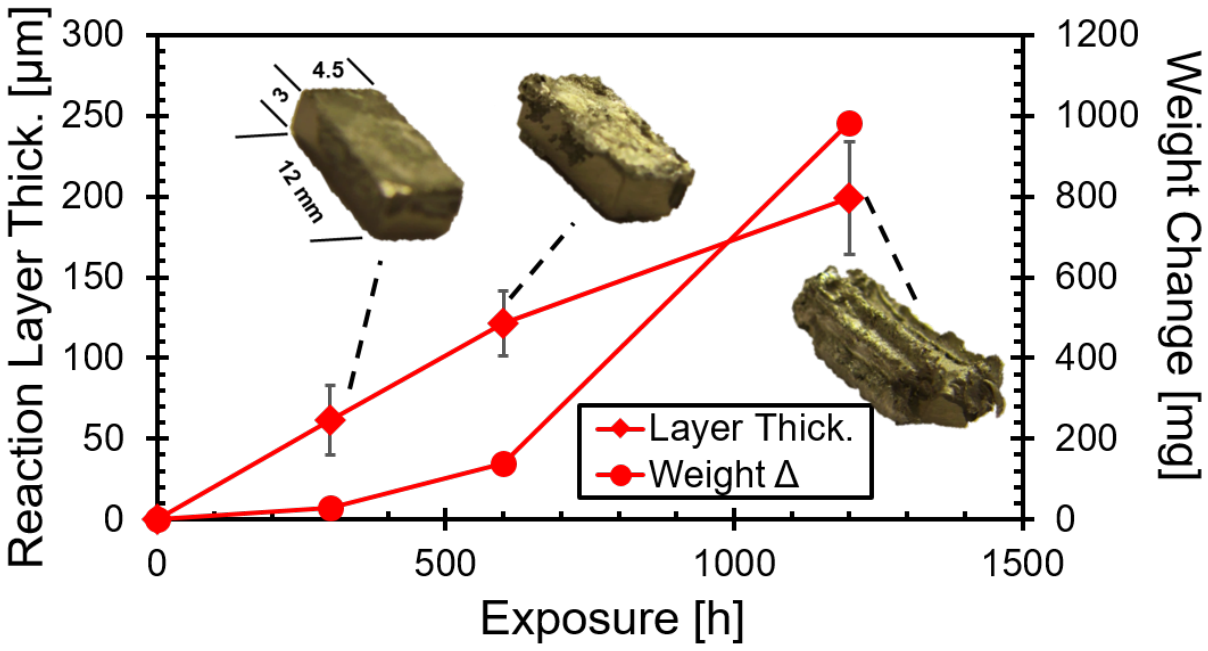

Figure 3.13: Weight change and reaction layer growth during liquid metal exposure for the Ni/Ga couples. Images of the Ni specimens are overlayed. Nickel undergoes alloying immediately with a steady weight increase and increase in reaction layer thickness.

at.% Ga, as depicted in Fig. 3.15. In the bulk Ni near the reaction-layer interface, there is no Ga detected in the Ni matrix, which was compared to that virgin Ni. XRD indicated that the reaction layer consists of crystal structures relating to Ni_2Ga_3, Ni_3Ga_7, and crystalline Ga.

Ultimately, these observations suggest that alloying is the dominant mechanism of liquid metal-induced corrosion for Ni at 220°C as supported by a positive mass growth rate, increasing cross-sectional dimensions, and confirmed increasing intermetallic growth.

3.3.1.2 Titanium Grade 2

After cleaning, silver hues were observed which indicated liquid metal wetting, but no solid surface products were detected. The remaining surfaces had a golden hue, i.e., oxidized titanium, unique to the fact that Ti floated on the liquid metal surface and exposed to air. SEM imaging shows sharp corners and no reaction layers. Edge roughness measurements, could indicate that liquid metal had dissolved material from the Ti surface; however, no change in roughness was

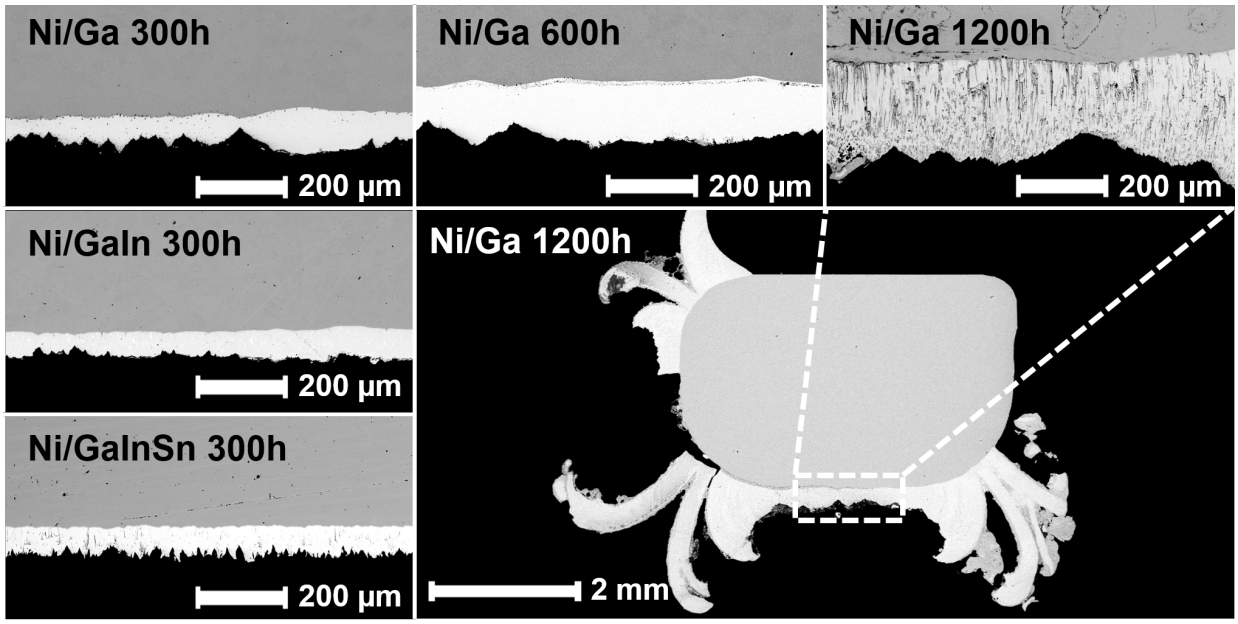

Figure 3.14: BSE imaging of Ni couple cross-sections. The upper section of each image is the bulk Ni. The lighter layer consists of Ni/Ga intermetallics. The reaction layer thickness increases with exposure time. For each specimen, the corners reacted faster than the sides which was especially emphasized for the 1200h specimen which the alloying growth began to curl.

measured, corresponding to a lack of measured weight change. Further, EDS measurements do not indicate Ga, In, or Sn diffusion into the Ti matrix. These observations suggest there is no corrosion with Ti at 220°C.

3.3.2 Liquid Metal-Induced Interactions on NiTi Systems: Isothermal Exposure and Thermal Cycling

The equiatomic $Ni_{50}Ti_{50}$, $Ni_{55}Ti_{45}$, $Ni_{49}Ti_{36}Hf_{15}$, and thermally cycled $Ni_{50}Ti_{50}$ couples each displayed silver hues where liquid metal wetting was present, similar to the Ti couples, but again lacked any indication of solid surface products.

SEM again shows sharp corners and a lack of reaction layers. Cross-sectional dimensions remained constant. Edge roughness measurements, based on Fig. 3.17, show no change, compatible with the lack of any measurable weight change (see Fig. 3.18). EDS measurements do not indicate Ga, In, or Sn diffusion into any NiTi SMA systems tested, highlighted in Fig. 3.19.

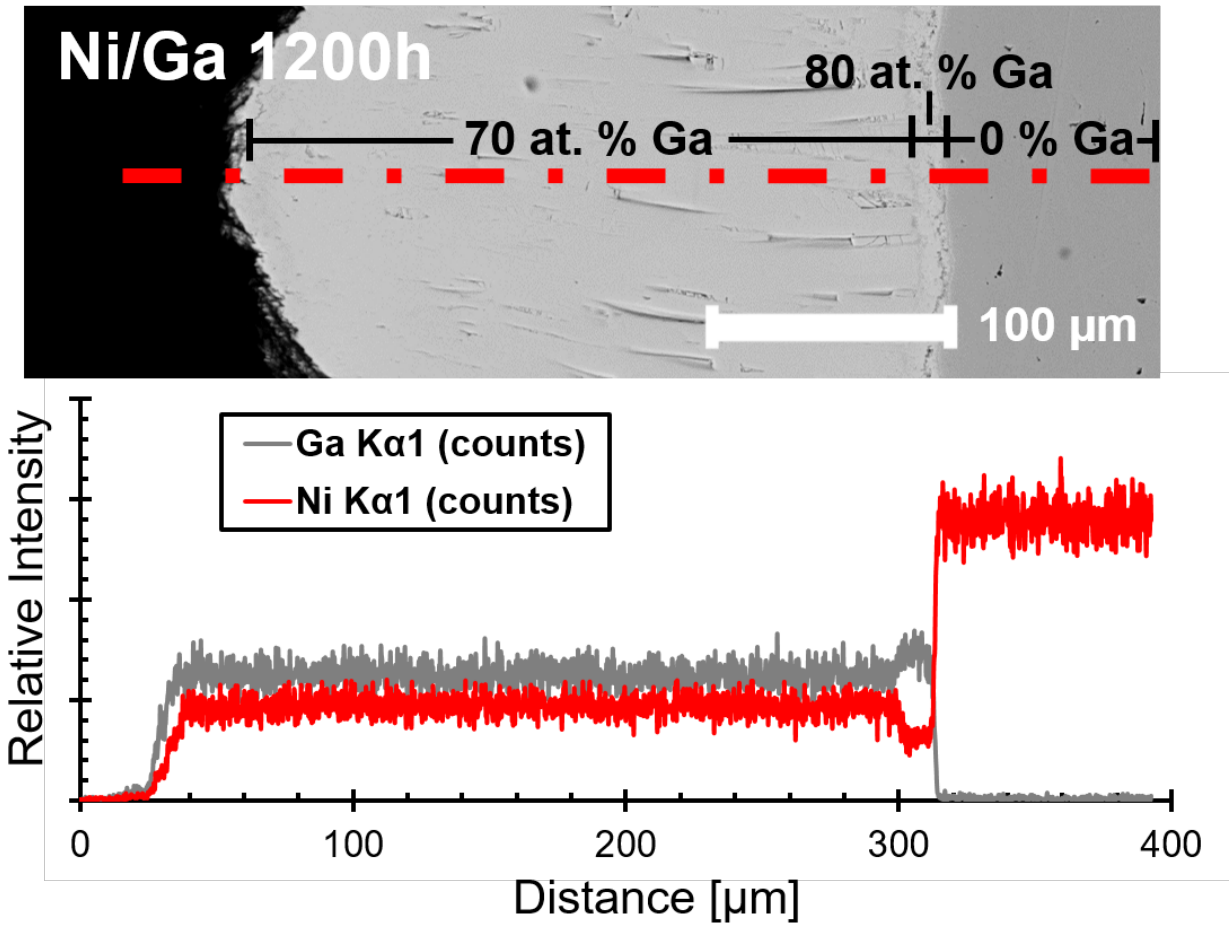

Figure 3.15: EDS linescan of the Ni/Ga couple reaction layer. In almost all cases, the Ni/Ga reaction layer consisted of 70 at. % Ga, however there was contrarily an increase in Ga content to 80 at. % near the bulk Ni interface for the 1200 h specimen.

The $Ni_{50}Ti_{50}$/E-GaIn couples exposed to up to 270 cycles of thermally induced martensitic transformation, did show an increase in edge roughness from an initial value of <1 µm to 3.5 µm; however, this could be attributed to transformation-induced surface defects as weight did not show any significant change.

3.3.3 High-Temperature Liquid Metal-Induced Interactions on Ti and NiTi

High temperature experiments were performed with Ti and $Ni_{55}Ti_{45}$ specimens exposed to E-GaIn at 300°C, 400°C, 600°C, 800°C, and 950°C for only 3 h with a sufficient amount of liquid metal to prevent saturation. Important cross-sections are displayed in Figs. 3.20 and 3.21. It is

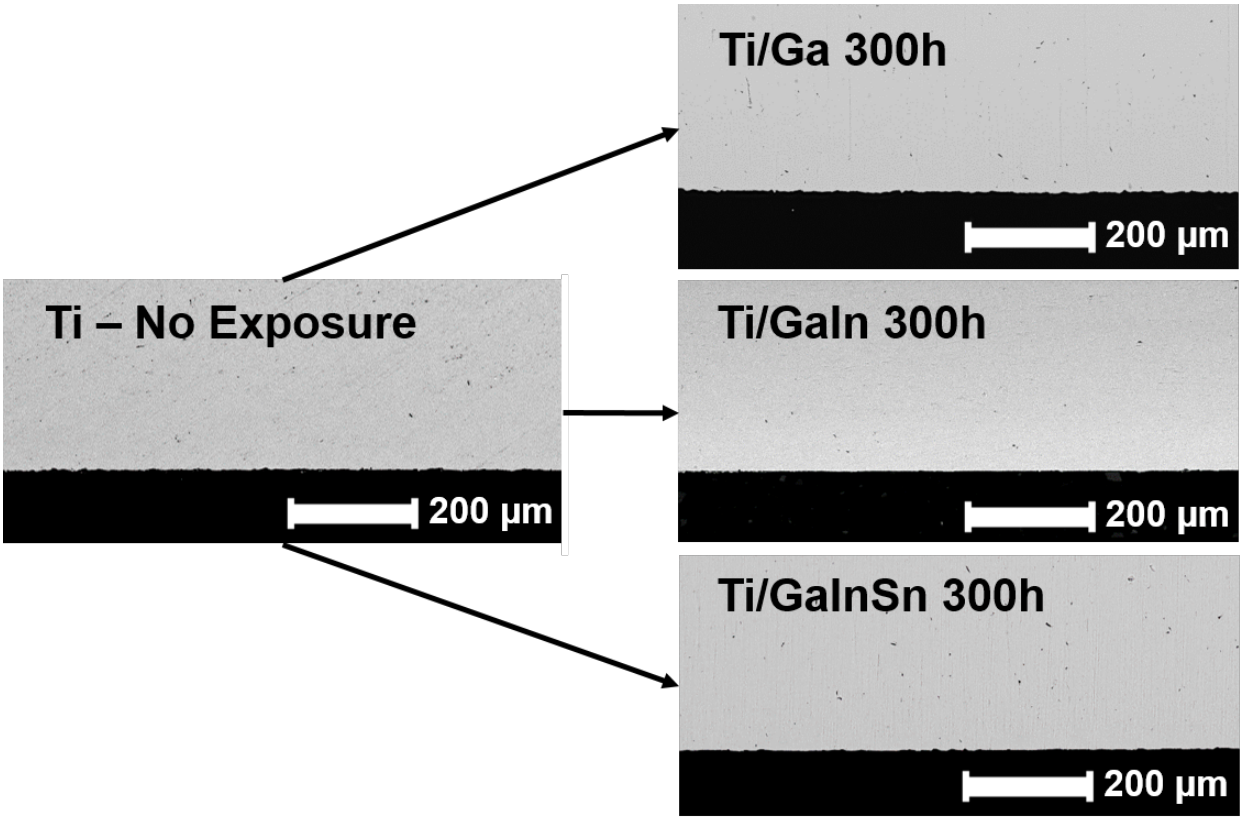

Figure 3.16: BSE imaging of Ti couple cross-sections after liquid metal exposure. Liquid metal interaction of any kind is not detected.

noted that the bottom edges of these figures correspond to the face in contact with the bottom of the crucible, and thus do not represent the overall corrosion behavior.

The 300°C Ti couple did not show any signs corrosion exactly like its 220°C counterpart, while the 400°C Ti couple had a very small mass increase of $<$1 mg and an extremely small and disconnected reaction layer (5 µm thick). The 600°C Ti couple (Fig. 3.20) had a mass increase of 30 mg (alloying) and its morphology resembled that of the type seen in the Ni couples (Fig. 3.14), i.e., rounded corners in the bulk, curled reaction layers on the corners. On the contrary, the 800°C Ti couple (Fig. 3.20) had a mass decrease of 50 mg (dissolution) with a more conformal reaction layer and with irregular areas of mass loss. The 950°C Ti couple *dissolved completely*. Generally, the reaction layer's were much more disordered than previous experiments tested at long exposures ($>$300 h), however, Ga content increased outwards and there were area that stoichiometrically

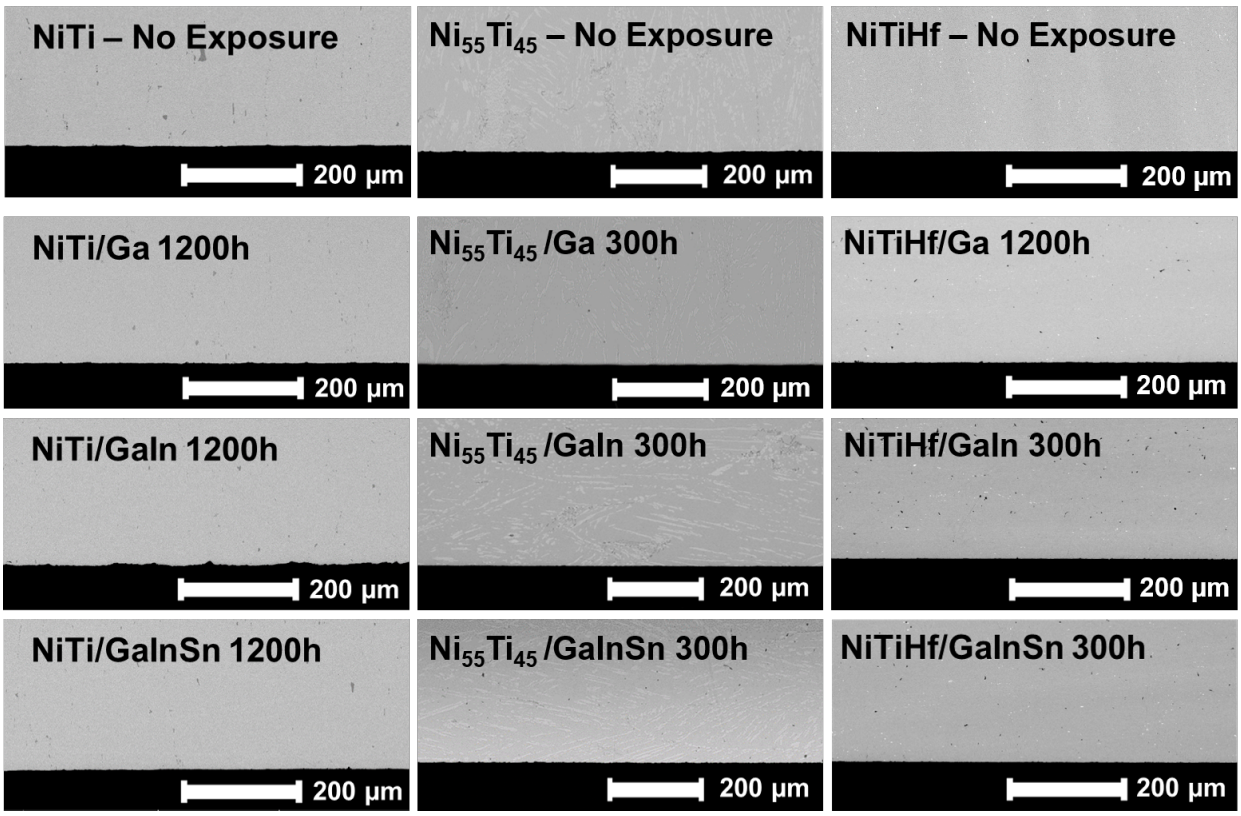

Figure 3.17: BSE imaging of SMA couple cross-sections. Liquid metal interaction is not detected. There is neither evidence of mass loss or etching, which could be occurring via Ni dissolution based on the Ni-Ga phase diagram (A.3)

$TiGa_2$ and $TiGa_3$. For the 600°C and 800°C, the bulk Ti adjacent to the reaction layer interface had about 5 at.% Ga, a contrasting result as this value was always within the EDS margin of error for the 220°C couples.

The 300°C NiTi couple did not show any diffusion or corrosion, matching the 300°C Ti couple. Further similarity to Ti was observed for the 400°C NiTi couple, which had an a very small mass increase of $>$1 mg and an extremely small and disconnected reaction layer (8 μm thick). However, at 600°C, similarities to Ti ended, as the 600°C NiTi couple (Fig. 3.21) had a mass decrease of 90 mg (dissolution) with a morphology that can be described as rounded corners in the bulk, thin reaction layers (15 μm) on each of the outer corners, and thicker reaction layers (60 μm) on the sides. The 800°C NiTi couple (Fig. 3.21) had a larger mass loss of 190 mg (dissolution) with a more conformal reaction layer but with irregular areas of mass loss, similar to that of the 800°C

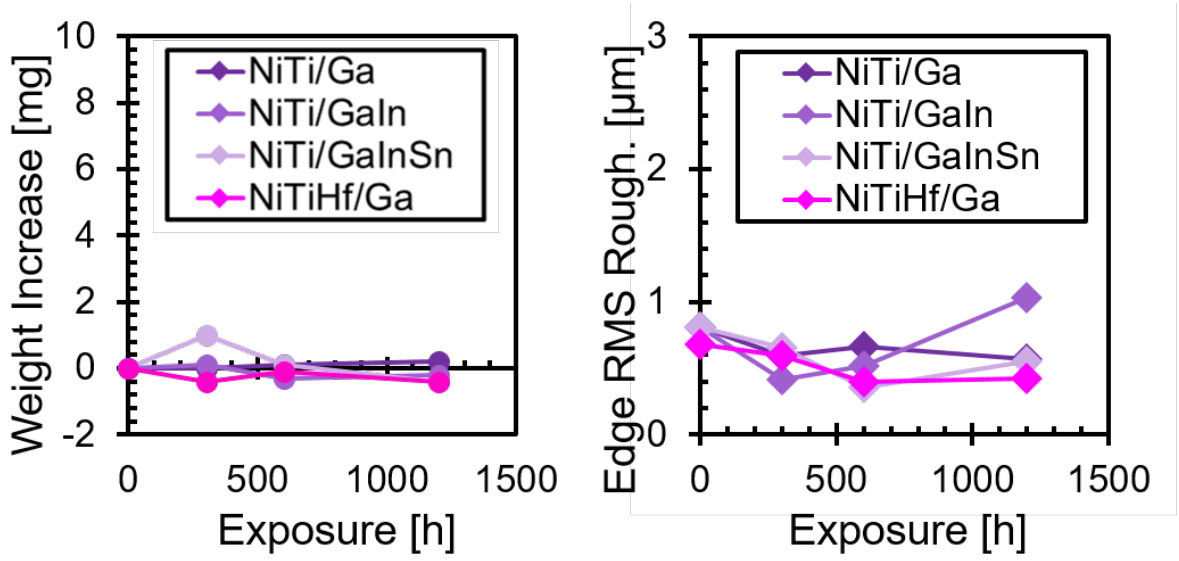

Figure 3.18: The weight change and edge RMS roughness of the various SMA corrosion couples. After exposure there no evidence of mass change and little evidence of the surface being attacked by the liquid metal based on the edge roughness.

Ti. The 950°C NiTi couple had an even larger mass decrease of 820 mg (dissolution) with a strictly conformal reaction layer. The chemistry of the all the observed reaction layers were again much more disordered due to the high temperature and short exposure; however, in the bulk NiTi adjacent to the reaction layer, there was about 5-7 at.% Ga replacing the Ni and Ti nearly equally. Line scans indicated that Ni decreased in intensity much more quickly that Ti towards the outer reaction layer, so much so that $TiGa_3$ in absence of Ni was detected on the outer edge of the 600°C reaction layer.

3.3.4 Liquid Metal-Induced Interactions on Electrical Grade Copper

Cu couples were seen to be coated with silver-gray solid surface reaction products after cleaning. The Cu couples are plotted in terms of mass gain over exposure in Fig. 3.22; both the Cu/Ga and Cu/E-GaIn couples seem to indicate that there may be dissolution present from 0 to 600 h, followed by significant mass growth (alloying) onwards. This contrasts the Cu/E-GaInSn couples which indicates only mass increase. (Note: the dotted line in the Cu/E-GaInSn line from 600 to 1200 h indicates an erroneousness result; solid reaction product fractured off and was lost during

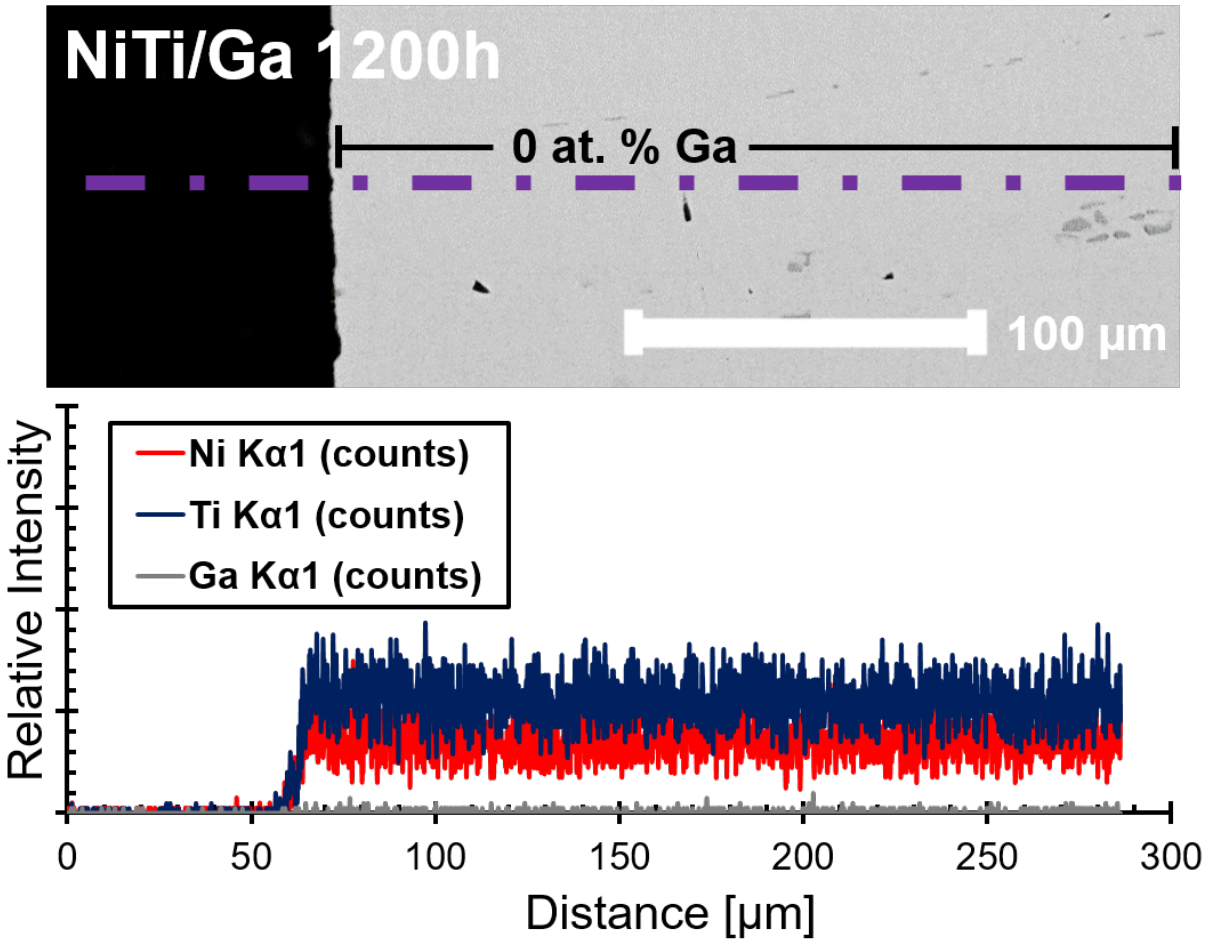

Figure 3.19: EDS linescan of $Ni_{50}Ti_{50}$/Ga couple reaction layer. Ga is not detected near the interface or in the bulk.

the cleaning process.) For the Cu/Ga and Cu/E-GaIn couples, it is possible that the liquid metal reached the Cu solubility limit and then began preferentially forming thick reaction layers. More evidence to support this is found by comparing the three liquid metal systems from 0 to 600 h; where the increased solute in Ga, i.e., In and Sn, seems to decrease the preference for dissolution. To further understand this dissolution preference, an additional Cu/E-GaIn specimen was exposed for 160 hours with 5x the amount of liquid metal than previous tests. This specimen resulted in high weight loss (1140 mg), thus indicating that dissolution would be dominant in Cu couples with sufficient amounts of liquid metal.

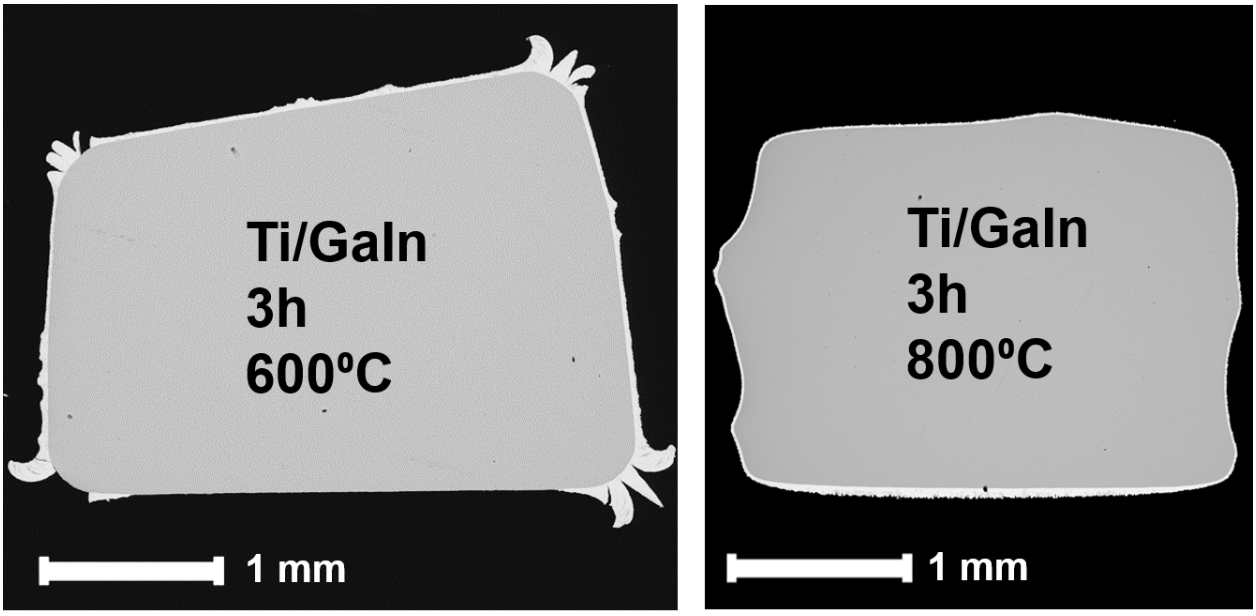

Figure 3.20: BSE imaging of the cross-sections of the Ti/E-GaIn couples at 600°C and 800°C. Only until some temperature between 400°C and 600°C does some type of corrosion occur to Ti. Note that this happens in just 3 hours, when nothing occurred previously at lower temperatures for at least 300 h.

SEM observation of the Cu specimens showed the reaction layers to be more homogeneous than that of the Ni couples. In diffusion experiments, an equiaxed layer occurs when volume diffusion occurs indicating that the copper is at relatively high temperature in terms of diffusion processes [76]. The thickness of the reaction layers, seen in Fig. 3.23, is compiled in Fig. 3.24 (along with the additional 160 h Cu/E-GaIn couple); there is some evidence that suggests the reaction layer reaches a equilibrium thickness for dissolution, as there is little change from 160 h to 600 h, until alloying after 600 h is preferred. However, it is emphasized that this transition is not intrinsic to Cu couples; the solubility limit and thus transition to alloying could be reached in less exposure with less liquid metal in the system. Thus, this would suggest that flowing a large amount of unsaturated liquid metal over a copper electrode would completely dissolve in a microfluidics application.

Along with SEM imaging, EDS suggests the reaction layer is multi-layered and corresponds to the products identified in the phase diagram of the Cu-Ga system [77]. For example, the 300

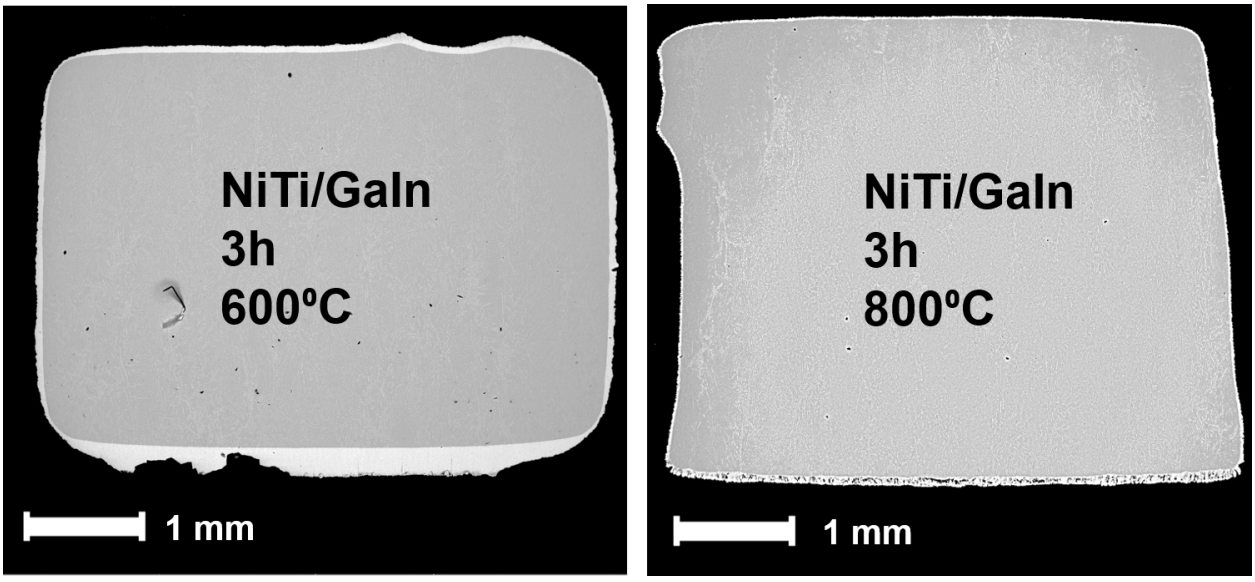

Figure 3.21: BSE imaging of the cross-sections of the NiTi/E-GaIn couples at 600°C and 800°C. Only until a temperature between 400°C and 600°C, does some type of corrosion occur for a NiTi specimen. Note that this happens in just 3 hours, when nothing occurred previously at lower temperatures for at least 300 h.

h Cu/Ga couple in Fig. 3.25 has an outer layer composed of 33 at.% Cu and 66 at.% Ga, likely the $CuGa_2$ θ intermetallic. The inner layer is 15 ± 5 μm thick with a composition of 60 at.% Cu and 40 at.% Ga, possibly the γ_3 phase. For the bulk Cu near the surface reaction, EDS indicated a chemistry of 99 at.% Cu, which is equivalent to that of unexposed Cu. For the couple containing In and Sn, similar observations were made for the outer layer, however the inner layer contained $<$5 at.% In and/or Sn. BSE imaging highlighted dark precipitates in the lighter matrix of the inner layer but EDS measurements could not resolve the chemical difference; the dark precipitates could be In-lean and/or Sn-lean areas, resulting in the darker BSE imaging. In the 1200 h exposures, pockets of nearly pure In-Sn mixtures were observed (white regions in Fig. 3.23).

All together, these observations suggest that dissolution is dominant when there is sufficient unsaturated liquid metal but alloying will occur when the liquid metal becomes saturated; further, In and Sn additions in Ga seem to decrease the preference for dissolution of Cu into the liquid metal.

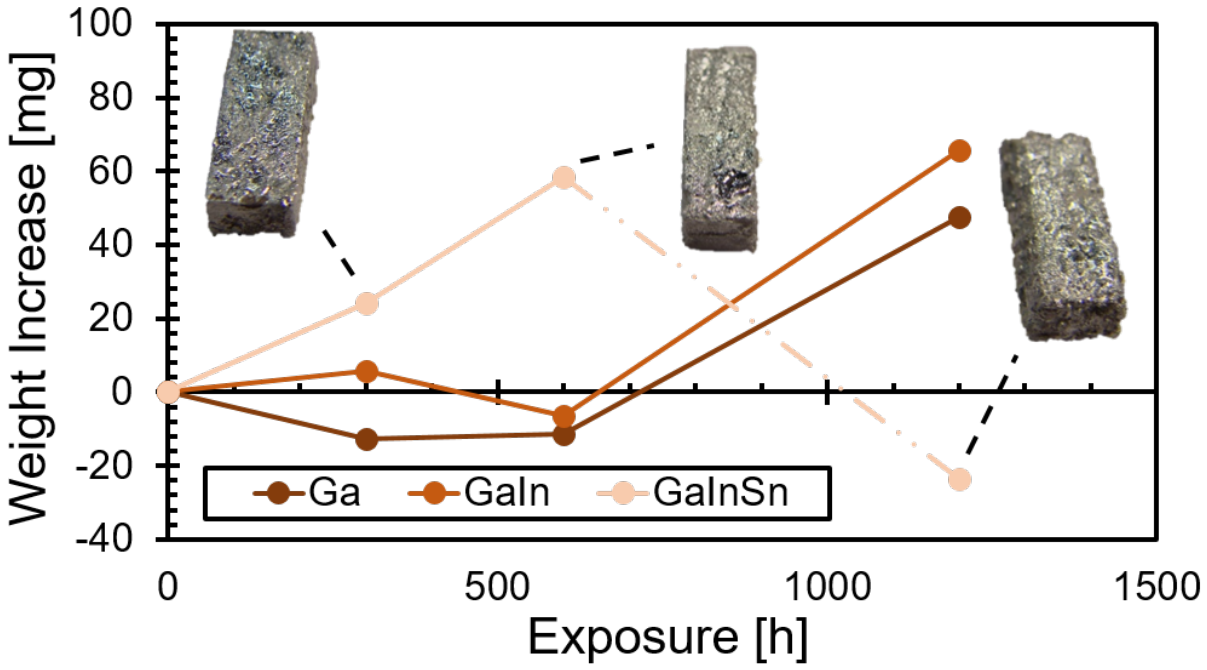

Figure 3.22: Cu couples' weight change. The loss of mass indicates that the Cu was undergoing dissolution of Cu into the liquid metal. With exposure, the Cu saturates the liquid metal and starts alloying. It seems that the additions of In or Sn into the Ga decrease the solubility of Cu into the liquid metal as E-GaInSn exposure immediately results in the Cu specimen alloying.

3.3.5 A Discussion of Possible Mechanisms for the Lack of Corrosion in Nickel-Titanium Alloys

As observed, Ni showed significant corrosion (alloying) with the liquid metals while Ti did not. Thus, one could expect the equiatomic $Ni_{50}Ti_{50}$, nickel-rich $Ni_{55}Ti_{45}$, or $Ni_{49}Ti_{36}Hf_{15}$ to exhibit some amount of corrosion, whether it be dissolution or alloying. However, despite multiple characterization methods, the data suggests that gallium-based liquid metal-induced corrosion in the presence of liquid metal does not occur with any of the tested SMAs at 220°C. Therefore, it is of interest to elucidate what mechanism is preventing these NiTi-based alloys from corrosion. In and Sn additions acted very similar to pure Ga, aside from faster saturation in the Cu couples, while Hf is chemically similar to Ti, i.e., same group on the periodic table, both hcp crystal structures, both form resilient native oxide layers. Thus, assuming In and Sn can be replaced by Ga and Hf

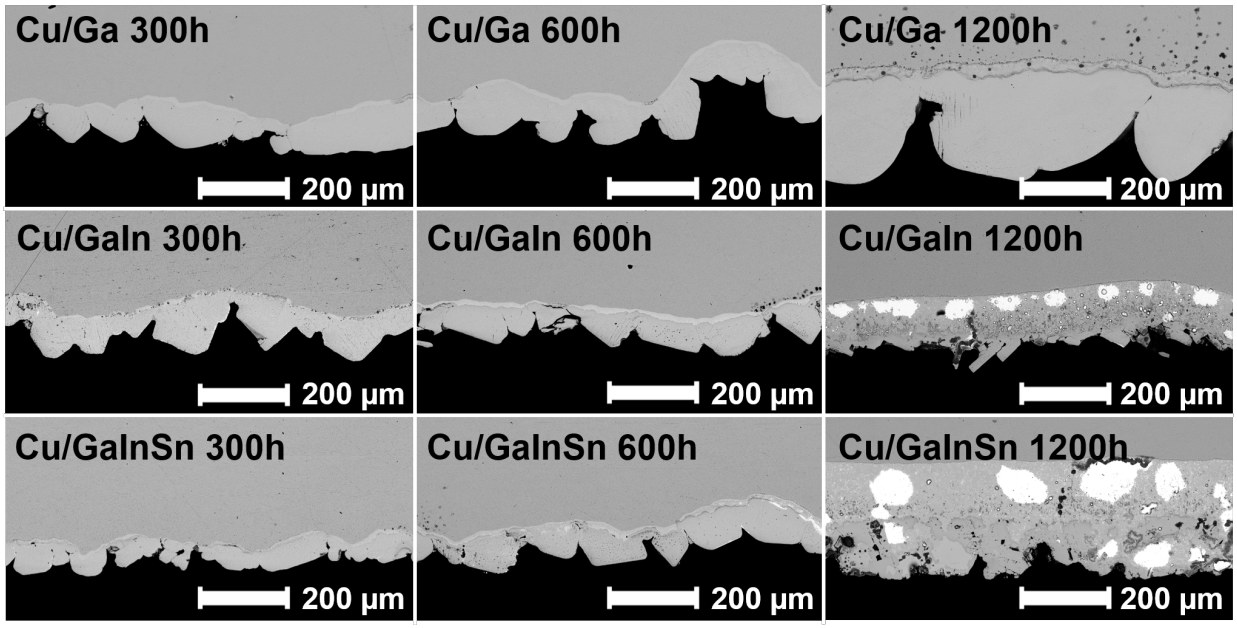

Figure 3.23: BSE imaging of Cu couple cross-sections. The upper section of each image is the bulk Cu. As all samples underwent alloying, the reaction layer grows thicker with longer exposure times.

by Ti, we can identify three possible mechanisms that prevent NiTi from corrosion:

1. a protective oxide layer that forms on Ti-containing surfaces

2. solubility of Ga into Ni vs. Ti

3. thermal activation of some diffusion process

For the first mechanism, it could be argued that the Ti in the nickel-titanium alloys (or alternatively Hf for $Ni_{49}Ti_{36}Hf_{15}$) is forming an oxide layer that is acting as a diffusion barrier and preventing the relatively reactive Ni, or even Ti itself, from interacting with Ga. It is well known that Ti forms resilient and passivating oxide layers upon exposure to even low oxygen environments and $Ni_{50}Ti_{50}$ surfaces are mostly comprised of oxides of Ti due to its higher affinity for oxygen. In the experimental section of this work, it was noted that actions were taken to remove this oxide before immersion into liquid metal. However, the minutes before immersion could result

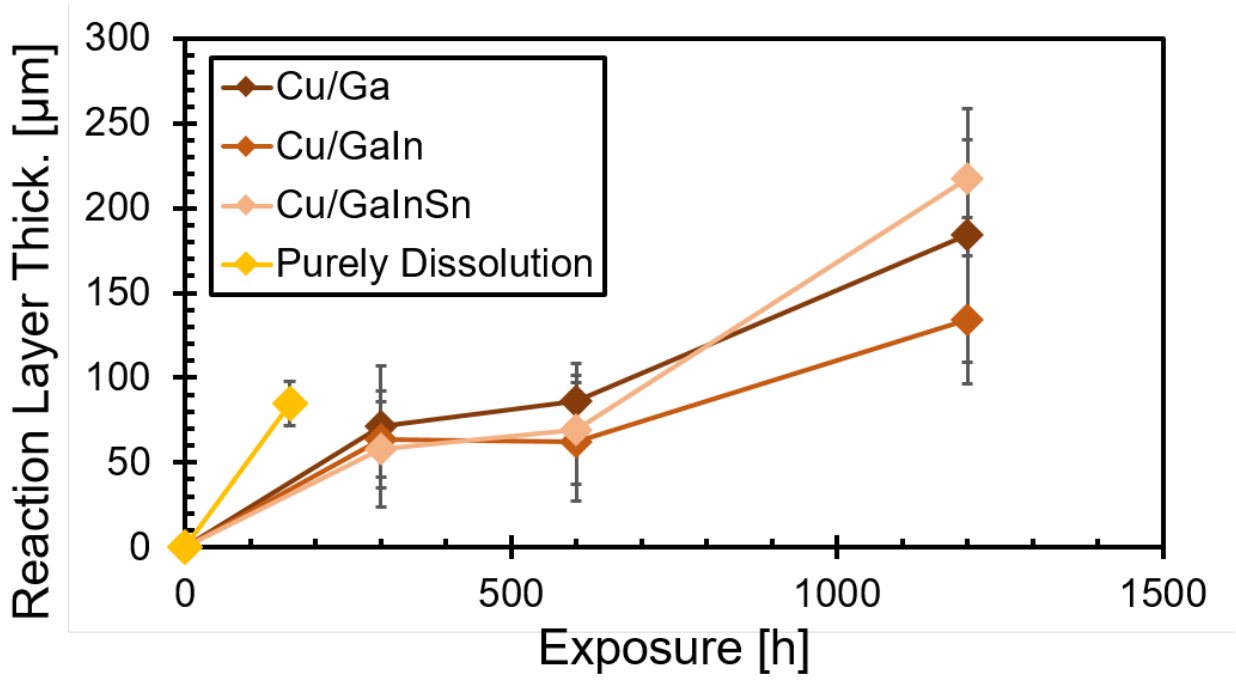

Figure 3.24: Cu couple reaction layer growth. The yellow line was a special case were ample amount of liquid metal was supplied during exposure to promote Cu dissolution. Though it was dissolving, reaction layers still form on the surface. The other Cu samples saturated the liquid metal with Cu and were alloying, as supported by 3.22.

in an oxide layer of at least several angstroms [], though unlikely to result in a significant diffusion barrier. Thus, to further test this mechanism, an additional experiment was performed with a chemical etching step [78] for the removal of any TiO_2. Prepared Ti and $Ni_{55}Ti_{45}$ specimens were etched in boiling sulphuric acid for 2 min to remove the native oxide and then placed, while "wet" with acid, into a bath of E-GaIn and exposed for 160 h at 220 °C with 5x the amount of liquid metal as previous experiments. Nonetheless, this resulted in the same behaviors as the non-etched samples. A reaction layer was not observed with SEM, Ga was not detected by EDS, the weight remained the same, but the edge roughness was higher, though likely from the acid etch. If the oxide was playing a protective role, some intermetallics or mass loss would be expected from this experiment.

To consider the second mechanism, one must refer to the established phase diagrams at the tested temperature of 220°C. For the Ga-Ni system [79], the solubility limit of Ga into the Ni matrix

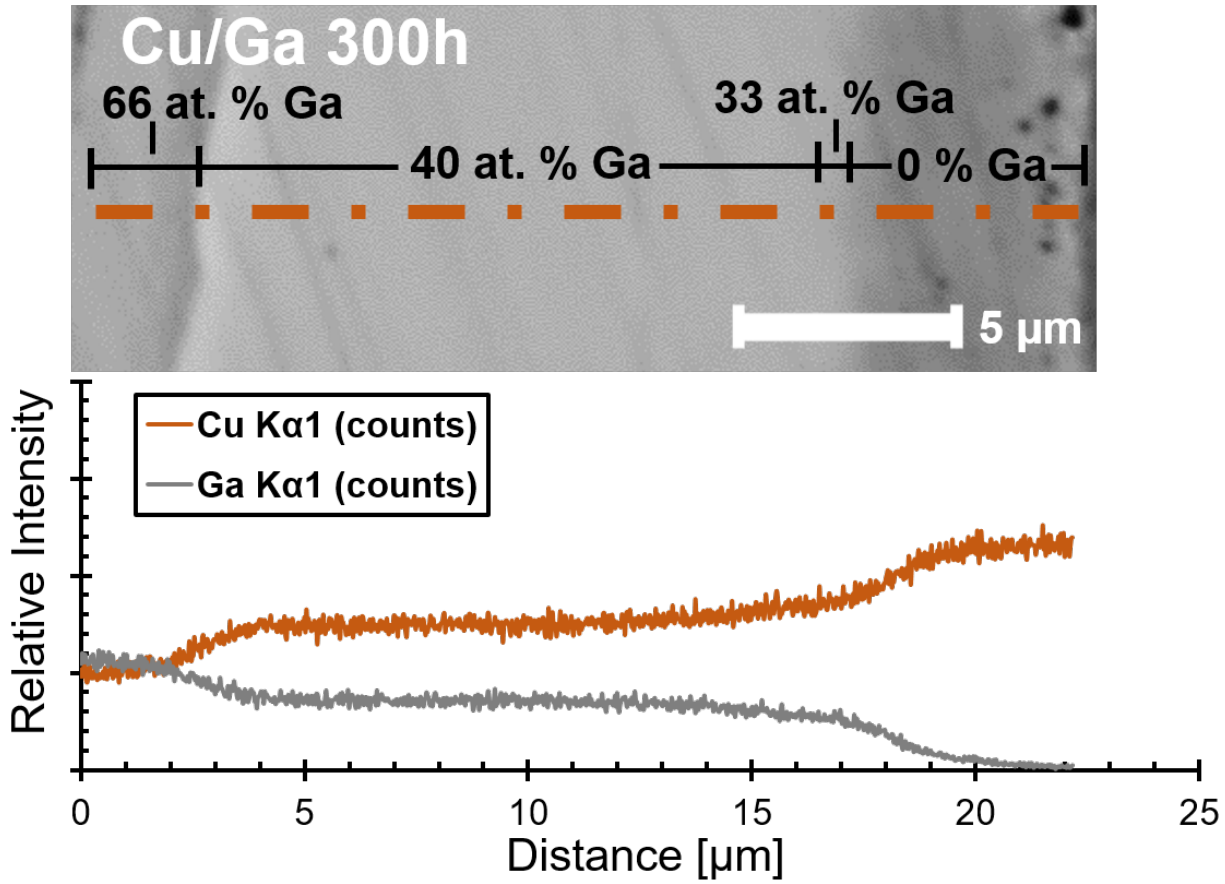

Figure 3.25: EDS linescan of Cu/Ga couple's multi-layer reaction. Multiple intermetallic layers were discovered which correlate with the Cu-Ga phase diagram.

is about 12 at.% Ga while 1.5 at.% Ni into liquid Ga. For the Ga-Ti system [80], temperatures below 900°C have not been established but by extrapolating the available experimental results, one can estimate that there is effectively zero solubility of Ti in liquid Ga and $<$1 at.% Ga into the Ti matrix. Since both Ni-related solubilities are much greater than the solubility of Ga into Ti or Ti into liquid Ga, then the Ni couples should show much more interaction than Ti couples, as was experimental shown. However, this does not explain why corrosion is not observed in the nickel-titanium couples. Perhaps a B2 NiTi matrix has a very low solubility of Ga at 220 °C, though there is no literature to confirm this. On the contrary, there is still 1.5 at.% Ni solubility into liquid Ga which should manifest itself as pitting, increased surface roughness, or mass loss on the tested

nickel-titanium couples; none of these were observed. Thus, it can be determined that solubility alone is not the mechanism preventing corrosion of nickel-titanium couples.

The third identified mechanism preventing interaction of nickel-titanium and its alloys with Ga-based liquid metals could be some temperature-activated process with regards to diffusion. One observation supporting this option recalls the 1.5 at.% Ni solubility in liquid Ga at 220°C, which should result in some overall mass loss for an exposed nickel-titanium specimen. The ability for significant amounts of Ga from the liquid metal to diffuse into the solid Ni would be influenced by the diffusivity of Ga atoms in a Ni matrix and the B2 NiTi matrix. However, there is currently no diffusion literature of such a system. On the other hand, Ga atoms have a high activation energy of 295 kJ/mol [81] in high purity Ti, which may explain no interaction took place in the Ti couples. Ti also has a high self-diffusivity activation energy of 303 kJ/mol [81] which may also by limiting corrosion in addition to its extremely low mutual solubilities [82].

Another observation supporting this option considers the how exposure time did not effect the interaction of nickel-titanium. Nickel-titanium and its alloys were held at 220°C for 1200 h and yet there was no Ga detected in the matrix or edge surfaces. However, nickel-titanium was found to have reactions occur at much smaller time scales (3 h) at higher temperatures of 400°C and significant Ga diffusion in the matrix around 600 °C. Ti closely follows this trend as described in the experiments, where corrosion does not occur until a higher temperature is reached, and then occurs readily. This experiment shows that there is more corrosion seen at 400°C in just 3 h for both Ti and $Ni_{55}Ti_{45}$ than at 220°C for 1200 h. This thereby helps the case that there is some thermal activation component to induce corrosion of NiTi by liquid gallium alloys.

These observations ultimately suggest that there is some thermal activation component with regards to diffusion involved for the ability of nickel-titanium and its alloys to undergo a form of liquid metal-induced corrosion. Additionally, it could not be argued that this corrosion could was simply induced by the increased solubilities at higher temperatures, as it was emphasized previously that solubility at 220°C alone, even at long time scales, did not seem to induce any corrosion.

4. CONCLUSIONS AND FUTURE WORK

4.1 Conclusions

The often disconnected research areas associated with shape memory alloys, microvascular cooling, room-temperature liquid metals, and additive manufacturing have been combined to enable the design and preliminary investigation of liquid metal energy circuits as a new multi-physical method for both heating and cooling SMA actuators. In this work, an liquid metal SMA actuator was both inductively heated and convectively cooled using the same liquid metal circuit for the first time; the advantages of such a method was motivated by computational analysis and substantiated by the experimental investigation herein. Liquid metal channels structurally embedded into a monolithic SMA body can increase thermal transfer rates both in heating and cooling. This ultimately leads to an increase in cyclic actuation frequency, further advancing the applicability of SMA actuators as a viable alternative to conventional actuators. Though the motivational computational analysis showed a feasible operation of an actuation frequency increase of 5 times over traditional design and method, experiments showed a cooling rate increase of 1.6 times, or 40.9% decrease in cooling time. This work also illustrates the enabling aspects of additive manufacturing techniques such as L-PBF in producing fully functional but topologically complex NiTi forms.

Further, this work investigated the effects of L-PBF process parameters on as-fabricated and electropolished surface roughness of interior channels in NiTi. This work specifically characterized the ceiling surfaces of horizontal channels and the walls of vertical channels. The primary observations of this section of work can be summarized as follows:

1. Channel orientation is the single most influential factor for as-fabricated channels for resultant surface roughness, where the root-mean-square surface roughness, S_q, for horizontal channel ceilings is consistently almost twice that of the vertical channel walls

2. Higher energy densities result in larger melt pools, which then lead to larger stalactites and/or increased partial powder fusion to nearby powder

3. Lower energy densities result in the increase of electropolishing efficacy on surface roughness

Thus, it can be concluded that when producing interior channels, one should choose the lowest laser energy density parameter set that can still provide sufficient mechanical properties for ease of surface roughness reduction during a subsequent electropolishing step. This is somewhat contrary to literature which recommends to use higher energy densities to produce lower surface roughness of parts produced by L-PBF; however, this is a reasonable discrepancy as most literature observes top surfaces where this work focuses on side and ceiling surfaces with a subsequent post-processing step.

Last, liquid metal-induced corrosion was investigated to assess both the viability of using liquid metals as multifunctional fluids for SMA-based microfluidics and copper as electrical contacts in liquid metal systems. With various characterization methods, this section of work concludes that there is no evidence of gallium-based liquid metal alloy corrosion with any tested nickel-titanium alloy at 220°C. It was also shown that elemental Cu couples showed dissolution corrosion for unsaturated liquid metal but can later result in alloying upon liquid metal saturation. Further investigation revealed that NiTi did not show corrosion until a temperature threshold was reached (between 400°C and 600°C) which is much higher than the working temperatures of SMA systems and thus permitting the combined use of NiTi and Ga-based liquid metals. It was finally determined that the titanium oxide layer found on the surfaces of Ti and NiTi does not contribute to corrosion prevention.

4.2 Challenges

There were several challenges that had to be overcome in regards to producing an integrated liquid metal SMA actuator.

1. First, actuator quality NiTi is very sensitive to chemistry and will be produced using laser powder-bed fusion, which requires significant trial-and-error to produce a sufficient sample without residual cracking, warping, or loss of shape memory properties.

2. Second, there are many factors to consider for mounting peripherals when testing such a device where there is simultaneously high temperatures to actuate the shape memory alloy, high strains from actuation, high electrical resistivity required to prevent a short circuit between the geometrically configured liquid metal induction coil and the NiTi itself, chemical inertness due to the corrosive nature of liquid metal, and the desire for high thermal conductivity to enable high heat transfer rates.

3. Third, sub-millimeter interior channels can be difficult to produce in laser powder-bed fusion as the channel surface roughness can be on the order of diameter of the channel itself due to the non-melted powder adhering to a nearby melt.

4. Last, liquid metal is known to have unique and extremely destructive corrosion mechanisms with dissimilar solid metals. Utilizing liquid metal as a heat transfer fluid could contact NiTi and result in catastrophically mechanical failure or high amount of metallic loss. There was currently no literature on the interactions of NiTi and liquid gallium alloys before this study.

Some challenges that are yet to be overcome include achieving significantly high actuation frequencies like that of the computational modeling of the liquid metal SMA actuator. The Kapton adhesive that held down the liquid metal induction channel failed at flow rates higher than 1 mL/min. The modeling had a original flow rate of 10 mL/min and the syringe pump system can obtain a maximum flow rate of 30 mL/min. By completely embedding the channels within the SMA, the flow rate will no longer be limited by some factor in the SMA channel itself and the actuator can achieve even higher actuation frequencies. Further, the induction heater can heat the SMA at higher power with more appropriate and heat-resistive mounting peripherals. The polymer tubing to flow the liquid metal would melt or deform near the induction heater interconnects, limiting high heating rates.

4.3 Further Study

Future iterations of this study would include a liquid metal SMA actuator that considers liquid metal channels fully embedded within the SMA component. This will permit much higher flow

rates, better facilitate heat transfer between the liquid metal and the SMA, and increase overall actuator robustness. It is expected that these future actuators will therefore demonstrate even higher actuation frequencies, enabling a new class of power-dense engineering actuation design solutions.

REFERENCES

[1] D. C. Lagoudas, ed., *Shape Memory Alloys: Modeling and Engineering Applications*. New York, NY: Springer, 2008.

[2] J. M. Jani, M. Leary, A. Subic, and M. A. Gibson, "A review of shape memory alloy research, applications and opportunities," *Materials & Design*, vol. 56, pp. 1078–1113, 2014.

[3] S. Barbarino, E. S. Flores, R. M. Ajaj, I. Dayyani, and M. I. Friswell, "A review on shape memory alloys with applications to morphing aircraft," *Smart Materials and Structures*, vol. 23, no. 6, p. 063001, 2014.

[4] D. J. Hartl, D. C. Lagoudas, F. T. Calkins, and J. H. Mabe, "Use of a Ni60Ti shape memory alloy for active jet engine chevron application: I. Thermomechanical characterization," *Smart Materials and Structures*, vol. 19, p. 015020, Jan. 2010.

[5] D. J. Hartl, J. T. Mooney, D. C. Lagoudas, F. T. Calkins, and J. H. Mabe, "Use of a Ni60Ti shape memory alloy for active jet engine chevron application: II. Experimentally validated numerical analysis," *Smart Materials and Structures*, vol. 19, p. 015021, Jan. 2010.

[6] J. Ma, I. Karaman, and R. D. Noebe, "High temperature shape memory alloys," *International Materials Reviews*, vol. 55, no. 5, pp. 257–315, 2010.

[7] J. Huber, N. Fleck, and M. Ashby, "The selection of mechanical actuators based on performance indices," in *Proceedings of the Royal Society of London A: Mathematical, Physical and Engineering Sciences*, vol. 453, pp. 2185–2205, 1997.

[8] B. Lubarsky and S. J. Kaufman, *Review of experimental investigations of liquid-metal heat transfer*. National Advisory Committee for Aeronautics, 1956.

[9] J. Van den Bosch, P. Hosemann, A. Almazouzi, and S. Maloy, "Liquid metal embrittlement of silicon enriched steel for nuclear applications," *Journal of Nuclear Materials*, vol. 398, no. 1, pp. 116–121, 2010.

[10] T. Anderson and I. Ansara, "The Ga-In (gallium-indium) system," *Journal of Phase Equilibria*, vol. 12, no. 1, pp. 64–72, 1991.

[11] T. Beerling, "Planar inductor using liquid metal MEMS technology," Jan. 2009.

[12] D. J. Hartl, G. H. Huff, H. Pan, L. Smith, R. L. Bradford, G. J. Frank, and J. W. Baur, "Analysis and characterization of structurally embedded vascular antennas using liquid metals," in *Sensors and Smart Structures Technologies for Civil, Mechanical, and Aerospace Systems 2016* (J. P. Lynch, ed.), p. 980333, 2016.

[13] R. N. Saunders, J. G. Boyd, D. J. Hartl, J. K. Brown, F. T. Calkins, and D. C. Lagoudas, "A validated model for induction heating of shape memory alloy actuators," *Smart Materials and Structures*, vol. 25, no. 4, p. 045022, 2016.

[14] R. Saunders, J. Boyd, D. Hartl, F. Calkins, and D. Lagoudas, "A Simplified Model for High Rate Actuation of Shape Memory Alloy Torque Tubes Using Induction Heating," *Journal of Intelligent Materials Systems and Structures*, 2017.

[15] A. R. Shahin, P. H. Meckl, J. D. Jones, and M. A. Thrasher, "Enhanced cooling of shape memory alloy wires using semiconductor" heat pump" modules," *Journal of Intelligent Material Systems and Structures*, vol. 5, no. 1, pp. 95–104, 1994.

[16] R. A. Russell and R. B. Gorbet, "Improving the response of SMA actuators," in *Robotics and Automation, 1995. Proceedings., 1995 IEEE International Conference on*, vol. 3, pp. 2299–2304, IEEE, 1995.

[17] A. M. Coppola, L. Hu, P. R. Thakre, M. Radovic, I. Karaman, N. R. Sottos, and S. R. White, "Active Cooling of a Microvascular Shape Memory Alloy-Polymer Matrix Composite Hybrid Material: Active Cooling of a Microvascular Shape Memory," *Advanced Engineering Materials*, vol. 18, pp. 1145–1153, July 2016.

[18] J. H. Mabe, R. T. Ruggeri, E. Rosenzweig, and C.-J. M. Yu, "Nitinol performance characterization and rotary actuator design," in *Smart Structures and Materials 2004: Industrial and*

Commercial Applications of Smart Structures Technologies, vol. 5388, pp. 95–110, International Society for Optics and Photonics, 2004.

[19] R. N. Saunders, D. J. Hartl, J. G. Boyd, and D. C. Lagoudas, "Modeling and development of a twisting wing using inductively heated shape memory alloy actuators," in *SPIE Smart Structures and Materials+ Nondestructive Evaluation and Health Monitoring*, pp. 94310U–94310U, International Society for Optics and Photonics, 2015.

[20] A. J. Neurohr and D. C. Dunand, "Shape-memory NiTi with two-dimensional networks of micro-channels," *Acta Biomaterialia*, vol. 7, no. 4, pp. 1862–1872, 2011.

[21] V. Y. Prokhorenko, V. V. Roshchupkin, M. A. Pokrasin, S. Prokhorenko, and V. Kotov, "Liquid gallium: potential uses as a heat-transfer agent," *High Temperature*, vol. 38, no. 6, pp. 954–968, 2000.

[22] J. Mingear, N. R. Page, A. Greer, B. Bielefeldt, and D. J. Hartl, "Liquid Metal Integration for Expedited Heating and Cooling of Monolithic and Composite SMA Actuators," in *25th AIAA/AHS Adaptive Structures Conference*, p. 1443, 2017.

[23] D. Hartl, J. Mingear, B. Bielefeldt, J. Rohmer, J. Zamarripa, and A. Elwany, "Towards high-frequency shape memory alloy actuators incorporating liquid metal energy circuits," *Shape Memory and Superelasticity*, vol. 3, no. 4, pp. 457–466, 2017.

[24] I. Shishkovsky, I. Yadroitsev, and I. Smurov, "Direct selective laser melting of nitinol powder," *Physics Procedia*, vol. 39, pp. 447–454, 2012.

[25] H. Meier, C. Haberland, and J. Frenzel, "Structural and functional properties of NiTi shape memory alloys produced by selective laser melting," *Innovative Developments in Design and Manufacturing*, pp. 291–296, 2011.

[26] R. F. Hamilton, B. A. Bimber, M. T. Andani, and M. Elahinia, "Multi-scale Shape Memory Effect Recovery in NiTi Alloys Additive Manufactured by Selective Laser Melting and Laser Directed Energy Deposition," *Journal of Materials Processing Technology*, 2017.

[27] B. Zhang, J. Chen, and C. Coddet, "Microstructure and transformation behavior of in-situ shape memory alloys by selective laser melting TiNi mixed powder," *Journal of Materials Science & Technology*, vol. 29, no. 9, pp. 863–867, 2013.

[28] B. Franco, J. Ma, B. Loveall, G. Tapia, K. Karayagiz, J. Liu, A. Elwany, R. Arroyave, and I. Karaman, "A Sensory Material Approach for Reducing Variability in Additively Manufactured Metal Parts," *Scientific Reports*, vol. 7, 2017.

[29] J. J. Lewandowski and M. Seifi, "Metal additive manufacturing: a review of mechanical properties," *Annual Review of Materials Research*, vol. 46, pp. 151–186, 2016.

[30] M. H. Elahinia, M. Hashemi, M. Tabesh, and S. B. Bhaduri, "Manufacturing and processing of NiTi implants: a review," *Progress in Materials Science*, vol. 57, no. 5, pp. 911–946, 2012.

[31] M. H. Wu, "Fabrication of nitinol materials and components," in *Materials Science Forum*, vol. 394, pp. 285–292, Trans Tech Publ, 2002.

[32] S. Xenos-Despina and N. Gregory, "The Unique Properties, Manufacturing Processes and Applications of Near Equatomic Ni-Ti Alloys," 2016.

[33] J. Ma, B. Franco, G. Tapia, K. Karayagiz, L. Johnson, J. Liu, R. Arroyave, I. Karaman, and A. Elwany, "Spatial Control of Functional Response in 4D-Printed Active Metallic Structures," *Scientific Reports*, vol. 7, 2017.

[34] C. Haberland, M. Elahinia, J. M. Walker, H. Meier, and J. Frenzel, "On the development of high quality NiTi shape memory and pseudoelastic parts by additive manufacturing," *Smart Materials and Structures*, vol. 23, no. 10, p. 104002, 2014.

[35] N. Sharma, K. Kumar, T. Raj, and V. Kumar, "Porosity exploration of SMA by Taguchi, regression analysis and genetic programming," *Journal of Intelligent Manufacturing*, pp. 1–8, 2016.

[36] M. Speirs, X. Wang, S. Van Baelen, A. Ahadi, S. Dadbakhsh, J.-P. Kruth, and J. Van Humbeeck, "On the Transformation Behavior of NiTi Shape-Memory Alloy Produced by SLM," *Shape Memory and Superelasticity*, vol. 2, no. 4, pp. 310–316, 2016.

[37] M. de Wild, F. Meier, T. Bormann, C. B. Howald, and B. Müller, "Damping of selective-laser-melted NiTi for medical implants," *Journal of Materials Engineering and Performance*, vol. 23, no. 7, pp. 2614–2619, 2014.

[38] B. B. Godbey, *Surface Finish Control of Three-Dimensional Printed Metal Tooling*. PhD thesis, Clemson University, 2007.

[39] K. Mumtaz and N. Hopkinson, "Top surface and side roughness of Inconel 625 parts processed using selective laser melting," *Rapid Prototyping Journal*, vol. 15, no. 2, pp. 96–103, 2009.

[40] F. Calignano, D. Manfredi, E. Ambrosio, L. Iuliano, and P. Fino, "Influence of process parameters on surface roughness of aluminum parts produced by dmls," *The International Journal of Advanced Manufacturing Technology*, vol. 67, no. 9-12, pp. 2743–2751, 2013.

[41] J. Delgado, J. Ciurana, and C. A. Rodríguez, "Influence of process parameters on part quality and mechanical properties for dmls and slm with iron-based materials," *The International Journal of Advanced Manufacturing Technology*, vol. 60, no. 5-8, pp. 601–610, 2012.

[42] G. Strano, L. Hao, R. M. Everson, and K. E. Evans, "Surface roughness analysis, modelling and prediction in selective laser melting," *Journal of Materials Processing Technology*, vol. 213, no. 4, pp. 589–597, 2013.

[43] B. Vandenbroucke and J.-P. Kruth, "Selective laser melting of biocompatible metals for rapid manufacturing of medical parts," *Rapid Prototyping Journal*, vol. 13, no. 4, pp. 196–203, 2007.

[44] A. Hussein, L. Hao, C. Yan, R. Everson, and P. Young, "Advanced lattice support structures for metal additive manufacturing," *Journal of Materials Processing Technology*, vol. 213, no. 7, pp. 1019–1026, 2013.

[45] D. S. Rickerby and A. Matthews, *Advanced Surface Coatings: A Handbook of Surface Engineering*. Blackie. Chapman and Hall, 1991.

[46] S. G. Kandlikar, D. Schmitt, A. L. Carrano, and J. B. Taylor, "Characterization of surface roughness effects on pressure drop in single-phase flow in minichannels," *Physics of Fluids*, vol. 17, no. 10, p. 100606, 2005.

[47] X. Yuan, Z. Tao, H. Li, and Y. Tian, "Experimental investigation of surface roughness effects on flow behavior and heat transfer characteristics for circular microchannels," *Chinese Journal of Aeronautics*, vol. 29, no. 6, pp. 1575–1581, 2016.

[48] Y. Plevachuk, V. Sklyarchuk, S. Eckert, G. Gerbeth, and R. Novakovic, "Thermophysical properties of the liquid Ga–In–Sn eutectic alloy," *Journal of Chemical & Engineering Data*, vol. 59, no. 3, pp. 757–763, 2014.

[49] T. Liu, P. Sen, and C.-J. Kim, "Characterization of nontoxic liquid-metal alloy galinstan for applications in microdevices," *Journal of Microelectromechanical Systems*, vol. 21, no. 2, pp. 443–450, 2012.

[50] D. J. Hartl, G. J. Frank, and J. W. Baur, "Embedded magnetohydrodynamic liquid metal thermal transport: validated analysis and design optimization," *Journal of Intelligent Material Systems and Structures*, vol. 28, no. 7, pp. 862–877, 2017.

[51] K. Ma and J. Liu, "Liquid metal cooling in thermal management of computer chips," *Frontiers of Energy and Power Engineering in China*, vol. 1, no. 4, pp. 384–402, 2007.

[52] I. Gmati, H. Boussetta, M. A. KAllala, and K. Besbes, "Wide-range RF MEMS variable inductor using micro pump actuator," in *2nd International Conference on Signals, Circuits and Systems, 2008. SCS 2008.*, pp. 1–4, IEEE, 2008.

[53] M. D. Dickey, R. C. Chiechi, R. J. Larsen, E. A. Weiss, D. A. Weitz, and G. M. Whitesides, "Eutectic gallium-indium (EGaIn): a liquid metal alloy for the formation of stable structures in microchannels at room temperature," *Advanced Functional Materials*, vol. 18, no. 7, pp. 1097–1104, 2008.

[54] B. L. Cumby, D. B. Mast, C. E. Tabor, M. D. Dickey, and J. Heikenfeld, "Robust pressure-actuated liquid metal devices showing reconfigurable electromagnetic effects at GHz frequen-

cies," *IEEE Transactions on Microwave Theory and Techniques*, vol. 63, no. 10, pp. 3122–3130, 2015.

[55] A. Tabatabai, A. Fassler, C. Usiak, and C. Majidi, "Liquid-phase gallium–indium alloy electronics with microcontact printing," *Langmuir*, vol. 29, no. 20, pp. 6194–6200, 2013.

[56] M. Hodes, R. Zhang, R. Wilcoxon, and N. Lower, "Cooling potential of galinstan-based minichannel heat sinks," in *3th IEEE Intersociety Conference on Thermal and Thermomechanical Phenomena in Electronic Systems (ITherm)*, pp. 297–302, IEEE, 2012.

[57] W. Rostoker, J. M. McCaughy, and H. Markus, *Embrittlement by Liquid Metals*. New York, NY: Reinhold Publishing Corporation, Jan. 1960.

[58] M. H. Kamdar, "Embrittlement by liquid metals," *Progress in Materials Science*, vol. 15, no. 4, pp. 289–374, 1973.

[59] M. Nicholas and C. Old, "Liquid metal embrittlement," *Journal of Materials Science*, vol. 14, no. 1, pp. 1–18, 1979.

[60] F. Barbier and J. Blanc, "Corrosion of martensitic and austenitic steels in liquid gallium," *Journal of materials research*, vol. 14, no. 03, pp. 737–744, 1999.

[61] B. Kockar, I. Karaman, J. Kim, and Y. Chumlyakov, "A method to enhance cyclic reversibility of NiTiHf high temperature shape memory alloys," *Scripta Materialia*, vol. 54, no. 12, pp. 2203–2208, 2006.

[62] P. F. Tortorelli and S. J. Pawel, "Corrosion by Liquid Metals," in *Corrosion: Fundamentals, Testing, and Protection*, vol. 13A of *ASM Handbook*, pp. 129–134, ASM International, 2003.

[63] J. Mingear and D. Hartl, "Corrosion of nickel-titanium, C110, and Al6061 in gallium-based liquid metal alloys," in *TMS 2017 146th Annual Meeting & Exhibition Supplemental Proceedings*, pp. 587–596, Springer, 2017.

[64] L. Migaj, T. Taritsina, and N. Taishcheva, M.I., "Corrosion resistance of construction materials in eutectic alloy gallium-indium-tin," *Study of Rare Earths Alloys*, vol. 84, pp. 26–29, 1978.

[65] S. D. Oehler, D. J. Hartl, and D. C. Lagoudas, "Analysis and optimization of improved hybrid sma flexures for high rate actuation," in *Industrial and Commercial Applications of Smart Structures Technologies 2011*, vol. 7979, p. 797907, International Society for Optics and Photonics, 2011.

[66] T. L. Bergman and F. P. Incropera, *Fundamentals of Heat and Mass Transfer*. John Wiley & Sons, 2011.

[67] A. Spierings, N. Herres, and G. Levy, "Influence of the particle size distribution on surface quality and mechanical properties in AM steel parts," *Rapid Prototyping Journal*, vol. 17, no. 3, pp. 195–202, 2011.

[68] J. Antony, *Design of experiments for engineers and scientists*. Elsevier, 2014.

[69] T. R. Thomas, *Rough Surfaces*. World Scientific, 1998.

[70] R. Leach, *Fundamental Principles of Engineering Nanometrology*. Elsevier, 2014.

[71] M. Pohl, C. Hessing, and J. Frenzel, "Electrolytic processing of NiTi shape memory alloys," *Materials Science and Engineering: A*, vol. 378, no. 1, pp. 191–199, 2004.

[72] K. Gupta, "The Hf-Ni-Ti (hafnium-nickel-titanium) system," *Journal of Phase Equilibria*, vol. 22, no. 1, pp. 69–72, 2001.

[73] J. R. Bickford, "Automatic stripe analysis tool," tech. rep., ARMY RESEARCH LAB ADELPHI MD SENSORS AND ELECTRON DEVICES DIRECTORATE, 2013.

[74] J. Mabe, F. Calkins, and G. Butler, "Boeing's variable geometry chevron, morphing aerostructure for jet noise reduction," in *47th AIAA/ASME/ASCE/AHS/ASC Structures, Structural Dynamics, and Materials Conference 14th AIAA/ASME/AHS Adaptive Structures Conference 7th*, p. 2142, 2006.

[75] J. P. Davim and others, *Surface Integrity in Machining*, vol. 1848828742. Springer, 2010.

[76] F. Van Loo, "Multiphase diffusion in binary and ternary solid-state systems," *Progress in Solid State Chemistry*, vol. 20, no. 1, pp. 47–99, 1990.

[77] P. Subramanian and D. Laughlin, "Cu (copper) binary alloy phase diagrams," in *Alloy Phase Diagrams*, vol. 3 of *ASM Handbook*, pp. 304–326, ASM International, 2016.

[78] P. Walker and W. H. Tarn, *CRC Handbook of Metal Etchants*. CRC press, 1990.

[79] H. Okamoto, "Ga-Ni (gallium-nickel)," *Journal of Phase Equilibria and Diffusion*, vol. 31, no. 6, pp. 575–576, 2010.

[80] J.-B. Li, J.-C. Tedenac, and M.-C. Record, "Thermodynamic analysis of the Ga-Ti system," *Journal of Alloys and Compounds*, vol. 358, no. 1-2, pp. 133–141, 2003.

[81] R. A. Perez, H. Nakajima, and F. Dyment, "Diffusion in α-Ti and Zr," *Materials Transactions*, vol. 44, no. 1, pp. 2–13, 2003.

[82] R. P. Elliott, "Diffusion in titanium and titanium alloys," tech. rep., ARMOUR RESEARCH FOUNDATION CHICAGO IL, 1962.

[83] J. Murray, "Phase diagram of binary titanium alloys," in *Alloy Phase Diagrams*, vol. 3 of *ASM Handbook*, pp. 197–211, ASM International, 1987.

APPENDIX A

APPENDIX OF RELEVANT BINARY PHASE DIAGRAMS

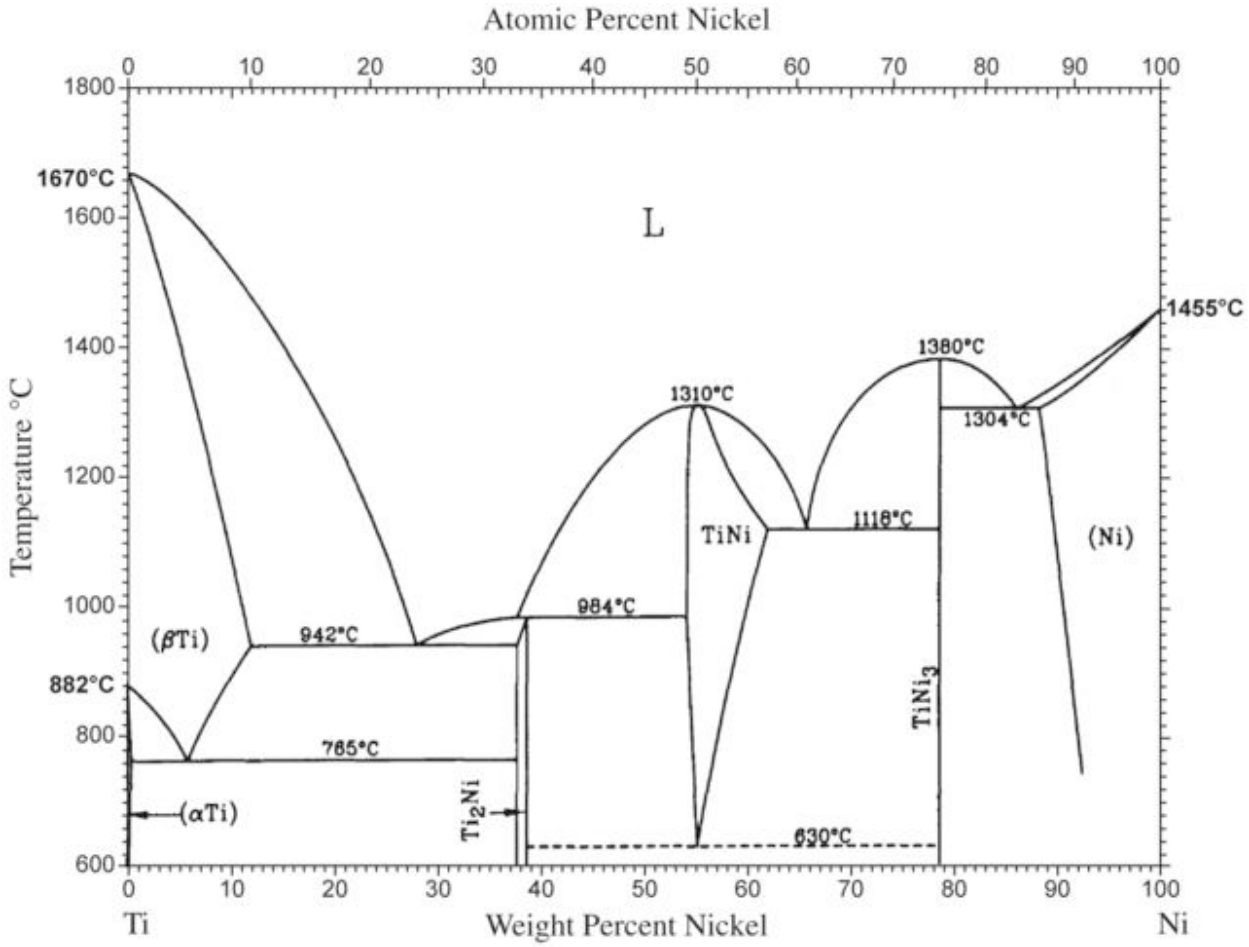

Figure A.1: The Nickel-Titanium System. Reprinted with permission from [83].

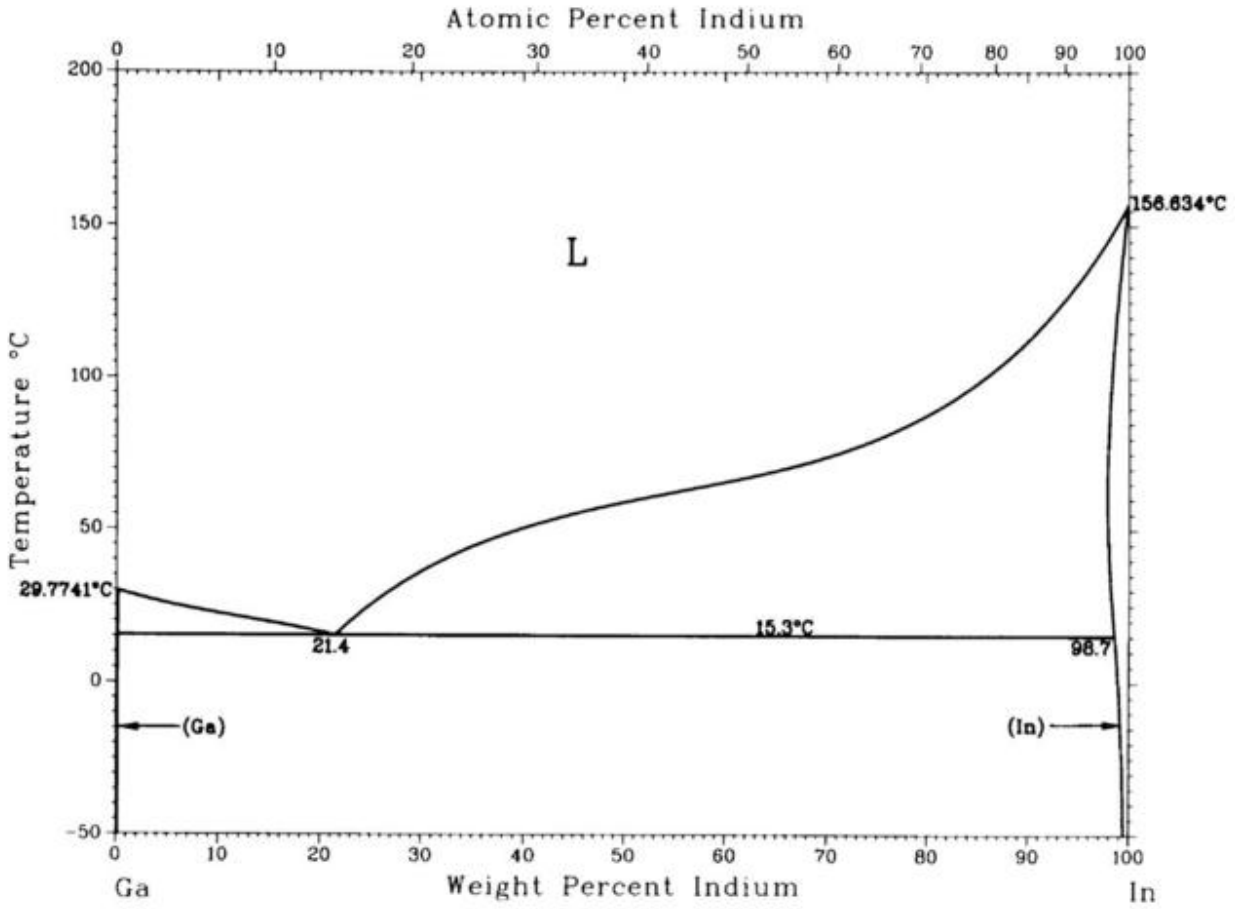

Figure A.2: The Gallium-Indium System. Reprinted with permission from [10].

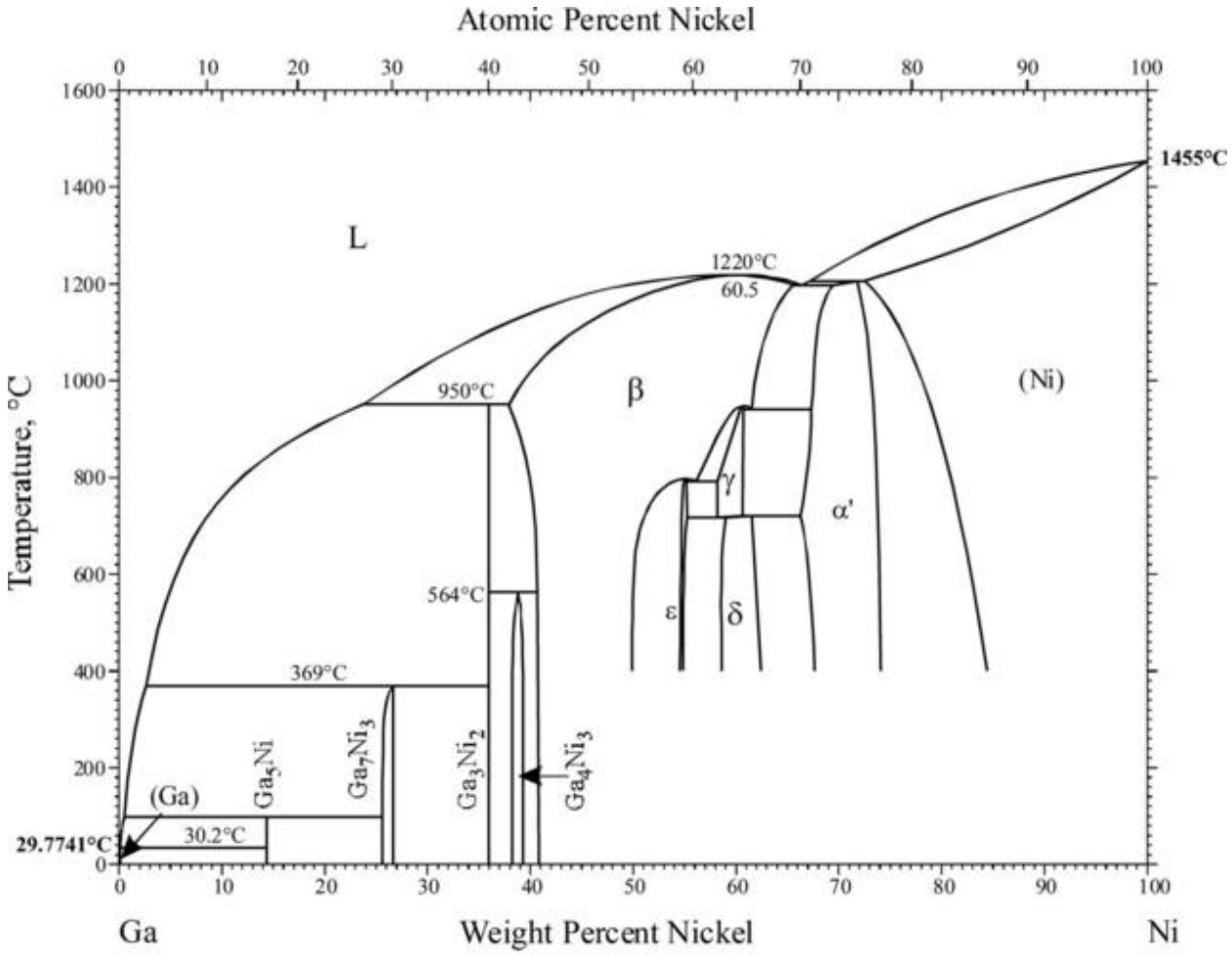

Figure A.3: The Nickel-Gallium System. Reprinted with permission from [79].

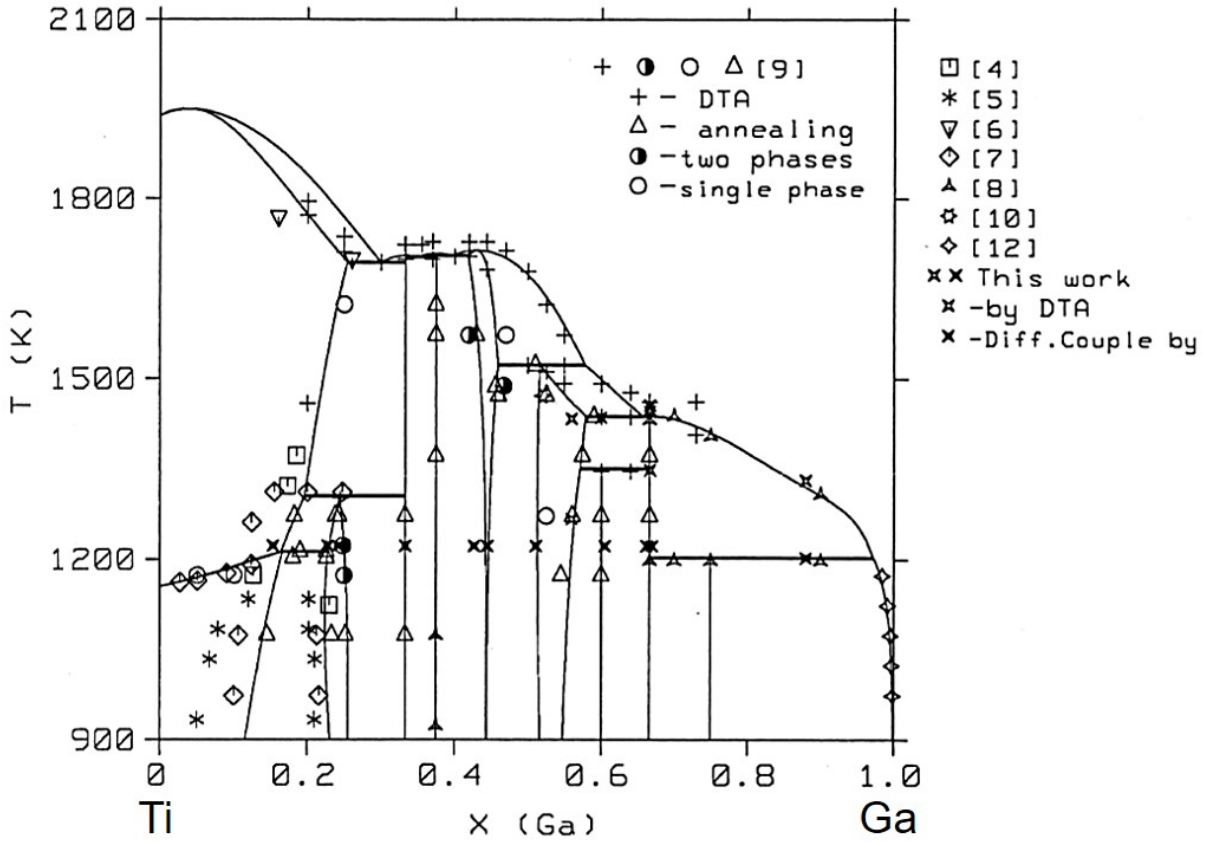

Figure A.4: The Titanium-Gallium System. Reprinted with permission from [80].

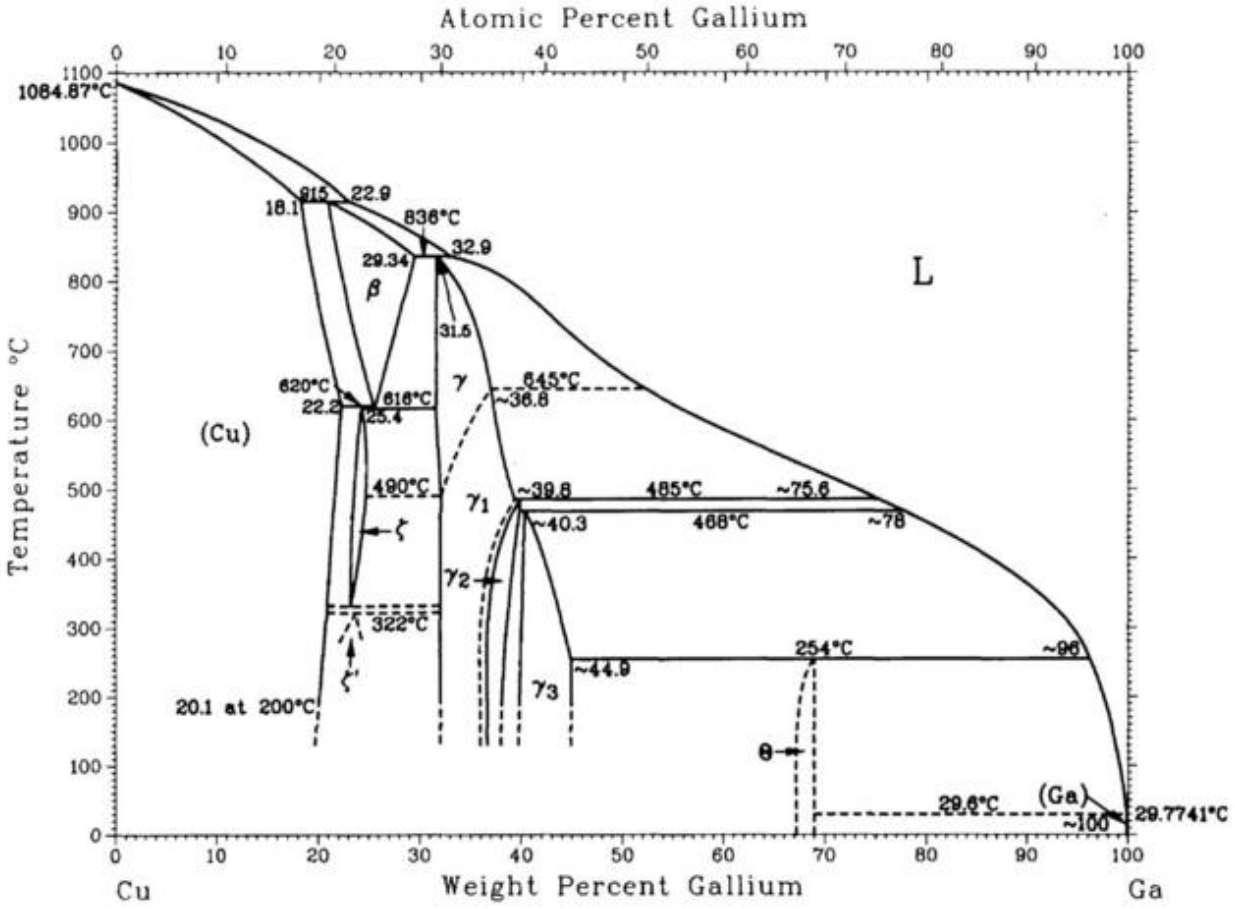

Figure A.5: The Copper-Gallium System. Reprinted with permission from [77].